

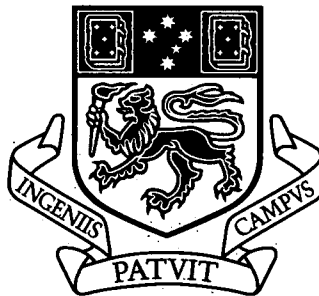
LINEAR AND NONLINEAR PROGRESSIVE ROSSBY WAVES ON A ROTATING SPHERE

by

Timothy G. Callaghan, B.A. B.Sc. Hons (Qld)

Submitted in fulfilment of the requirements
for the Degree of Doctor of Philosophy

Department of Mathematics
University of Tasmania
January, 2005




I declare that this thesis contains no material which has been accepted for a degree or diploma by the University or any other institution, except by way of background information and duly acknowledged in the thesis, and that, to the best of my knowledge and belief, this thesis contains no material previously published or written by another person, except where due acknowledgement is made in the text of the thesis.

Signed: 
Timothy G. Callaghan

Date: 13/01/2005

This thesis may be made available for loan and limited copying in accordance with the *Copyright Act 1968*

Signed: 
Timothy G. Callaghan

Date: 13/01/2005

ABSTRACT

We present an analysis of incompressible and compressible flow of a thin layer of fluid with a free-surface on a rotating sphere. Our general aim is to investigate the nature of progressive Rossby wave structures that are possible in this rotating system, with the goal of expanding previous research by conducting an in-depth analysis of wavespeed/amplitude relationships.

A linearized theory for the incompressible dynamics, closely related to the theory developed by B. Haurwitz, is constructed, with good agreement observed between the two separate models. This result is then extended to the numerical solution of the full model, to obtain highly nonlinear large-amplitude progressive-wave solutions in the form of Fourier series. A detailed picture is developed of how the progressive wavespeed depends on the wave amplitude. This approach reveals the presence of nonlinear resonance behaviour, with different disjoint solution branches existing at different values of the amplitude. Additionally, we show that the formation of localised low pressure systems is an inherent feature of the nonlinear dynamics, once the forcing amplitude reaches a certain critical level.

We then derive a new free-surface model for compressible fluid dynamics and repeat the above analysis by first constructing a linearized solution and then using this to guide the computation of nonlinear solutions via a bootstrapping process. It is shown that if the value of the pressure on the free-surface is assumed to be zero, which is consistent with the concept of the atmosphere terminating, then the model almost reduces to the incompressible dynamics with the only difference being a slightly modified conservation of mass equation. By forcing wave amplitude in the model we show that the resonant behaviour observed in the incompressible dynamics is again encountered in the compressible model. The effect of the compressibility is observed to become apparent through damped resonance behaviour in general, so that in some instances two neighbouring disjoint solution branches from the incompressible dynamics are seen to merge into one continuous solution branch when compressible dynamics are incorporated. In closing, some conjectures are made as

to how these results might help explain certain observed atmospheric phenomena. In particular it is conjectured that the process of atmospheric blocking is a direct result of critically forced stationary Rossby waves.

ACKNOWLEDGEMENTS

I would like to sincerely thank my supervisor Professor Larry Forbes for his faithful guidance and insight throughout all stages of this research. Having someone to look up to and learn from is a great honour and privilege, and to him I will be eternally indebted for his enthusiasm and encouragement.

I would also like to express deep gratitude to Dr Simon Wotherspoon for many stimulating and illuminating discussions along the way. His advice, critical analysis and wit have been most welcome and enjoyed immensely. A big thank you also to all my mathematically minded friends both here at UTas and back at UQ for general support and advice. In addition I wish to acknowledge the financial assistance of the Australian government for an APA scholarship; this assistance has ultimately afforded me the time and financial freedom to pursue this research.

Finally I would like to thank friends and family for continued emotional support. In particular Mr Aaron Ryan has been a wonderful friend full of encouragement who I will continue to value highly for his intelligence and like minded sense of humour. To my parents and sisters I owe thanks not only for unconditional love and support but also for believing in me and convincing me otherwise of my doubts in my own ability at those, perhaps rather too frequent, precipitous times throughout this emotionally taxing but highly rewarding period of my life.

TABLE OF CONTENTS

TABLE OF CONTENTS	i
LIST OF TABLES	v
LIST OF FIGURES	vi
1 INTRODUCTION	1
1.1 Brief Literature Review and Research Objective	1
1.2 Preliminaries	4
2 INCOMPRESSIBLE LINEARIZED SHALLOW ATMOSPHERE MODEL	8
2.1 Derivation	8
2.2 Progressive-Wave Coordinate Transform	13
2.3 Non-dimensionalization of the Governing Equations	14
2.4 Linearization of the Equations	15
2.4.1 Base Zonal Flow Derivation	15
2.4.2 Linearization about the Base Zonal Flow	17
2.5 Numerical Solution of the Linearized Equations	19
2.5.1 Series Representation	19
2.5.2 Galerkin Method	21
2.5.3 Truncation and Generalised Eigenvalue Formulation	25

2.6	Solution and Results	27
2.6.1	Parameters and Constants	27
2.6.2	Results for $\kappa = 3, 4$ and 5	29
2.6.3	Comparison with Rossby-Haurwitz solution	35
3	INCOMPRESSIBLE NONLINEAR SHALLOW ATMOSPHERE MODEL	40
3.1	Problem Specification	40
3.1.1	Conservation Equations	40
3.1.2	Series Representation	41
3.1.3	Volume Specification	43
3.2	Numerical Solution Method	44
3.2.1	Collocation	44
3.2.2	Newton-Raphson Technique	45
3.3	Code Highlights	48
3.3.1	Programming Language and Computational Environment . .	48
3.3.2	Truncation	48
3.3.3	Forcing the Solution	49
3.3.4	Collocation Points	50
3.3.5	Caching the Basis Functions	51
3.3.6	Calculation of the Jacobian Matrix	52
3.3.7	Adaptive Integration Method	54
3.3.8	Bootstrapping	54
3.4	Solution and Results	55
3.4.1	Measuring the Amplitude	55
3.4.2	Parameters and Constants	57
3.4.3	Results for $\kappa = 4, \omega = 1.25$	58

3.4.4	Results for $\kappa = 4$, $\omega = 1.0$	61
3.4.5	Results for $\kappa = 5$, $\omega = 1.25$	68
3.4.6	Results for $\kappa = 5$, $\omega = 1.0$	71
3.5	Closing Remarks	73
4	COMPRESSIBLE LINEARIZED SHALLOW ATMOSPHERE MODEL	74
4.1	Derivation	74
4.2	Non-dimensionalization and Problem Simplification	82
4.2.1	Non-dimensionalization	82
4.2.2	Problem Simplification	83
4.3	Linearization of the Equations	84
4.4	Numerical Solution of the Linearized Equations	86
4.5	Solution and Results	87
4.5.1	Model Parameters	87
4.5.2	Zonal Flow Parameters and Mass Specification	88
4.5.3	Results for $\kappa = 3, 4$ and 5	90
5	COMPRESSIBLE NONLINEAR SHALLOW ATMOSPHERE MODEL	97
5.1	Problem Specification	97
5.1.1	Conservation Equations	97
5.1.2	Mass Specification	98
5.2	Numerical Solution Method	99
5.2.1	Series Solution and Algorithm	99
5.2.2	Amplitude Measurement	102
5.3	Solution and Results	103
5.3.1	Model parameters	103

TABLE OF CONTENTS

iv

5.3.2	Results for $\kappa = 4, \omega = 1.25$	103
5.3.3	Results for $\kappa = 4, \omega = 1.0$	106
5.3.4	Results for $\kappa = 5, \omega = 1.25$	108
5.3.5	Results for $\kappa = 5, \omega = 1.0$	109
5.4	Closing Remarks	111
6	CONCLUSION AND CLOSING REMARKS	112
6.1	Discussion and Application to Meteorology	112
6.2	Future work and Closing Remarks	114
A	EVALUATION OF VOLUME SPECIFICATION JACOBIAN ELEMENTS	116
B	COMPRESSIBLE LINEARIZED SYSTEM DERIVATION	118
C	3D OPENGL ROSSBY WAVE VIEWER	121
	BIBLIOGRAPHY AND SELECTED READING LIST	125
	INDEX	130

LIST OF TABLES

2.1	Convergence of incompressible wavespeed and first three coefficients in each series for increasing N , $\kappa = 3$	30
2.2	Convergence of incompressible wavespeed and first three coefficients in each series for increasing N , $\kappa = 4$	30
2.3	Convergence of incompressible wavespeed and first three coefficients in each series for increasing N , $\kappa = 5$	31
3.1	Damped Newton-Raphson algorithm.	47
4.1	Convergence of compressible wavespeed and first three coefficients in each series for increasing N , $\kappa = 3$	90
4.2	Convergence of compressible wavespeed and first three coefficients in each series for increasing N , $\kappa = 4$	91
4.3	Convergence of compressible wavespeed and first three coefficients in each series for increasing N , $\kappa = 5$	91

LIST OF FIGURES

1.1	Spherical coordinate system with free-surface.	5
2.1	Free-surface height parameters	8
2.2	Full eigen-spectrum for $\kappa = 4$ with $N = 5$	33
2.3	Zoomed eigen-spectrum for $\kappa = 4$ with $N = 50$	34
2.4	Comparison of incompressible linearized and Rossby-Haurwitz solutions for $\kappa = 3, 4$ and 5 with $N = 100$	36
2.5	Incompressible shallow atmosphere free-surface contours for $\kappa = 4$ with $N = 100$	37
2.6	Rossby-Haurwitz free-surface contours for $\kappa = 4$	37
2.7	Incompressible shallow atmosphere free-surface contours with corresponding velocity vector field for $\kappa = 4$ with $N = 100$	38
3.1	Various amplitude measurement methods	56
3.2	Incompressible wavespeed versus amplitude for $\kappa = 4$ and $\omega = 1.25$	59
3.3	Incompressible shallow atmosphere free-surface contours for $\kappa = 4$, $\omega = 1.25$ at limit of computation. The average amplitude is $\mathcal{A}_{ave} = 12.5104(deg.)$ and the wavespeed is $c = 0.9580$	60
3.4	Incompressible wavespeed versus amplitude for $\kappa = 4$ and $\omega = 1.0$	62
3.5	Incompressible shallow atmosphere free-surface contours at end of branch 1 for $\kappa = 4$, $\omega = 1.0$. The average amplitude is $\mathcal{A}_{ave} = 13.6732(deg.)$ and the wavespeed is $c = 0.3978$	64

3.6	Incompressible shallow atmosphere free-surface contours at end of branch 4 for $\kappa = 4$, $\omega = 1.0$. The average amplitude is $\mathcal{A}_{ave} = 17.11662(deg.)$ and the wavespeed is $c = 0.3997$	65
3.7	Incompressible shallow atmosphere free-surface contours at end of branch 5 for $\kappa = 4$, $\omega = 1.0$. The average amplitude is $\mathcal{A}_{ave} = 17.11662(deg.)$ and the wavespeed is $c = 0.4016$	66
3.8	Incompressible shallow atmosphere free-surface contours with corresponding velocity vector field at end of branch 5 for $\kappa = 4$, $\omega = 1.0$. The average amplitude is $\mathcal{A}_{ave} = 17.11662(deg.)$ and the wavespeed is $c = 0.4016$	67
3.9	Incompressible wavespeed versus amplitude for $\kappa = 5$ and $\omega = 1.25$.	68
3.10	Incompressible shallow atmosphere free-surface contours at end of branch 1 for $\kappa = 5$, $\omega = 1.25$. The average amplitude is $\mathcal{A}_{ave} = 8.3678(deg.)$ and the wavespeed is $c = 1.5812$	70
3.11	Incompressible wavespeed versus amplitude for $\kappa = 5$ and $\omega = 1.0$.	71
3.12	Incompressible shallow atmosphere free-surface contours at end of branch 1 for $\kappa = 5$, $\omega = 1.0$. The average amplitude is $\mathcal{A}_{ave} = 9.3175(deg.)$ and the wavespeed is $c = 0.9945$	72
4.1	Free-surface height parameters	75
4.2	Comparison of compressible linearized and Rossby-Haurwitz solutions for $\kappa = 3, 4$ and 5 with $N = 100$	92
4.3	Compressible linearized free-surface contours for $\kappa = 4$ with $N = 100$. .	93
4.4	Compressible linearized density contours for $\kappa = 4$ with $N = 100$. . .	94
4.5	Compressible linearized pressure contours for $\kappa = 4$ with $N = 100$. .	95
4.6	Compressible linearized pressure contours with corresponding velocity vector field for $\kappa = 4$ with $N = 100$	95
5.1	Compressible wavespeed versus Amplitude for $\kappa = 4$ and $\omega = 1.25$.	104
5.2	Compressible free-surface contours at end of branch 2 for $\kappa = 4$, $\omega = 1.25$	105

5.3	Compressible free-surface contours with velocity field at end of branch 2 for $\kappa = 4$, $\omega = 1.25$	106
5.4	Compressible wavespeed versus amplitude for $\kappa = 4$ and $\omega = 1.0$. .	107
5.5	Compressible wavespeed versus Amplitude for $\kappa = 5$ and $\omega = 1.25$.	108
5.6	Compressible wavespeed versus Amplitude for $\kappa = 5$ and $\omega = 1.0$. .	110
C.1	Rossby-wave viewer output, Equatorial region	121
C.2	Rossby-wave viewer output, Antarctic polar region	122
C.3	Rossby-wave viewer output, Australian region	123

CHAPTER 1

INTRODUCTION

1.1 Brief Literature Review and Research Objective

Since the classic paper by Rossby [69], proving the existence of large-scale planetary waves in the atmosphere, there has been much interest and time devoted to understanding and describing these planetary waves, known throughout the scientific community as Rossby waves. In particular, how Rossby waves influence the global circulation of the atmosphere has been the focus of a wide body of research over the past sixty years and it has been suggested by Lorenz [58], and later supported by Lilly [50], that the dynamical stability of Rossby waves might impose a limit on the overall numerical predictability of the global circulation.

Traditionally, almost all analytical and numerical analysis of planetary waves has been carried out either on a localized tangent plane to a sphere, the β -plane, or else with a simplified set of governing equations for the full spherical geometry. The benefits of these two approaches are that the recovery of closed form wave solutions to the equations under consideration is often possible, of which the wave forms found by Rossby [69], Haurwitz [32] and Longuet-Higgins [54, 55] are classic examples. In this thesis, following work first introduced by Haurwitz [32], we make no tangent plane simplifications and we use the shallow atmosphere equations for a thin layer of fluid with a free-surface on a rotating sphere. The aim is to incorporate the exact spherical geometry in the governing dynamics.

The shallow atmosphere equations, or shallow water equations if dealing with oceanography, have been used extensively in dynamic meteorological modeling. The paper by Williamson et al. [87] has subsequently generated a large literature of research

papers using the shallow atmosphere equations as a basic test bed for fast global atmospheric solver algorithms (see, e.g. [9], [17], [40], [79]). Their test case 6 employs the Rossby–Haurwitz wave, with parameters similar to those first used by Phillips [66], to initialise the flow state which is subsequently computed at later time steps. While the Rossby–Haurwitz wave is useful here as a flow initialiser, it is important to remember that it is not an exact analytical solution of the full nonlinear shallow atmosphere equations.

Indeed, there is recent numerical evidence by Thuburn & Li [81] that the zonal wavenumber 4 Rossby–Haurwitz wave is dynamically unstable and will eventually break down as the result of an initial perturbation. This agrees in general with previous work conducted by Hoskins [39] and Baines [6] who both found maximum amplitudes beyond which instability of Rossby–Haurwitz waves subject to perturbations was observed. All these results serve to highlight the fact that Rossby–Haurwitz waves, while analytic solutions of the barotropic vorticity equation, are not true solutions of the shallow water equations on a sphere.

Another possible source of instability for Rossby waves could be the presence of nonlinear resonances, as certain key flow parameters are changed. Resonances are known in the water-wave literature, and are characterised by the presence of two or more solution branches in close proximity. Resonances in large-amplitude free-surface waves were apparently first encountered by Wilton [88], in the context of gravity-capillary waves. Schwartz & Vanden-Broeck [72] and Hogan [34, 35, 36] subsequently showed that the small divisors in Wilton’s resonant solutions are indeed associated with multiple solution branches. Forbes [24, 25] encountered a similar phenomenon in waves beneath a floating elastic ice sheet.

In the meteorological context, nonlinear resonance behaviour has been studied by Longuet-Higgins & Gill [57], who showed that long-term resonant interactions can exist between three waves, termed a resonant triad. They found an algebraic relationship relating the individual wavenumbers, associated with each physical dimension, and corresponding wavespeeds; their results are concerned with planetary waves both on the β -plane and more generally on a spherical surface. The instabilities found by both Hoskins [39] and Baines [6] extended this work by calculating amplitudes required for instability based on triad interactions for specific types of Rossby–Haurwitz waves. More recently, Callaghan & Forbes [11] have numerically demonstrated the presence of nonlinear resonance in forced progressive Rossby

wave solutions of the shallow atmosphere equations, with different disjoint solution branches existing at different values of the forcing amplitude. Thus, small perturbations to a Rossby–Haurwitz wave which has been used to initialise a numerical solution of the shallow atmosphere equations, could cause the wave to fluctuate between one solution branch and another in an unpredictable fashion, or break down structurally altogether.

The main goal of this thesis is to extend the above literature by finding numerical solutions of the shallow water equations in the form of progressive Rossby waves that propagate in time without change of shape. Additionally, we aim to explore the relationship that exists between the nonlinear progressive wavespeed and wave amplitude. Two distinct models of the atmosphere are investigated; an incompressible model is first considered and then, in the second half of the thesis, a compressible model is analyzed. The approach is mainly through numerical methods so it must be emphasized at the outset that the task of determining the nature of the exact physical processes that produce some of the subsequently observed results is somewhat hard to discern; a separate analytical study, to which an entire thesis could be devoted, would be needed in many instances. Our aim, therefore, is to uncover key qualitative aspects of progressive Rossby wave solutions for the models under examination.

In Chapter 2 we derive the incompressible shallow atmosphere equations for free-surface fluid flow on a rotating sphere. After non-dimensionalizing, we construct a linearization by first finding a base westerly zonal flow and then perturbing about this state. Solutions are sought in the form of Fourier series with specific symmetry conditions and a standard Galerkin method is used to integrate the linearized equations in closed form, leading to a generalised eigenvalue problem for the wavespeed which is readily solved. Comparison is made to the equivalent Rossby–Haurwitz solutions found in [32], with excellent agreement observed between the separate theories.

In Chapter 3 we extend the linearized solutions computed in Chapter 2 to encompass the full nonlinear equation set for the dynamical system. This allows for the investigation of subtleties in the flow field, resulting from nonlinearity, which are not possible to expose using linear theory alone. We again seek solutions in the form of Fourier series, and a collocation method is used to solve for the unknown Fourier coefficients and wavespeed. The solution is forced by parameterizing the

wave amplitude in terms of one of the unknown Fourier coefficients. A detailed picture is developed of how the progressive wavespeed depends on the wave amplitude, revealing the presence of nonlinear resonances.

A compressible shallow atmosphere model is derived in Chapter 4. It is shown that if the values of the pressure and density on the free-surface are assumed to be zero, which is consistent with the concept of the atmosphere terminating there, then the model almost reduces to the incompressible dynamics, with the only difference being a slightly modified conservation of mass equation. Similar techniques to those used in Chapter 2 are applied to the compressible equations, providing small amplitude linearized solutions of the model.

The solution of the full nonlinear dynamics of the compressible model is accomplished in Chapter 5. The linearized results of Chapter 4 are extended by computing nonlinear solutions via a bootstrapping process, providing detailed information on how the nonlinear progressive wavespeed and amplitude are related. The effect of compressibility is observed to manifest itself via damped resonance behaviour in general.

A brief discussion in Chapter 6 concludes the thesis. In closing, some conjectures are made as to how the results obtained might help explain certain observed atmospheric phenomena. In particular it is proposed that the process of atmospheric blocking is a direct result of critically forced stationary Rossby waves. If this conjecture is true, it would support the blocking theory of multiple equilibria that is popular amongst many theoretical meteorologists. Lastly, a visualisation tool that was developed to aid in interpreting the results, using the OpenGL three dimensional programming interface, is briefly documented in Appendix C.

1.2 Preliminaries

In this section we introduce the coordinate frame and associated conservation equations to be used as the basis of the dynamics throughout the entirety of this thesis. The derivation process is well represented and detailed in any one of a large number of well respected texts on fluid dynamics (see, e.g. Batchelor [8] or Pedlosky [65]), and as such will not be repeated in this work. However, the rotating spherical polar coordinate reference frame system is less well known and requires a small amount of development and clarification, which we present here.

We consider a spherical model Earth of radius a and rotating with constant angular velocity Ω , enveloped by a model incompressible atmosphere, with a free-surface, of depth $h(\lambda, \phi, t)$. A spherical polar coordinate system (r, λ, ϕ) is defined, in which r measures the euclidean distance from the origin of the coordinate system and λ is the azimuthal (longitudinal) angle coordinate. An elevation (latitudinal) coordinate ϕ is also defined as the angle above the equator, so that the North and South poles are represented by $\phi = \pi/2$ and $\phi = -\pi/2$ respectively. This is not the standard definition of polar angle ϕ common in most instances (see, e.g. Kreyszig [44, pages 498-499]), although it is usual practice in meteorology (e.g. Dutton [21], Haltiner & Williams [31], Holton [37]). A schematic diagram illustrating the coordinate system and enveloping atmosphere is given in Figure 1.1.

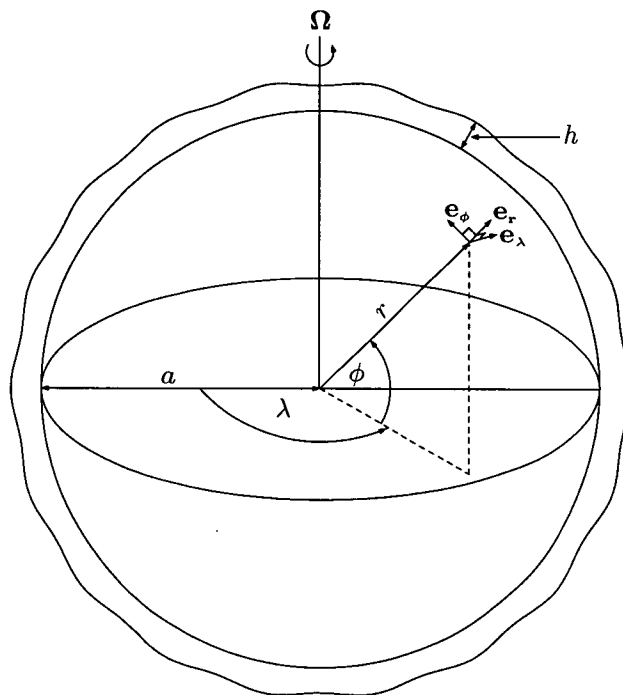


Figure 1.1: Spherical coordinate system with free-surface.

The density and pressure in the atmosphere layer shown in Figure 1.1 are denoted respectively as ρ and p , and g is the magnitude of the acceleration of gravity which is directed radially inwards towards the centre of the sphere so that in vector notation we have $\mathbf{g} = -g \mathbf{e}_r$. An atmospheric velocity vector $\mathbf{q} = u_r \mathbf{e}_r + u_\lambda \mathbf{e}_\lambda + u_\phi \mathbf{e}_\phi$ is introduced, with components u_r, u_λ, u_ϕ in the coordinate directions given by unit vectors $\mathbf{e}_r, \mathbf{e}_\lambda$ and \mathbf{e}_ϕ .

In a reference frame rotating with angular velocity Ω , conservation of mass for an inviscid fluid is expressed through the continuity equation

$$\frac{D\rho}{Dt} + \rho \nabla \cdot \mathbf{q} = 0 \quad (1.1)$$

and conservation of momentum requires the usual Euler equation

$$\frac{D\mathbf{q}}{Dt} + 2\Omega \times \mathbf{q} + \frac{1}{\rho} \nabla p = \mathbf{f}, \quad (1.2)$$

where \mathbf{f} is the combined effect of all body forces per unit mass. The total (substantial) derivative in (1.1) and (1.2) is defined as

$$\frac{D}{Dt} = \frac{\partial}{\partial t} + \mathbf{q} \cdot \nabla, \quad (1.3)$$

and the gradient and divergence operators appearing in (1.1), (1.2) and (1.3) are appropriately defined for the spherical polar coordinate system represented in Figure 1.1.

Conservation of energy, in the absence of viscous dissipation and thermal conduction, is expressed through the first law of thermodynamics and is given mathematically as

$$\rho c_v \frac{DT}{Dt} - \frac{p}{\rho} \frac{D\rho}{Dt} = \rho q_h. \quad (1.4)$$

In (1.4), T is the temperature, c_v is the specific heat at constant volume, and q_h is the rate of heat addition per unit mass by internal heat sources. This study will only be concerned with fluids that are either incompressible, so that the density ρ is constant, or compressible and ideal, so that the ideal gas law of the form

$$p = \rho R T \quad (1.5)$$

can be used to approximate the thermodynamic state relations. The symbol R in (1.5) is the gas constant for dry air and will always take the value of

$$R = 287 \text{ J kg}^{-1} \text{ K}^{-1}$$

in this work.

Because of the rotating reference frame and associated spherical coordinate system, the component forms of (1.1), (1.2) and (1.4) are mathematically complicated and need to be stated here for future reference. The complete set of governing equations in spherical component form is given by (see, e.g. Holton [37, pages 24–28], Pedlosky [65, pages 314–317]),

Mass

$$\begin{aligned} \frac{\partial \rho}{\partial t} + u_r \frac{\partial \rho}{\partial r} + \frac{u_\lambda}{r \cos \phi} \frac{\partial \rho}{\partial \lambda} + \frac{u_\phi}{r} \frac{\partial \rho}{\partial \phi} \\ + \frac{\rho}{r^2 \cos \phi} \left[\frac{\partial}{\partial r} (r^2 u_r \cos \phi) + \frac{\partial}{\partial \lambda} (r u_\lambda) + \frac{\partial}{\partial \phi} (r u_\phi \cos \phi) \right] = 0, \end{aligned} \quad (1.6)$$

 r momentum

$$\frac{\partial u_r}{\partial t} + u_r \frac{\partial u_r}{\partial r} + \frac{u_\lambda}{r \cos \phi} \frac{\partial u_r}{\partial \lambda} + \frac{u_\phi}{r} \frac{\partial u_r}{\partial \phi} - \frac{u_\lambda^2 + u_\phi^2}{r} - 2\Omega u_\lambda \cos \phi + \frac{1}{\rho} \frac{\partial p}{\partial r} = -g, \quad (1.7)$$

 λ momentum

$$\begin{aligned} \frac{\partial u_\lambda}{\partial t} + u_r \frac{\partial u_\lambda}{\partial r} + \frac{u_\lambda}{r \cos \phi} \frac{\partial u_\lambda}{\partial \lambda} + \frac{u_\phi}{r} \frac{\partial u_\lambda}{\partial \phi} \\ + \frac{u_r u_\lambda - u_\lambda u_\phi \tan \phi}{r} + 2\Omega(u_r \cos \phi - u_\phi \sin \phi) + \frac{1}{\rho r \cos \phi} \frac{\partial p}{\partial \lambda} = 0, \end{aligned} \quad (1.8)$$

 ϕ momentum

$$\begin{aligned} \frac{\partial u_\phi}{\partial t} + u_r \frac{\partial u_\phi}{\partial r} + \frac{u_\lambda}{r \cos \phi} \frac{\partial u_\phi}{\partial \lambda} + \frac{u_\phi}{r} \frac{\partial u_\phi}{\partial \phi} \\ + \frac{u_r u_\phi + u_\lambda^2 \tan \phi}{r} + 2\Omega u_\lambda \sin \phi + \frac{1}{\rho r} \frac{\partial p}{\partial \phi} = 0, \end{aligned} \quad (1.9)$$

Energy

$$\begin{aligned} \rho c_v \left[\frac{\partial T}{\partial t} + u_r \frac{\partial T}{\partial r} + \frac{u_\lambda}{r \cos \phi} \frac{\partial T}{\partial \lambda} + \frac{u_\phi}{r} \frac{\partial T}{\partial \phi} \right] \\ - \frac{p}{\rho} \left[\frac{\partial \rho}{\partial t} + u_r \frac{\partial \rho}{\partial r} + \frac{u_\lambda}{r \cos \phi} \frac{\partial \rho}{\partial \lambda} + \frac{u_\phi}{r} \frac{\partial \rho}{\partial \phi} \right] = \rho q_h, \end{aligned} \quad (1.10)$$

Gas Law

$$p = \rho R T. \quad (1.11)$$

Equations (1.6)–(1.11) form a closed set, for field variables u_r , u_λ , u_ϕ , p , ρ and T , that model compressible ideal fluid flow in a rotating spherical reference frame. The complexity of the equations all but rules out analytical solutions in closed form, except for the simplest of flows. Consequently it is almost always necessary to make idealizations and approximations that yield simplified governing equations which facilitate the solution process and understanding. The shallow atmosphere, or shallow water, approximation is one such method that can be used to simplify the equations of motion. This technique is introduced in the next chapter.

CHAPTER 2

INCOMPRESSIBLE LINEARIZED SHALLOW ATMOSPHERE MODEL

2.1 Derivation

We consider here the basic derivation of the incompressible shallow atmosphere equations following the general approach developed in Pedlosky[65, pages 57–63]. However, as opposed to the rotating cartesian form derived in [65], we initially start in a rotating spherical coordinate system, thus allowing for the curved geometry of the spherical Earth to be appropriately incorporated into the resulting equation set.

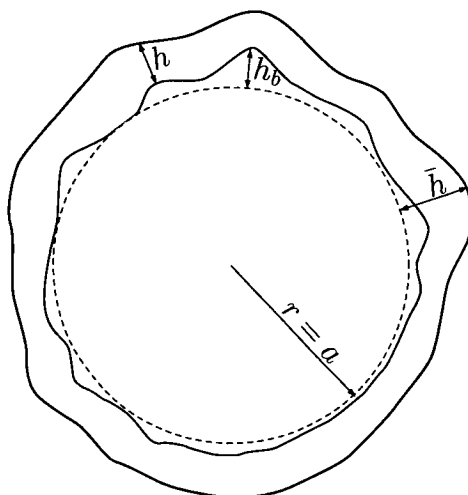


Figure 2.1: Free-surface height parameters

Commencing the derivation we define \bar{h} as the height of a free-surface surrounding a rotating reference sphere of radius $r = a$ as depicted in Figure 2.1. We measure \bar{h}

as the radial distance from the level surface $r = a$ of the spherical coordinate system to the free-surface. Additionally, define h and h_b as the depth of the fluid and the height of the underlying mountains respectively. The height of the free-surface \bar{h} can be given in terms of the two parameters h and h_b as

$$\bar{h} = h_b + h. \quad (2.1)$$

Although the generality of this setup affords the representation of a much wider class of problem we will restrict ourselves to the case when there is no underlying mountain specification so that $h_b = 0$, leading to

$$\bar{h} = h. \quad (2.2)$$

Because we are only concerned with incompressible flow in Chapters 2 and 3, the equations of motion presented in Chapter 1 will reduce significantly. In particular, since density ρ is constant the mass equation, (1.1), reduces to the form $\nabla \cdot \mathbf{q} = 0$. In addition, we can discard all thermodynamic behaviour, allowing us to remove the energy and ideal gas equations from the governing system. We also note that, due to the nature of the spherical coordinate system, the vertical coordinate r appears explicitly in the dynamical equations. Holton [37, page 24] points out that these curvature terms can be adequately approximated by $r = a$ since the depth of the atmosphere h is assumed to be much smaller than the radius of the earth. Adopting the above approximations and simplifications we obtain the following form for the incompressible dynamical equations.

Mass

$$a \cos \phi \frac{\partial u_r}{\partial r} + \frac{\partial u_\lambda}{\partial \lambda} + \frac{\partial}{\partial \phi} (u_\phi \cos \phi) = 0, \quad (2.3)$$

r momentum

$$\frac{\partial u_r}{\partial t} + u_r \frac{\partial u_r}{\partial r} + \frac{u_\lambda}{a \cos \phi} \frac{\partial u_r}{\partial \lambda} + \frac{u_\phi}{a} \frac{\partial u_r}{\partial \phi} - \frac{u_\lambda^2 + u_\phi^2}{a} - 2\Omega u_\lambda \cos \phi + \frac{1}{\rho} \frac{\partial p}{\partial r} = -g, \quad (2.4)$$

λ momentum

$$\begin{aligned} \frac{\partial u_\lambda}{\partial t} + u_r \frac{\partial u_\lambda}{\partial r} + \frac{u_\lambda}{a \cos \phi} \frac{\partial u_\lambda}{\partial \lambda} + \frac{u_\phi}{a} \frac{\partial u_\lambda}{\partial \phi} + \frac{u_r u_\lambda - u_\lambda u_\phi \tan \phi}{a} \\ + 2\Omega(u_r \cos \phi - u_\phi \sin \phi) + \frac{1}{a \rho \cos \phi} \frac{\partial p}{\partial \lambda} = 0, \end{aligned} \quad (2.5)$$

ϕ momentum

$$\begin{aligned} \frac{\partial u_\phi}{\partial t} + u_r \frac{\partial u_\phi}{\partial r} + \frac{u_\lambda}{a \cos \phi} \frac{\partial u_\phi}{\partial \lambda} + \frac{u_\phi}{a} \frac{\partial u_\phi}{\partial \phi} + \frac{u_r u_\phi + u_\lambda^2 \tan \phi}{a} \\ + 2\Omega u_\lambda \sin \phi + \frac{1}{a\rho} \frac{\partial p}{\partial \phi} = 0. \end{aligned} \quad (2.6)$$

The underlying assumption of the shallow atmosphere approximation is that motion mainly occurs in the λ - ϕ plane and less so in the r direction, effectively confining the velocity to predominantly “horizontal” motion. Mathematically we can write this statement as

$$u_r \approx O(\epsilon), \quad (2.7)$$

$$u_\lambda \approx O(1), \quad (2.8)$$

$$u_\phi \approx O(1), \quad (2.9)$$

where ϵ is a small parameter that reflects the shallowness of the atmosphere relative to the radius of the Earth. In effect, ϵ might be regarded as the ratio h/a which is typically of order 10^{-3} for the Earth. Consider now the implications of this approximation for the r momentum equation (2.4). We argue that the total derivative terms $\frac{\partial u_r}{\partial t}$, $u_r \frac{\partial u_r}{\partial r}$, $\frac{u_\lambda}{a \cos \phi} \frac{\partial u_r}{\partial \lambda}$ and $\frac{u_\phi}{a} \frac{\partial u_r}{\partial \phi}$ are all $O(\epsilon)$ so that the r momentum equation reduces to

$$-\frac{u_\lambda^2 + u_\phi^2}{a} - 2\Omega u_\lambda \cos \phi + \frac{1}{\rho} \frac{\partial p}{\partial r} = -g, \quad (2.10)$$

where only terms of $O(1)$ have been retained. Finally, we assume that (2.10) is dominated by hydrostaticsⁱ, so that effectively we have

$$\frac{\partial p}{\partial r} = -\rho g. \quad (2.11)$$

Equation (2.11) can be integrated with respect to r , yielding

$$p(r, \lambda, \phi, t) = -\rho g r + f(\lambda, \phi, t). \quad (2.12)$$

We fix the value of $f(\lambda, \phi, t)$ by assuming that, on the free-surface $r = a + \bar{h}(\lambda, \phi, t)$, the pressure has the constant value p_0 so that

$$p(r, \lambda, \phi, t) = p_0 + \rho g(a + \bar{h}(\lambda, \phi, t) - r). \quad (2.13)$$

ⁱWe can be more rigorous and use a scale analysis approach to argue this point. See Pedlosky[65, page 60] for the finer details of this process

From (2.13) we immediately obtain

$$\frac{\partial p}{\partial \lambda} = \rho g \frac{\partial \bar{h}}{\partial \lambda}, \quad (2.14)$$

$$\frac{\partial p}{\partial \phi} = \rho g \frac{\partial \bar{h}}{\partial \phi}, \quad (2.15)$$

implying that the horizontal pressure gradient components are independent of r , which in turn implies that the horizontal accelerations must be r -independent also. It is therefore consistent (see Pedlosky [65, page 61]) to assume that the horizontal velocity components are also r -independent if they are initially so. Thus we must have

$$u_\lambda \equiv u_\lambda(\lambda, \phi, t), \quad (2.16)$$

$$u_\phi \equiv u_\phi(\lambda, \phi, t), \quad (2.17)$$

so that, in conjunction with (2.7), the two remaining momentum equations, (2.5) and (2.6), taken to $O(1)$ become

λ momentum

$$\frac{\partial u_\lambda}{\partial t} + \frac{u_\lambda}{a \cos \phi} \frac{\partial u_\lambda}{\partial \lambda} + \frac{u_\phi}{a} \frac{\partial u_\lambda}{\partial \phi} - \frac{u_\lambda u_\phi \tan \phi}{a} - 2\Omega u_\phi \sin \phi + \frac{g}{a \rho \cos \phi} \frac{\partial \bar{h}}{\partial \lambda} = 0, \quad (2.18)$$

ϕ momentum

$$\frac{\partial u_\phi}{\partial t} + \frac{u_\lambda}{a \cos \phi} \frac{\partial u_\phi}{\partial \lambda} + \frac{u_\phi}{a} \frac{\partial u_\phi}{\partial \phi} + \frac{u_\lambda^2 \tan \phi}{a} + 2\Omega u_\lambda \sin \phi + \frac{g}{a \rho} \frac{\partial \bar{h}}{\partial \phi} = 0. \quad (2.19)$$

We now turn our attention to the mass equation and note that since u_λ and u_ϕ are r -independent we can integrate (2.3) with respect to r to give

$$a \cos \phi u_r(r, \lambda, \phi, t) = -r \left[\frac{\partial u_\lambda}{\partial \lambda} + \frac{\partial}{\partial \phi} (u_\phi \cos \phi) \right] + \tilde{u}_r(\lambda, \phi, t). \quad (2.20)$$

To determine the nature of \tilde{u}_r we need to examine the boundary conditions on the upper and lower boundaries $r = a + \bar{h}$ and $r = a + h_b$ respectively. On the lower boundary we must have no normal flow, otherwise the fluid would penetrate the surface and breach the conservation of mass requirement. Thus on $r = a + h_b$ we must enforce the condition $\mathbf{q} \cdot \mathbf{n} = 0$ where \mathbf{n} is a normal to the surface $r = a + h_b$. We can easily show that the normal to the lower boundary is given by

$$\mathbf{n} = \mathbf{e}_r - \frac{1}{a \cos \phi} \frac{\partial h_b}{\partial \lambda} \mathbf{e}_\lambda - \frac{1}{a} \frac{\partial h_b}{\partial \phi} \mathbf{e}_\phi, \quad (2.21)$$

so that

$$\mathbf{q} \cdot \mathbf{n} = u_r(a + h_b, \lambda, \phi, t) - \frac{u_\lambda}{a \cos \phi} \frac{\partial h_b}{\partial \lambda} - \frac{u_\phi}{a} \frac{\partial h_b}{\partial \phi} = 0. \quad (2.22)$$

Solving for u_r we obtain

$$u_r(a + h_b, \lambda, \phi, t) = \frac{u_\lambda}{a \cos \phi} \frac{\partial h_b}{\partial \lambda} + \frac{u_\phi}{a} \frac{\partial h_b}{\partial \phi}. \quad (2.23)$$

Substituting (2.23) into (2.20) and evaluating at $r = a + h_b$ allows us to solve for \tilde{u}_r , which we in turn substitute back into (2.20). After simplification we arrive at

$$\begin{aligned} a \cos \phi u_r(r, \lambda, \phi, t) = & -r \left[\frac{\partial u_\lambda}{\partial \lambda} + \frac{\partial}{\partial \phi} (u_\phi \cos \phi) \right] + \frac{\partial}{\partial \lambda} (u_\lambda h_b) \\ & + \frac{\partial}{\partial \phi} (u_\phi h_b \cos \phi). \end{aligned} \quad (2.24)$$

On the upper boundary we enforce the kinematic condition

$$\frac{D}{Dt} [r - a - \bar{h}(\lambda, \phi, t)] = 0,$$

which states that the fluid can not penetrate the free-surface. Expanding the total derivative and solving for u_r gives

$$u_r(h, \lambda, \phi, t) = \frac{\partial \bar{h}}{\partial t} + \frac{u_\lambda}{a \cos \phi} \frac{\partial \bar{h}}{\partial \lambda} + \frac{u_\phi}{a} \frac{\partial \bar{h}}{\partial \phi}. \quad (2.25)$$

Finally, substitution of (2.25) into (2.24) and subsequent simplification yields the incompressible shallow atmosphere mass equation given by

$$a \cos \phi \frac{\partial \bar{h}}{\partial t} + \frac{\partial}{\partial \lambda} (u_\lambda (\bar{h} - h_b)) + \frac{\partial}{\partial \phi} (u_\phi (\bar{h} - h_b) \cos \phi) = 0. \quad (2.26)$$

We note that since $h = \bar{h} - h_b$, expanding all differential products and writing $f = 2\Omega \sin \phi$, we can express the complete dimensional dynamical equations of motion for an incompressible fluid in a rotating spherical coordinate system as

mass

$$\frac{\partial h}{\partial t} + \frac{u_\lambda}{a \cos \phi} \frac{\partial h}{\partial \lambda} + \frac{u_\phi}{a} \frac{\partial h}{\partial \phi} + \frac{h}{a \cos \phi} \left[\frac{\partial u_\lambda}{\partial \lambda} + \cos \phi \frac{\partial u_\phi}{\partial \phi} - u_\phi \sin \phi \right] = 0, \quad (2.27)$$

λ momentum

$$\frac{\partial u_\lambda}{\partial t} + \frac{u_\lambda}{a \cos \phi} \frac{\partial u_\lambda}{\partial \lambda} + \frac{u_\phi}{a} \frac{\partial u_\lambda}{\partial \phi} - \left(f + \frac{u_\lambda}{a} \tan \phi \right) u_\phi + \frac{g}{a \cos \phi} \frac{\partial h}{\partial \lambda} = 0, \quad (2.28)$$

ϕ momentum

$$\frac{\partial u_\phi}{\partial t} + \frac{u_\lambda}{a \cos \phi} \frac{\partial u_\phi}{\partial \lambda} + \frac{u_\phi}{a} \frac{\partial u_\phi}{\partial \phi} + \left(f + \frac{u_\lambda}{a} \tan \phi \right) u_\lambda + \frac{g}{a} \frac{\partial h}{\partial \phi} = 0. \quad (2.29)$$

The above form is that given by Williamson et al.[87, page 213] as the advective form of the shallow atmosphere equations and this is the form we shall subsequently use for all analysis in this chapter.

2.2 Progressive-Wave Coordinate Transform

We are interested in solutions to equations (2.27), (2.28) and (2.29) that are of the form of a progressive-wave with constant angular velocity. Defining c to be an angular wavespeed we now construct a new moving coordinate frame that depends on λ and t in the form

$$\eta = \lambda - ct. \quad (2.30)$$

The effect of the $-ct$ term is to translate any initial wave structure either towards the west ($c < 0$) or towards the east ($c > 0$) with constant angular speed c . Since we have defined a new coordinate system we need to establish how the equations of motion are represented in this new reference frame. Applying the chain rule we can easily show that, for some scalar field $\Psi(\eta, \phi)$,

$$\frac{\partial \Psi}{\partial \lambda} = \frac{\partial \Psi}{\partial \eta} \frac{\partial \eta}{\partial \lambda} = \frac{\partial \Psi}{\partial \eta}, \quad (2.31)$$

$$\frac{\partial \Psi}{\partial t} = \frac{\partial \Psi}{\partial \eta} \frac{\partial \eta}{\partial t} = -c \frac{\partial \Psi}{\partial \eta}. \quad (2.32)$$

Using this transformation we can now write equations (2.27), (2.28) and (2.29) as

mass

$$\left(\frac{u_\lambda}{a} - c \cos \phi \right) \frac{\partial h}{\partial \eta} + \frac{u_\phi \cos \phi}{a} \frac{\partial h}{\partial \phi} + \frac{h}{a} \left[\frac{\partial u_\lambda}{\partial \eta} + \cos \phi \frac{\partial u_\phi}{\partial \phi} - u_\phi \sin \phi \right] = 0, \quad (2.33)$$

λ momentum

$$\left(\frac{u_\lambda}{a} - c \cos \phi \right) \frac{\partial u_\lambda}{\partial \eta} + \frac{u_\phi \cos \phi}{a} \frac{\partial u_\lambda}{\partial \phi} - \left(f \cos \phi + \frac{u_\lambda}{a} \sin \phi \right) u_\phi + \frac{g}{a} \frac{\partial h}{\partial \eta} = 0, \quad (2.34)$$

ϕ momentum

$$\left(\frac{u_\lambda}{a} - c \cos \phi \right) \frac{\partial u_\phi}{\partial \eta} + \frac{u_\phi \cos \phi}{a} \frac{\partial u_\phi}{\partial \phi} + \left(f \cos \phi + \frac{u_\lambda}{a} \sin \phi \right) u_\lambda + \frac{g \cos \phi}{a} \frac{\partial h}{\partial \phi} = 0, \quad (2.35)$$

where we have multiplied each equation by $\cos \phi$ to remove apparent polar singularities that would otherwise adversely affect numerical computations, and we have also retained the name “ λ momentum” to remind us of the fact that equation (2.34) is essentially still the λ component of conservation of momentum despite the transformation to η .

2.3 Non-dimensionalization of the Governing Equations

In an attempt to generalise the analysis, it is desirable to express the governing partial differential equations in a form that is independent of the specific units used to measure the variables of the problem. For this reason we non-dimensionalize each of the governing equations to expose the underlying qualitative behaviour. The particular approach adopted here is similar to that used by Klein [42, page 766] in that we reduce our dimensionless parameters to the set of familiar fluid dynamical parameters comprised of Strouhal number, Froude number and Rossby number.

First we define the following characteristic values, for each reference scale contained in the problem, as

$$v_{\text{ref}} \equiv \text{characteristic speed,}$$

$$h_{\text{ref}} \equiv \text{characteristic free-surface height,}$$

$$c_{\text{ref}} \equiv \text{characteristic angular velocity.}$$

Using these dimensional parameters we now rescale all the field variables to dimensionless form giving

$$\hat{u}_\lambda = \frac{u_\lambda}{v_{\text{ref}}} \Rightarrow u_\lambda = v_{\text{ref}} \hat{u}_\lambda, \quad (2.36)$$

$$\hat{u}_\phi = \frac{u_\phi}{v_{\text{ref}}} \Rightarrow u_\phi = v_{\text{ref}} \hat{u}_\phi, \quad (2.37)$$

$$\hat{h} = \frac{h}{h_{\text{ref}}} \Rightarrow h = h_{\text{ref}} \hat{h}, \quad (2.38)$$

$$\hat{c} = \frac{c}{c_{\text{ref}}} \Rightarrow c = c_{\text{ref}} \hat{c}, \quad (2.39)$$

where the hat ($\hat{\cdot}$) denotes a dimensionless variable. Substituting equations (2.36)–(2.39) into (2.33), (2.34), (2.35) and manipulating, we obtain

mass

$$\left(\hat{u}_\lambda - \frac{c_{\text{ref}} a}{v_{\text{ref}}} \hat{c} \cos \phi \right) \frac{\partial \hat{h}}{\partial \eta} + \hat{u}_\phi \cos \phi \frac{\partial \hat{h}}{\partial \phi} + \hat{h} \left[\frac{\partial \hat{u}_\lambda}{\partial \eta} + \cos \phi \frac{\partial \hat{u}_\phi}{\partial \phi} - \hat{u}_\phi \sin \phi \right] = 0, \quad (2.40)$$

λ momentum

$$\left(\hat{u}_\lambda - \frac{c_{\text{ref}} a}{v_{\text{ref}}} \hat{c} \cos \phi \right) \frac{\partial \hat{u}_\lambda}{\partial \eta} + \hat{u}_\phi \cos \phi \frac{\partial \hat{u}_\lambda}{\partial \phi} - \left(\frac{2\Omega a}{v_{\text{ref}}} \cos \phi + \hat{u}_\lambda \right) \hat{u}_\phi \sin \phi + \frac{gh_{\text{ref}}}{v_{\text{ref}}^2} \frac{\partial \hat{h}}{\partial \eta} = 0, \quad (2.41)$$

ϕ momentum

$$\left(\hat{u}_\lambda - \frac{c_{\text{ref}} a}{v_{\text{ref}}} \hat{c} \cos \phi \right) \frac{\partial \hat{u}_\phi}{\partial \eta} + \hat{u}_\phi \cos \phi \frac{\partial \hat{u}_\phi}{\partial \phi} + \left(\frac{2\Omega a}{v_{\text{ref}}} \cos \phi + \hat{u}_\lambda \right) \hat{u}_\lambda \sin \phi + \frac{gh_{\text{ref}} \cos \phi}{v_{\text{ref}}^2} \frac{\partial \hat{h}}{\partial \phi} = 0, \quad (2.42)$$

where we have also replaced the Coriolis parameter f by its definition $f = 2\Omega \sin \phi$.

Three obvious dimensionless parameter groupings emerge from this process. These are just the familiar flow regime parameters from fluid dynamics given as

$$\begin{aligned} \text{Sr} &= \frac{a c_{\text{ref}}}{v_{\text{ref}}} && \text{Strouhal number,} \\ \text{Fr} &= \frac{v_{\text{ref}}}{\sqrt{gh_{\text{ref}}}} && \text{Froude number,} \\ \text{Ro} &= \frac{v_{\text{ref}}}{2\Omega a} && \text{Rossby number.} \end{aligned}$$

Substitution of these parameters into our governing equations yields

mass

$$(\hat{u}_\lambda - \text{Sr} \hat{c} \cos \phi) \frac{\partial \hat{h}}{\partial \eta} + \hat{u}_\phi \cos \phi \frac{\partial \hat{h}}{\partial \phi} + \hat{h} \left[\frac{\partial \hat{u}_\lambda}{\partial \eta} + \cos \phi \frac{\partial \hat{u}_\phi}{\partial \phi} - \hat{u}_\phi \sin \phi \right] = 0, \quad (2.43)$$

λ momentum

$$(\hat{u}_\lambda - \text{Sr} \hat{c} \cos \phi) \frac{\partial \hat{u}_\lambda}{\partial \eta} + \hat{u}_\phi \cos \phi \frac{\partial \hat{u}_\lambda}{\partial \phi} - \left(\frac{\cos \phi}{\text{Ro}} + \hat{u}_\lambda \right) \hat{u}_\phi \sin \phi + \frac{1}{\text{Fr}^2} \frac{\partial \hat{h}}{\partial \eta} = 0, \quad (2.44)$$

ϕ momentum

$$(\hat{u}_\lambda - \text{Sr} \hat{c} \cos \phi) \frac{\partial \hat{u}_\phi}{\partial \eta} + \hat{u}_\phi \cos \phi \frac{\partial \hat{u}_\phi}{\partial \phi} + \left(\frac{\cos \phi}{\text{Ro}} + \hat{u}_\lambda \right) \hat{u}_\lambda \sin \phi + \frac{\cos \phi}{\text{Fr}^2} \frac{\partial \hat{h}}{\partial \phi} = 0, \quad (2.45)$$

which is the final form for the non-dimensional incompressible shallow atmosphere equations on a rotating sphere.

2.4 Linearization of the Equations

2.4.1 Base Zonal Flow Derivation

As previously discussed in Chapter 1 it is convenient to consider Rossby waves as consisting of latitudinal perturbations about an underlying zonal flow structure. Thus it is important to know the exact nature of the zonal flow in order to calculate

the resulting perturbations. Following the work of Haurwitz[32, page 255] we choose the simplest zonal flow in the form of a super rotation that only depends on latitude and additionally has $u_\phi = 0^{\text{ii}}$. The form for our zonal flow is then given by

$$u_{\lambda z} = \omega \cos \phi, \quad (2.46)$$

$$u_{\phi z} = 0, \quad (2.47)$$

$$h_z = H(\phi), \quad (2.48)$$

where the parameter ω is the non-dimensional representation of the base angular speed of the flow and the subscript z is used to denote field variables belonging to the zonal flow structure. The problem now reduces to finding the function $H(\phi)$ that makes equations (2.46), (2.47) and (2.48) a solution of equations (2.43), (2.44) and (2.45).

Direct substitution reveals that the only equation not identically satisfied by the zonal flow structure is the ϕ momentum equation, which yields the ordinary differential equation

$$\frac{dH}{d\phi} = -\omega \text{Fr}^2 \left(\frac{1}{\text{Ro}} + \omega \right) \sin \phi \cos \phi. \quad (2.49)$$

This integrates easily to give

$$H(\phi) = h_o + \frac{\omega \text{Fr}^2}{2} \left(\frac{1}{\text{Ro}} + \omega \right) \cos^2 \phi. \quad (2.50)$$

The constant of integration h_o can be viewed as the base non-dimensional height of the free-surface at the poles and typically we would choose $h_o = 1$ so that the dimensional value of h_z at $\phi = \pm\pi/2$ is h_{ref} . The two parameters ω and h_o suffice to specify uniquely any given super rotation and associated total mass, or volume in the incompressible case, of the system. We note here that in order to make comparison between results with differing values of ω it is necessary to modify the value of h_o so that the total volume of fluid in $a + h_b \leq r \leq a + \bar{h}$ remains constant. This amounts to solving a cubic equation for h_o once a fixed volume and value for ω have been decided upon.

ⁱⁱAlthough all variables are dimensionless, from now on, for the sake of brevity, we drop the hat ($\hat{}$) notation and all variables will be assumed dimensionless unless otherwise stated.

In summary, we have shown that a basic zonal flow structure is given by

$$u_{\lambda z} = \omega \cos \phi, \quad (2.51)$$

$$u_{\phi z} = 0, \quad (2.52)$$

$$h_z = h_o + \frac{\omega \text{Fr}^2}{2} \left(\frac{1}{\text{Ro}} + \omega \right) \cos^2 \phi. \quad (2.53)$$

2.4.2 Linearization about the Base Zonal Flow

Given the base zonal flow we now consider $O(\epsilon)$ perturbations about this flow state by constructing the perturbation expansions

$$u_\lambda(\eta, \phi) = u_{\lambda z} + \epsilon u_{\lambda 1}(\eta, \phi) + O(\epsilon^2), \quad (2.54)$$

$$u_\phi(\eta, \phi) = 0 + \epsilon u_{\phi 1}(\eta, \phi) + O(\epsilon^2), \quad (2.55)$$

$$h(\eta, \phi) = h_z + \epsilon h_1(\eta, \phi) + O(\epsilon^2). \quad (2.56)$$

The perturbation parameter ϵ is a small quantity that represents the maximum deviation about the zonal flow. It is instructive to think of ϵ as a wave amplitude in this case, although it must be emphasized that the linearization is only valid for infinitely small amplitude and consequently our results will only be accurate as $\epsilon \rightarrow 0$. Nonetheless we can expect reasonable results for small values of ϵ .

Substituting the perturbation expansions (2.54)–(2.56) into the governing equations (2.43)–(2.45) leads to the set of partial differential equations given by

mass

$$\begin{aligned} \epsilon (u_{\lambda z} - \text{Sr } c \cos \phi) \frac{\partial h_1}{\partial \eta} + \epsilon u_{\phi 1} \cos \phi \frac{d h_z}{d \phi} \\ + \epsilon h_z \left[\frac{\partial u_{\lambda 1}}{\partial \eta} + \cos \phi \frac{\partial u_{\phi 1}}{\partial \phi} - u_{\phi 1} \sin \phi \right] + O(\epsilon^2) = 0, \end{aligned} \quad (2.57)$$

λ momentum

$$\begin{aligned} \epsilon (u_{\lambda z} - \text{Sr } c \cos \phi) \frac{\partial u_{\lambda 1}}{\partial \eta} + \epsilon u_{\phi 1} \cos \phi \frac{d u_{\lambda z}}{d \phi} - \epsilon \left(\frac{\cos \phi}{\text{Ro}} + u_{\lambda z} \right) u_{\phi 1} \sin \phi \\ + \frac{1}{\text{Fr}^2} \frac{\partial h_1}{\partial \eta} + O(\epsilon^2) = 0, \end{aligned} \quad (2.58)$$

ϕ momentum

$$\begin{aligned} \left(\frac{\cos \phi}{\text{Ro}} + u_{\lambda z} \right) u_{\lambda z} \sin \phi + \frac{\cos \phi}{\text{Fr}^2} \frac{d h_z}{d \phi} + \epsilon (u_{\lambda z} - \text{Sr } c \cos \phi) \frac{\partial u_{\phi 1}}{\partial \eta} \\ + \epsilon \left(\frac{\cos \phi}{\text{Ro}} + 2u_{\lambda z} \right) u_{\lambda 1} \sin \phi + \frac{\cos \phi}{\text{Fr}^2} \frac{\partial h_1}{\partial \phi} + O(\epsilon^2) = 0. \end{aligned} \quad (2.59)$$

The $O(1)$ terms in (2.59) are satisfied identically by the base zonal flow. By putting $u_{\lambda z} = \omega \cos \phi$ into the above equations we obtain the $O(\epsilon)$ equations that define the first level of corrections in our perturbation expansions. These equations are

mass

$$(\omega - \text{Sr } c) \cos \phi \frac{\partial h_1}{\partial \eta} + u_{\phi 1} \cos \phi \frac{d h_z}{d \phi} + h_z \left[\frac{\partial u_{\lambda 1}}{\partial \eta} + \cos \phi \frac{\partial u_{\phi 1}}{\partial \phi} - u_{\phi 1} \sin \phi \right] = 0, \quad (2.60)$$

λ momentum

$$(\omega - \text{Sr } c) \cos \phi \frac{\partial u_{\lambda 1}}{\partial \eta} - \left(\frac{1}{\text{Ro}} + 2\omega \right) u_{\phi 1} \sin \phi \cos \phi + \frac{1}{\text{Fr}^2} \frac{\partial h_1}{\partial \eta} = 0, \quad (2.61)$$

ϕ momentum

$$(\omega - \text{Sr } c) \cos \phi \frac{\partial u_{\phi 1}}{\partial \eta} + \left(\frac{1}{\text{Ro}} + 2\omega \right) u_{\lambda 1} \sin \phi \cos \phi + \frac{\cos \phi}{\text{Fr}^2} \frac{\partial h_1}{\partial \phi} = 0. \quad (2.62)$$

The solution of (2.60), (2.61) and (2.62) is facilitated by noting that we may write each of the $O(\epsilon)$ perturbation terms as the product of a Fourier mode in η with a function of ϕ . Thus we define

$$u_{\lambda 1}(\eta, \phi) = \cos(\kappa \eta) \Lambda(\phi), \quad (2.63)$$

$$u_{\phi 1}(\eta, \phi) = \sin(\kappa \eta) \Phi(\phi), \quad (2.64)$$

$$h_1(\eta, \phi) = \cos(\kappa \eta) \mathcal{H}(\phi), \quad (2.65)$$

where the parity of the Fourier basis in η in each term is chosen to preserve the overall parity of each dynamical equation. Alternatively, it would be possible to interchange the sin and cos terms in (2.63)–(2.65), with the effect of rotating the solution at $t = 0$ by π/κ . Also note that the parameter κ has been introduced as a way of specifying the wavenumber of the solution. This is a natural addition to the model since intuitively we would expect that the wavespeed c will depend on the number of equally spaced wavelengths around a latitude circle.

By defining our $O(\epsilon)$ terms according to (2.63)–(2.65) we can remove the η dependence entirely from the partial differential equations, transforming them into a set of ordinary differential and algebraic equations given by

mass

$$\begin{aligned} -\kappa(\omega - \text{Sr } c) \cos \phi \mathcal{H}(\phi) + \Phi(\phi) \cos \phi \frac{d h_z}{d \phi} \\ + h_z \left[-\kappa \Lambda(\phi) + \cos \phi \frac{d \Phi(\phi)}{d \phi} - \Phi(\phi) \sin \phi \right] = 0, \end{aligned} \quad (2.66)$$

λ momentum

$$-\kappa(\omega - \text{Sr}c) \cos\phi \Lambda(\phi) - \left(\frac{1}{\text{Ro}} + 2\omega\right) \Phi(\phi) \sin\phi \cos\phi - \frac{\kappa}{\text{Fr}^2} \mathcal{H}(\phi) = 0, \quad (2.67)$$

ϕ momentum

$$\kappa(\omega - \text{Sr}c) \Phi(\phi) + \left(\frac{1}{\text{Ro}} + 2\omega\right) \Lambda(\phi) \sin\phi + \frac{1}{\text{Fr}^2} \frac{d\mathcal{H}(\phi)}{d\phi} = 0. \quad (2.68)$$

2.5 Numerical Solution of the Linearized Equations

2.5.1 Series Representation

The numerical solution of (2.66), (2.67) and (2.68) can be accomplished by approximating each of $\Lambda(\phi)$, $\Phi(\phi)$ and $\mathcal{H}(\phi)$ with truncated series of basis functions. As noted by Boyd[10, page 109], the particular choice of basis function is primarily governed by the geometry involved in the problem. The inherent spherical geometry in the shallow atmosphere problem can be adequately described by using either spherical harmonics or Fourier basis functions, which both cope well with periodic boundary conditions. Although the generally accepted solution approach for problems in spherical geometry, in both meteorological and mathematical circles, is via the spherical harmonics, the sheer simplicity and ease of use of Fourier series is an attractive alternative that, as will be demonstrated shortly, allows for some further analytical manipulation to be carried out, greatly reducing the computational time for any given solution.

The particular form of the Fourier basis components needs careful consideration, primarily because we can identify key symmetry and boundary conditions that each of the field variables must satisfy. In this study we are only concerned with special types of solutions that obey the following set of conditions:

- u_λ and h are symmetric with respect to the equator ($\phi = 0$),
- u_ϕ is anti-symmetric with respect to the equator,
- u_λ and u_ϕ are zero at the poles ($\phi = \pm\pi/2$),
- h is constant at the poles.

From an analysis of the problem we can show that $\Lambda(\phi)$ and $\mathcal{H}(\phi)$ must be symmetric with respect to the equator whilst $\Phi(\phi)$ must be antisymmetric. This basically says

that a northward velocity deflection in the northern hemisphere is equivalent to a southward velocity deflection in the southern hemisphere, whereas the free-surface has the same height at points $(\eta_0, \pm\phi_0)$. From the above list of solution requirements we can also deduce that the $O(\epsilon)$ field variables must all have zero value at the poles. This is necessary because we have convergence of lines of longitude at $\phi = \pm\pi/2$ and hence to avoid multi-valued functions for the field variables we require that the perturbations are all zero at the polesⁱⁱⁱ.

Although the above list of solution requirements might seem, at first glance, to be rather restrictive there is much to be gained by employing such an approach. The main advantage of this formulation is that difficulties at the poles are avoided; this can be a common source of numerical trouble in models that account for the spherical geometry. The pole problem amounts to the previously mentioned dilemma of having multi-valued functions defining the flow field and the apparent switching of East to West (or North to South) as one traverses across a pole of the spherical coordinate system. A common approach to navigate this troublesome numerical stumbling block is to introduce new velocity components that are multiplied by Fourier functions that correctly adjust for the parity change on either side of the pole as detailed in Duran[20, page 207]. In our approach no such adjustments are required since by forcing the flow to have stagnation points at each pole we will never encounter a scenario in which flow with an eastward or northward component suddenly switches to flow having a westward or southward component. Of course, in all realistic global circulation models the handling of the pole problem becomes an integral feature of any time integrating computation since in general stagnation points are not situated at both poles. Nonetheless, the advantages to be had by adopting our approach coupled with the motive of theoretical investigation justify its use.

We are now in a position to construct the series approximations. For now we just state the forms for the $O(\epsilon)$ linear terms, deferring the statement of the series for the full nonlinear terms until Chapter 3 when we approach the solution of the full nonlinear system. The functions that meet our prescribed conditions above can be

ⁱⁱⁱIn general $\mathcal{H}(\phi)$ need only be constant at the poles; however the allowed values for the parameter κ effectively force $\mathcal{H}(\pm\frac{\pi}{2}) = 0$.

given by

$$\Lambda(\phi) = \sum_{n=1}^{\infty} P_{\kappa,n} \cos((2n-1)\phi), \quad (2.69)$$

$$\Phi(\phi) = \sum_{n=1}^{\infty} Q_{\kappa,n} \sin(2n\phi), \quad (2.70)$$

$$\mathcal{H}(\phi) = \sum_{n=1}^{\infty} H_{\kappa,n} (-1)^n [\cos(2n\phi) + \cos(2(n-1)\phi)], \quad (2.71)$$

where subscript κ on each coefficient denotes the longitudinal wave number that we are currently using as defined in equations (2.63)–(2.65).

It is also essential to point out that the particular form of (2.71) is due to the process of basis recombination in which we have constructed new basis functions, which are linear combinations of our underlying basis set, that satisfy the required boundary conditions, as discussed in detail in Boyd[10, page 112]. Basis recombination is needed here since the general representation of $h(\eta, \phi)$ need only be constant at the poles, rather than zero as in the case of the two velocity components u_λ and u_ϕ . Thus the underlying basis set is centered around $\cos(2n\phi)$ which attains the value of ± 1 at the poles. Since we require $\mathcal{H}(\phi)$ to be zero at $\pm\pi/2$ then it becomes the task of basis recombination to satisfy this boundary condition; this is achieved through the particular form of (2.71).

2.5.2 Galerkin Method

With the forms for each of our series defined we now tackle the problem of solving for the wavespeed c and associated coefficients $P_{\kappa,n}$, $Q_{\kappa,n}$ and $H_{\kappa,n}$. To do this we exploit the orthogonality properties of the trigonometric functions by requiring that the residual equations, obtained after substituting (2.69)–(2.71) into (2.66)–(2.68), be orthogonal to each of our expansion functions. This technique amounts to the standard Galerkin method which has been used extensively to solve optimization and root finding problems from all areas of mathematics. We now demonstrate the particular application to our problem.

Substitution of (2.69)–(2.71) into (2.66) yields the algebraic version of the linearized

mass equation given by

$$\begin{aligned}
& -\kappa(\omega - \text{Sr } c) \sum_{n=1}^{\infty} H_{\kappa,n} (-1)^n [\cos(2n\phi) \cos \phi + \cos(2(n-1)\phi) \cos \phi] \\
& - \omega \text{Fr}^2 \left(\frac{1}{\text{Ro}} + \omega \right) \sum_{n=1}^{\infty} Q_{\kappa,n} \sin(2n\phi) \cos^2 \phi \sin \phi \\
& + (h_o + \frac{\omega \text{Fr}^2}{2} \left(\frac{1}{\text{Ro}} + \omega \right) \cos^2 \phi) \left[-\kappa \sum_{n=1}^{\infty} P_{\kappa,n} \cos((2n-1)\phi) \right. \\
& \left. + \sum_{n=1}^{\infty} Q_{\kappa,n} 2n \cos(2n\phi) \cos \phi - \sum_{n=1}^{\infty} Q_{\kappa,n} \sin(2n\phi) \sin \phi \right] = 0. \quad (2.72)
\end{aligned}$$

We can show that general terms of (2.72) take the form $\cos((2l-1)\phi)$, for $l = 0, 1, 2, \dots$, so these become our base expansion functions and the orthogonality condition is now equivalent to multiplying (2.72) by $\cos((2l-1)\phi)$, integrating from $-\pi/2 \leq \phi \leq \pi/2$ and equating to zero. Performing these operations we have

$$\begin{aligned}
& -\kappa(\omega - \text{Sr } c) \sum_{n=1}^{\infty} H_{\kappa,n} (-1)^n \int_{-\pi/2}^{\pi/2} \cos(2n\phi) \cos \phi \cos((2l-1)\phi) d\phi \\
& + \kappa(\omega - \text{Sr } c) \sum_{n=1}^{\infty} H_{\kappa,n} (-1)^n \int_{-\pi/2}^{\pi/2} \cos(2(n-1)\phi) \cos \phi \cos((2l-1)\phi) d\phi \\
& - \omega \text{Fr}^2 \left(\frac{1}{\text{Ro}} + \omega \right) \sum_{n=1}^{\infty} Q_{\kappa,n} \int_{-\pi/2}^{\pi/2} \sin(2n\phi) \cos^2 \phi \sin \phi \cos((2l-1)\phi) d\phi \\
& - h_o \kappa \sum_{n=1}^{\infty} P_{\kappa,n} \int_{-\pi/2}^{\pi/2} \cos((2n-1)\phi) \cos((2l-1)\phi) d\phi \\
& + 2h_o \sum_{n=1}^{\infty} n Q_{\kappa,n} \int_{-\pi/2}^{\pi/2} \cos(2n\phi) \cos \phi \cos((2l-1)\phi) d\phi \\
& - h_o \sum_{n=1}^{\infty} Q_{\kappa,n} \int_{-\pi/2}^{\pi/2} \sin(2n\phi) \sin \phi \cos((2l-1)\phi) d\phi \\
& - \frac{\kappa \omega \text{Fr}^2}{2} \left(\frac{1}{\text{Ro}} + \omega \right) \sum_{n=1}^{\infty} P_{\kappa,n} \int_{-\pi/2}^{\pi/2} \cos((2n-1)\phi) \cos^2 \phi \cos((2l-1)\phi) d\phi \\
& + \omega \text{Fr}^2 \left(\frac{1}{\text{Ro}} + \omega \right) \sum_{n=1}^{\infty} n Q_{\kappa,n} \int_{-\pi/2}^{\pi/2} \cos(2n\phi) \cos^3 \phi \cos((2l-1)\phi) d\phi \\
& - \frac{\omega \text{Fr}^2}{2} \left(\frac{1}{\text{Ro}} + \omega \right) \sum_{n=1}^{\infty} Q_{\kappa,n} \int_{-\pi/2}^{\pi/2} \sin(2n\phi) \sin \phi \cos^2 \phi \cos((2l-1)\phi) d\phi = 0. \quad (2.73)
\end{aligned}$$

All of the integrals in (2.73) can be rewritten by using trigonometric identities to express the integrands in terms of products of two of the base expansion functions.

As an example, we consider the first integral in (2.73) and note that the integrand may be written, with the aid of the identity $\cos(A - B) + \cos(A + B) = 2 \cos A \cos B$, as

$$\begin{aligned} \cos(2n\phi) \cos \phi \cos((2l - 1)\phi) &= \frac{1}{2} [\cos((2n + 1)\phi) + \cos((2n - 1)\phi)] \cos((2l - 1)\phi) \\ &= \frac{1}{2} \cos((2n + 1)\phi) \cos((2l - 1)\phi) \\ &\quad + \frac{1}{2} \cos((2n - 1)\phi) \cos((2l - 1)\phi). \end{aligned} \quad (2.74)$$

In addition we then, if required, shift the index on the resulting integrands so that every integral in equation (2.73) is transformed to one of the form

$$I_o = \int_{-\frac{\pi}{2}}^{\frac{\pi}{2}} \cos((2n - 1)\phi) \cos((2l - 1)\phi) d\phi, \quad (2.75)$$

$$= \begin{cases} \frac{\pi}{2} & \text{if } n = l, (n = 0 \text{ and } l = 1) \text{ or } (n = 1 \text{ and } l = 0), \\ 0 & \text{otherwise,} \end{cases} \quad (2.76)$$

where the o subscript denotes an integral obtained by using orthogonality.

Applying trigonometric identities, similar to that used in (2.74), to all the integrals in (2.73) and then shifting the indices on those terms that require it we obtain

$$\begin{aligned} & -\frac{\kappa}{2}(\omega - \text{Sr } c) \sum_{n=0}^{\infty} H_{\kappa,n+1}(-1)^{n+1} I_o - \kappa(\omega - \text{Sr } c) \sum_{n=1}^{\infty} H_{\kappa,n}(-1)^n I_o \\ & - \frac{\kappa}{2}(\omega - \text{Sr } c) \sum_{n=2}^{\infty} H_{\kappa,n-1}(-1)^{n-1} I_o - \frac{\omega \text{Fr}^2}{8} \left(\frac{1}{\text{Ro}} + \omega \right) \left[\sum_{n=0}^{\infty} Q_{\kappa,n+1} I_o \right. \\ & \quad \left. + \sum_{n=1}^{\infty} Q_{\kappa,n} I_o - \sum_{n=2}^{\infty} Q_{\kappa,n-1} I_o - \sum_{n=3}^{\infty} Q_{\kappa,n-2} I_o \right] - h_o \kappa \sum_{n=1}^{\infty} P_{\kappa,n} I_o \\ & + h_o \sum_{n=1}^{\infty} n Q_{\kappa,n} I_o + h_o \sum_{n=2}^{\infty} (n - 1) Q_{\kappa,n-1} I_o - \frac{h_o}{2} \sum_{n=1}^{\infty} Q_{\kappa,n} I_o + \frac{h_o}{2} \sum_{n=2}^{\infty} Q_{\kappa,n-1} I_o \\ & - \frac{\kappa \omega \text{Fr}^2}{8} \left(\frac{1}{\text{Ro}} + \omega \right) \left[\sum_{n=0}^{\infty} P_{\kappa,n+1} I_o + 2 \sum_{n=1}^{\infty} P_{\kappa,n} I_o + \sum_{n=2}^{\infty} P_{\kappa,n-1} I_o \right] \\ & - \frac{\omega \text{Fr}^2}{16} \left(\frac{1}{\text{Ro}} + \omega \right) \left[\sum_{n=0}^{\infty} Q_{\kappa,n+1} I_o + \sum_{n=1}^{\infty} Q_{\kappa,n} I_o - \sum_{n=2}^{\infty} Q_{\kappa,n-1} I_o - \sum_{n=3}^{\infty} Q_{\kappa,n-2} I_o \right] \\ & + \frac{\omega \text{Fr}^2}{8} \left(\frac{1}{\text{Ro}} + \omega \right) \left[\sum_{n=0}^{\infty} (n + 1) Q_{\kappa,n+1} I_o + 3 \sum_{n=1}^{\infty} n Q_{\kappa,n} I_o \right. \\ & \quad \left. + 3 \sum_{n=2}^{\infty} (n - 1) Q_{\kappa,n-1} I_o + \sum_{n=3}^{\infty} (n - 2) Q_{\kappa,n-2} I_o \right] = 0. \end{aligned} \quad (2.77)$$

Each integral I_o in (2.77) is now in the standard form given by (2.75) allowing us to use the orthogonality conditions given in (2.76) to extract a set of algebraic equations for each value of the integer l . Letting $l = 1$ and performing some algebraic manipulations we arrive at

$$\begin{aligned} & \left[-\kappa h_o - \frac{3\kappa\omega\text{Fr}^2}{8} \left(\frac{1}{\text{Ro}} + \omega \right) \right] P_{\kappa,1} - \frac{\kappa\omega\text{Fr}^2}{8} \left(\frac{1}{\text{Ro}} + \omega \right) P_{\kappa,2} \\ & + \left[\frac{h_o}{2} + \frac{\omega\text{Fr}^2}{8} \left(\frac{1}{\text{Ro}} + \omega \right) \right] Q_{\kappa,1} + \frac{\omega\text{Fr}^2}{16} \left(\frac{1}{\text{Ro}} + \omega \right) Q_{\kappa,2} \\ & + \frac{3\kappa\omega}{2} H_{\kappa,1} - \frac{\kappa\omega}{2} H_{\kappa,2} = c \left[\frac{3\kappa\text{Sr}}{2} H_{\kappa,1} - \frac{\kappa\text{Sr}}{2} H_{\kappa,2} \right], \end{aligned} \quad (2.78)$$

where we have taken the terms involving the wavespeed c to the right hand side in preparation for the numerical solution method, to be discussed shortly. We also note that letting $l = 1$ is equivalent to letting $l = 0$ since the nature of the orthogonality of $\cos((2n-1)\phi) \cos((2l-1)\phi)$ is the same in both cases.

In a similar vein we now consider the case when $l = 2$, leading to

$$\begin{aligned} & -\frac{\kappa\omega\text{Fr}^2}{8} \left(\frac{1}{\text{Ro}} + \omega \right) P_{\kappa,1} + \left[-\kappa h_o - \frac{\kappa\omega\text{Fr}^2}{4} \left(\frac{1}{\text{Ro}} + \omega \right) \right] P_{\kappa,2} \\ & - \frac{\kappa\omega\text{Fr}^2}{8} \left(\frac{1}{\text{Ro}} + \omega \right) P_{\kappa,3} + \left[\frac{3h_o}{2} + \frac{9\omega\text{Fr}^2}{16} \left(\frac{1}{\text{Ro}} + \omega \right) \right] Q_{\kappa,1} \\ & + \left[\frac{3h_o}{2} + \frac{9\omega\text{Fr}^2}{16} \left(\frac{1}{\text{Ro}} + \omega \right) \right] Q_{\kappa,2} + \frac{3\omega\text{Fr}^2}{16} \left(\frac{1}{\text{Ro}} + \omega \right) Q_{\kappa,3} \\ & + \frac{\kappa\omega}{2} H_{\kappa,1} - \kappa\omega H_{\kappa,2} + \frac{\kappa\omega}{2} H_{\kappa,3} = c \left[\frac{\kappa\text{Sr}}{2} H_{\kappa,1} - \kappa\text{Sr} H_{\kappa,2} + \frac{\kappa\text{Sr}}{2} H_{\kappa,3} \right]. \end{aligned} \quad (2.79)$$

Finally, the cases for $l \geq 3$ are given by

$$\begin{aligned} & -\frac{\kappa\omega\text{Fr}^2}{8} \left(\frac{1}{\text{Ro}} + \omega \right) P_{\kappa,l-1} + \left[-\kappa h_o - \frac{\kappa\omega\text{Fr}^2}{4} \left(\frac{1}{\text{Ro}} + \omega \right) \right] P_{\kappa,l} \\ & - \frac{\kappa\omega\text{Fr}^2}{8} \left(\frac{1}{\text{Ro}} + \omega \right) P_{\kappa,l+1} + \frac{\omega(2l-1)\text{Fr}^2}{16} \left(\frac{1}{\text{Ro}} + \omega \right) Q_{\kappa,l-2} \\ & + \left[\frac{(2l-1)h_o}{2} + \frac{3(2l-1)\omega\text{Fr}^2}{16} \left(\frac{1}{\text{Ro}} + \omega \right) \right] Q_{\kappa,l-1} \\ & + \left[\frac{(2l-1)h_o}{2} + \frac{3(2l-1)\omega\text{Fr}^2}{16} \left(\frac{1}{\text{Ro}} + \omega \right) \right] Q_{\kappa,l} \\ & + \frac{\omega(2l-1)\text{Fr}^2}{16} \left(\frac{1}{\text{Ro}} + \omega \right) Q_{\kappa,l+1} + \frac{\kappa\omega(-1)^l}{2} H_{\kappa,l-1} - \kappa\omega(-1)^l H_{\kappa,l} \\ & + \frac{\kappa\omega(-1)^l}{2} H_{\kappa,l+1} = c \left[\frac{\kappa\text{Sr}(-1)^l}{2} H_{\kappa,l-1} - \kappa\text{Sr}(-1)^l H_{\kappa,l} + \frac{\kappa\text{Sr}(-1)^l}{2} H_{\kappa,l+1} \right]. \end{aligned} \quad (2.80)$$

Equations (2.78), (2.79) and (2.80) constitute an infinite set of algebraic relationships representing mass conservation that must be satisfied for a solution to be valid. In a similar manner we can derive equivalent algebraic relationships from both the λ and ϕ momentum equations, (2.67) and (2.68), by substituting our series expressions for the $O(\epsilon)$ field variables and using orthogonality to generate the required equations.

From the λ momentum equation we have: For $l = 0$,

$$-\frac{\kappa\omega}{2}P_{\kappa,1} - \frac{1}{4}\left(\frac{1}{\text{Ro}} + \omega\right)Q_{\kappa,1} + \frac{\kappa}{\text{Fr}^2}H_{\kappa,1} = c\left[-\frac{\kappa\text{Sr}}{2}P_{\kappa,1}\right], \quad (2.81)$$

for $l = 1$,

$$\begin{aligned} -\frac{\kappa\omega}{2}P_{\kappa,1} - \frac{\kappa\omega}{2}P_{\kappa,2} - \frac{1}{4}\left(\frac{1}{\text{Ro}} + \omega\right)Q_{\kappa,2} + \frac{\kappa}{\text{Fr}^2}H_{\kappa,1} - \frac{\kappa}{\text{Fr}^2}H_{\kappa,2} \\ = c\left[-\frac{\kappa\text{Sr}}{2}P_{\kappa,1} - \frac{\kappa\text{Sr}}{2}P_{\kappa,2}\right] \end{aligned} \quad (2.82)$$

and for $l \geq 2$,

$$\begin{aligned} -\frac{\kappa\omega}{2}P_{\kappa,l} - \frac{\kappa\omega}{2}P_{\kappa,l+1} + \frac{1}{4}\left(\frac{1}{\text{Ro}} + \omega\right)Q_{\kappa,l-1} - \frac{1}{4}\left(\frac{1}{\text{Ro}} + \omega\right)Q_{\kappa,l+1} \\ - \frac{\kappa(-1)^l}{\text{Fr}^2}H_{\kappa,l} + \frac{\kappa(-1)^l}{\text{Fr}^2}H_{\kappa,l+1} = c\left[-\frac{\kappa\text{Sr}}{2}P_{\kappa,l} - \frac{\kappa\text{Sr}}{2}P_{\kappa,l+1}\right]. \end{aligned} \quad (2.83)$$

Similarly from the ϕ momentum equation we have, for $l \geq 1$,

$$\begin{aligned} \frac{1}{2}\left(\frac{1}{\text{Ro}} + \omega\right)P_{\kappa,l} - \frac{1}{2}\left(\frac{1}{\text{Ro}} + \omega\right)P_{\kappa,l+1} + \kappa\omega Q_{\kappa,l} + \frac{2l(-1)^{l+1}}{\text{Fr}^2}H_{\kappa,l} \\ - \frac{2l(-1)^{l+1}}{\text{Fr}^2}H_{\kappa,l+1} = c[\kappa\text{Sr}Q_{\kappa,l}]. \end{aligned} \quad (2.84)$$

2.5.3 Truncation and Generalised Eigenvalue Formulation

The set of algebraic equations (2.78)–(2.84) represent an infinite linear system in the form of a generalised eigenvalue problem. In order to perform any numerical work it is essential to truncate this system to some finite size. Let $N \in \mathbb{N}$ define an integer truncation level so that our infinite series (2.69)–(2.71) are now truncated to sums over the finite domain $1 \leq n \leq N$ for $n \in \mathbb{N}$. Since we have three field variables to solve for we will have a total of $3N$ unknown coefficients, requiring $3N$ equations to close the system.

Our choice of equations from the set (2.78)–(2.84) is rather intuitive and obvious in that we use exactly N equations from each physical law. To elucidate this process we note that the orthogonalised version of the mass equation consists of two base equations, (2.78) and (2.79), and an infinite series of equations in the form of a recurrence relation (2.80). To obtain exactly N equations from this set we retain the first two equations along with $N-2$ from the recurrence relation so that the limit on l in (2.80) is now $l = 3, 4, 5, \dots, N$. Note that when $l = N$ we make reference to the coefficients $P_{\kappa, N+1}$, $Q_{\kappa, N+1}$ and $H_{\kappa, N+1}$ but these and higher-order coefficients are ignored in the truncation of the series (2.69)–(2.71). Thus when $l = N$ we have the modified version of (2.80) given by

$$\begin{aligned}
& -\frac{\kappa\omega\text{Fr}^2}{8}\left(\frac{1}{\text{Ro}} + \omega\right)P_{\kappa, N-1} + \left[-\kappa h_o - \frac{\kappa\omega\text{Fr}^2}{4}\left(\frac{1}{\text{Ro}} + \omega\right)\right]P_{\kappa, N} \\
& + \frac{\omega(2N-1)\text{Fr}^2}{16}\left(\frac{1}{\text{Ro}} + \omega\right)Q_{\kappa, N-2} \\
& + \left[\frac{(2N-1)h_o}{2} + \frac{3(2N-1)\omega\text{Fr}^2}{16}\left(\frac{1}{\text{Ro}} + \omega\right)\right]Q_{\kappa, N-1} \\
& + \left[\frac{(2N-1)h_o}{2} + \frac{3(2N-1)\omega\text{Fr}^2}{16}\left(\frac{1}{\text{Ro}} + \omega\right)\right]Q_{\kappa, N} \\
& + \frac{\kappa\omega(-1)^N}{2}H_{\kappa, N-1} - \kappa\omega(-1)^N H_{\kappa, N} \\
& = c \left[\frac{\kappa\text{Sr}(-1)^N}{2}H_{\kappa, N-1} - \kappa\text{Sr}(-1)^N H_{\kappa, N} \right]. \tag{2.85}
\end{aligned}$$

In a similar way we note that the orthogonalised version of the λ momentum equation also consists of two base equations, (2.81) and (2.82), and an infinite recurrence set (2.83). Again, to obtain exactly N equations from this set we retain the first two equations and $N-2$ equations from the recurrence relation so that the limit on l in (2.83) is $l = 2, 3, 4, \dots, N-1$. Since the maximum coefficient index is N , occuring when $l = N-1$, we only index into coefficients that are members of the truncated set so no special treatment, analogous to that used to obtain (2.85) above, is required in this case.

The orthogonalised version of the ϕ momentum equation consists of one infinite recurrence relation which we truncate to N equations by imposing the limit $l = 1, 2, 3, \dots, N$ on l in (2.84). When $l = N$ it is again necessary to ignore $P_{\kappa, N+1}$, $Q_{\kappa, N+1}$ and $H_{\kappa, N+1}$ and higher-order coefficients, giving a special form of (2.84) for

this case. The result is

$$\frac{1}{2} \left(\frac{1}{\text{Ro}} + \omega \right) P_{\kappa,N} + \kappa \omega Q_{\kappa,N} + \frac{2N(-1)^{N+1}}{\text{Fr}^2} H_{\kappa,N} = c [\kappa \text{Sr} Q_{\kappa,N}]. \quad (2.86)$$

The set of equations (2.78)–(2.84), coupled with the two special terminating conditions (2.85) and (2.86), constitute a complete generalised eigenvalue problem of the form

$$A\mathbf{x} = cB\mathbf{x},$$

where A and B are matrices corresponding to the left and right hand sides of each of our algebraic equations. The eigenvalue c is precisely the wavespeed for our progressive Rossby waves, and vector \mathbf{x} is the eigenvector of unknown linearized coefficients which we define as

$$\mathbf{x} = \begin{pmatrix} H_{\kappa,1} \\ \vdots \\ H_{\kappa,N} \\ P_{\kappa,1} \\ \vdots \\ P_{\kappa,N} \\ Q_{\kappa,1} \\ \vdots \\ Q_{\kappa,N} \end{pmatrix}. \quad (2.87)$$

We note that the general structure of both A and B is that of a banded diagonal matrix with A also containing banded sub and super diagonal components. In particular we note that diagonal matrix B consists of non-zero elements along the main diagonal and thus will be invertible, implying that we will always be able to find solutions of our generalised eigensystem.

2.6 Solution and Results

2.6.1 Parameters and Constants

Now that the linearized problem has been formulated, all that remains is to specify the particular values for the dimensionless parameters in the model and to solve the resulting system. Although this analysis is not specific to a given sphere size or mass it seems reasonable to use parameters that closely approximate those of the Earth so that direct comparison can be made between the present model and other

published results. With this in mind we adopt the following values for the sphere specific parameters:

$$a = 6.37122 \times 10^6 \text{m}, \quad (2.88)$$

$$\Omega = \frac{2\pi}{24 \times 3600} \approx 7.272 \times 10^{-5} \text{s}^{-1}, \quad (2.89)$$

$$g = 9.80616 \text{m s}^{-2}. \quad (2.90)$$

Additionally we define each characteristic reference scale as

$$v_{\text{ref}} = 40 \text{m s}^{-1}, \quad (2.91)$$

$$h_{\text{ref}} = 8.0 \times 10^3 \text{m}, \quad (2.92)$$

$$c_{\text{ref}} = \frac{\Omega}{30} \approx 2.4241 \times 10^{-6} \text{s}^{-1}. \quad (2.93)$$

Note that whilst the values for h_{ref} and c_{ref} seem “reasonable” with reference to the Earth, one should not be surprised at the rather large value of v_{ref} . Normally, to compute velocities similar to those observed locally on the surface of the Earth one must include the effects of friction and the planetary boundary layer in the problem. Neglecting these terms, as we have done in this analysis, will always result in higher than observed surface velocities, which accounts for the larger than normal choice of v_{ref} .

With the specification of the above parameters we can now calculate estimates for the Strouhal, Froude and Rossby numbers. These are given by

$$\text{Sr} = \frac{a c_{\text{ref}}}{v_{\text{ref}}} \approx 3.8611 \times 10^{-1}, \quad (2.94)$$

$$\text{Fr} = \frac{v_{\text{ref}}}{\sqrt{g h_{\text{ref}}}} \approx 1.4281 \times 10^{-1}, \quad (2.95)$$

$$\text{Ro} = \frac{v_{\text{ref}}}{2\Omega a} \approx 4.3166 \times 10^{-2}. \quad (2.96)$$

The small value of Ro is in agreement with the definition of large-scale flow defined by Pedlosky[65, pages 2–3] so that we can expect the Earth’s rotation to be an influential factor determining the nature of any calculated solution. This is precisely the kind of behaviour we seek since we require flows in which the dominant driving force sustaining any initial perturbation is highly dependent on the large scale nature of the flow, as first demonstrated by Rossby[69].

For the dimensionless zonal flow parameters we choose values that are consistent with those documented in the test set of Williamson et al.[87]. The equivalent

non-dimensional values for h_o and ω are

$$h_o = 1, \quad (2.97)$$

$$\omega \approx 1.25. \quad (2.98)$$

The value of 1 for h_o is consistent with our previous statement about the dimensional value of h at $\phi = \pm\pi/2$ being h_{ref} , and the particular value of ω above is obtained by noting that Williamson et al. use a dimensional value for ω of $7.848 \times 10^{-6} \text{ s}^{-1}$, a value first introduced by Phillips[66] in 1956 when he successfully integrated the primitive equations of atmospheric flow. In order to convert this to a dimensionless number it is necessary to multiply by the radius of the Earth and divide by the reference velocity scale so that

$$\omega = \frac{7.848 \times 10^{-6} a}{v_{\text{ref}}} \approx 1.25. \quad (2.99)$$

Although (2.99) is only a single value of the dimensionless zonal flow angular speed, the analysis presented here permits a wide variety of values for ω . Nevertheless, the value given by (2.99) facilitates comparison with other published literature, such as Williamson et al. [87]. In the next section we will consider the solution for values of ω over a wide range of allowable values including the specific value above, anticipating the strong dependence of the nonlinear solution on ω which will be discussed in Chapter 3.

2.6.2 Results for $\kappa = 3, 4$ and 5

The solution of the generalised eigenvalue problem was achieved by implementing a MATLAB script that assembled the left and right hand side matrices and then solved the resulting system by using the inbuilt routine `eig(A,B)` to find the eigenvalues and corresponding eigenvectors. Various truncation levels were chosen to check convergence of the algorithm and in all cases rapid convergence was observed for increasing N . Typically a truncation value of $N = 10$ was all that was required to establish the solution to 4 or 5 significant figures and a truncation level of $N = 100$ could almost be deemed excessive if not for the very small computational times involved; approximately 3 seconds was required to compute all 300 eigenvalue-eigenvector pairs when $N = 100$, on an AMD Athlon(tm) XP 1800+ processor clocked at 1.54 GHz with 512 MB of physical memory clocked at 266 MHz.

Tables 2.1, 2.2 and 2.3 illustrate this rapid convergence for $\kappa = 3, 4$ and 5 respectively. The final column in each table gives the order of the last coefficient in each

N	3	5	10	100	$O(\text{Coeff}_{100})$
$H_{3,1}$	-4.6628E-02	-4.4294E-02	-4.4505E-02	-4.4507E-02	1.0E-09
$H_{3,2}$	-2.4242E-02	-2.2917E-02	-2.3022E-02	-2.3023E-02	
$H_{3,3}$	9.3363E-03	1.1141E-02	1.1256E-02	1.1258E-02	
$P_{3,1}$	-1.7968E-01	-1.7071E-01	-1.7152E-01	-1.7153E-01	1.0E-06
$P_{3,2}$	-6.5140E-01	-6.1965E-01	-6.2262E-01	-6.2265E-01	
$P_{3,3}$	-2.1733E-01	-1.7497E-01	-1.7495E-01	-1.7494E-01	
$Q_{3,1}$	-1.0157E+00	-9.6486E-01	-9.6945E-01	-9.6948E-01	1.0E-07
$Q_{3,2}$	-2.6718E-01	-2.5611E-01	-2.5740E-01	-2.5741E-01	
$Q_{3,3}$	1.1171E-02	5.1071E-02	5.2422E-02	5.2437E-02	
c	-4.1957E-02	-4.1805E-02	-4.1805E-02	-4.1805E-02	-

Table 2.1: Convergence of incompressible wavespeed and first three coefficients in each series for increasing N , $\kappa = 3$.

series when $N = 100$ and provides evidence for the accuracy of the solution since in each case the coefficients are observed to drop off reasonably fast and in the case of $\kappa = 4$ we have accuracy to very high precision. The particular scaling for the coefficients is arbitrary and has been chosen to match the equivalent Rossby-Haurwitz wave as specified in [87], to be explained in the next section. Note also that convergence of the eigenvalue is obtained with smaller truncation than that required for corresponding accuracy in the coefficients, providing confidence in the accuracy of the wavespeeds calculated.

N	3	5	10	100	$O(\text{Coeff}_{100})$
$H_{4,1}$	-3.0905E-02	-2.9884E-02	-2.9888E-02	-2.9888E-02	1.0E-17
$H_{4,2}$	-1.2042E-02	-1.1779E-02	-1.1781E-02	-1.1781E-02	
$H_{4,3}$	1.1248E-02	1.1718E-02	1.1719E-02	1.1719E-02	
$P_{4,1}$	-1.0749E-01	-1.0392E-01	-1.0393E-01	-1.0393E-01	1.0E-15
$P_{4,2}$	-5.0323E-01	-4.8531E-01	-4.8537E-01	-4.8537E-01	
$P_{4,3}$	-2.5965E-01	-2.3376E-01	-2.3379E-01	-2.3379E-01	
$Q_{4,1}$	-9.1506E-01	-8.8487E-01	-8.8498E-01	-8.8498E-01	1.0E-15
$Q_{4,2}$	-4.0863E-01	-3.9154E-01	-3.9158E-01	-3.9158E-01	
$Q_{4,3}$	6.5631E-03	3.0816E-02	3.0825E-02	3.0825E-02	
c	9.5282E-01	9.5522E-01	9.5522E-01	9.5522E-01	-

Table 2.2: Convergence of incompressible wavespeed and first three coefficients in each series for increasing N , $\kappa = 4$.

As already stated, we need not only consider the value of ω as used by Williamson

N	3	5	10	100	$O(\text{Coeff}_{100})$
$H_{5,1}$	-2.1197E-02	-2.1753E-02	-2.1665E-02	-2.1665E-02	1.0E-12
$H_{5,2}$	-6.2402E-03	-6.2807E-03	-6.2548E-03	-6.2548E-03	
$H_{5,3}$	1.0452E-02	1.0325E-02	1.0284E-02	1.0284E-02	
$P_{5,1}$	-6.8086E-02	-6.9875E-02	-6.9590E-02	-6.9590E-02	1.0E-10
$P_{5,2}$	-3.7993E-01	-3.9110E-01	-3.8951E-01	-3.8951E-01	
$P_{5,3}$	-2.3940E-01	-2.5611E-01	-2.5506E-01	-2.5506E-01	
$Q_{5,1}$	-7.9287E-01	-8.1367E-01	-8.1037E-01	-8.1036E-01	1.0E-10
$Q_{5,2}$	-4.5979E-01	-4.7615E-01	-4.7422E-01	-4.7422E-01	
$Q_{5,3}$	-8.0105E-04	-1.7789E-02	-1.7677E-02	-1.7677E-02	
c	1.5811E+00	1.5791E+00	1.5791E+00	1.5791E+00	-

Table 2.3: Convergence of incompressible wavespeed and first three coefficients in each series for increasing N , $\kappa = 5$.

et al. Indeed it is important to investigate the behaviour of the solution over a wide range of valid ω values. We now define precisely what we mean by “valid”. It was noted in Section 2.4.1 that, to make comparison between solutions with different values of ω it is essential to make sure that the volume^{iv} of fluid between the surface of the sphere and the free-surface is the same in each case. Since the linearized waves are effectively perturbations of the zonal flow, we need only match the volumes for each underlying zonal flow state because in the limit as $\epsilon \rightarrow 0$ the flow will reduce to this form.

To perform this analysis then, we need to agree on a volume that will remain constant throughout all the calculations. For now, let this volume be denoted by V_b where the subscript b represents the base volume. V_b can be any positive volume we decide upon as long as it remains small compared to the volume of the sphere so that the shallow atmosphere approximation is not violated. Generally one would choose V_b to be the volume of the atmosphere without any super rotation so that the free-surface has uniform height 1 everywhere and the volume is just given by the region bounded inside the two concentric spheres of radii \hat{a} and $\hat{a} + 1$, so that

$$V_b = \frac{4\pi}{3} + 4\pi\hat{a}(1 + \hat{a}).$$

Here we have denoted the dimensionless form of the sphere’s radius by \hat{a} , which is just the dimensional value divided by the reference height of the free-surface.

With a base volume decided upon we now ask the question; if the value of ω changes

^{iv}In general we need to consider the total mass of the fluid; however the incompressibility condition means that volume conservation is equivalent to mass conservation in this case

how must the value of h_o change to ensure that the volume remains constant? To answer this question we note that for the general zonal flow described in (2.53), the volume is given by

$$\begin{aligned} V_z &= \int_0^{2\pi} \int_{-\pi/2}^{\pi/2} \int_{\hat{a}}^{\hat{a}+h_z(\phi)} r^2 \cos \phi \, dr \, d\phi \, d\eta \\ &= \frac{4\pi}{3} \int_0^{\pi/2} [h_z^3 + 3h_z\hat{a}(h_z + \hat{a})] \cos \phi \, d\phi. \end{aligned} \quad (2.100)$$

The volume matching condition states that $V_z - V_b = 0$, thus substituting (2.53) into (2.100) and performing algebraic manipulations leads to a cubic equation for h_o of the form

$$\begin{aligned} \frac{4\pi}{3} h_o^3 + \left(\frac{8\pi A}{3} + 4\pi \hat{a} \right) h_o^2 + \left(\frac{32\pi A^2}{15} + \frac{16\pi \hat{a} A}{3} + 4\pi \hat{a}^2 \right) h_o \\ + \left(\frac{64\pi A^3}{105} + \frac{32\pi \hat{a} A^2}{15} + \frac{8\pi \hat{a}^2 A}{3} - V_b \right) = 0 \end{aligned} \quad (2.101)$$

where $A = \frac{\omega \text{Fr}^2}{2} \left(\frac{1}{\text{Ro}} + \omega \right)$. Once ω is fixed, which in turn fixes the coefficients in (2.101), we can solve for h_o using any appropriate method we choose, be it analytical or numerical. For the present purposes, the formula for the one real root of a cubic equation was used to solve for h_o , as taken from Abramowitz & Stegun[1].

In general we may choose any value for ω ; however for (2.101) to have non-negative solutions we can show that there is an upper limit on the value that ω can take, since the polar height h_o must decrease as the super-rotation rate increases, when volume remains fixed. The limiting upper value on ω , denoted ω_u , will be encountered once the solution of (2.101) returns $h_o = 0$. Similarly we can also argue for a lower limit of $\omega = 0$ since by definition of the linearization process we need to have a base zonal flow to perturb about, which can only occur for non-zero ω . In conclusion we must restrict our investigation to the valid range of values from $0 < \omega \leq \omega_u$.

With a volume matching method agreed upon we can now investigate the behaviour of the eigenvalues for constant volume and varying ω . For this analysis we present results only for the case $\kappa = 4$ since similar behaviour is observed when $\kappa = 3$ or 5 . For a given truncation N we will have a total of $3N$ eigenvalues computed. Figure 2.2 shows the 15 calculated eigenvalues when $N = 5$ for valid values of parameter ω . Although the truncation level is quite low here it is useful to observe what is

going on at this level since we can clearly distinguish between successive eigenvalues in the spectrum.

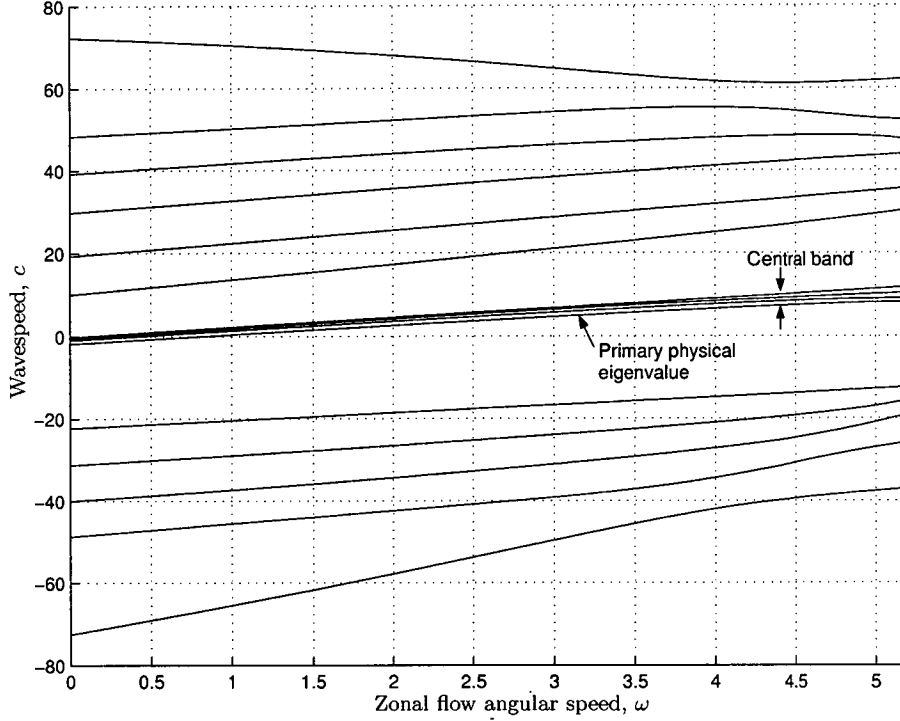


Figure 2.2: Full eigen-spectrum for $\kappa = 4$ with $N = 5$.

It is evident that solutions to this problem can be classified into two groups: Those in the indicated central band in Figure 2.2 and those lying outside this banded region. For the latter type, there was the initial suspicion that these were truncation induced solutions only; however further investigation at larger truncation levels revealed their persistence and convergence. The particular eigenvalues associated with these solutions are meaningless in a physical interpretation sense and thus can only be regarded as mathematically valid curiosities of the system. This is because the large values for the wavespeed that these solutions would imply are outside normally observed values on Earth. In addition the solutions themselves have an unphysical almost wave-less form with very little wave activity in the mid-latitudes and increased activity at the poles.

The central band, on the other hand, contains much more realistic and physically meaningful solutions that demand further investigation. As labelled in Figure 2.2, we regard the banded region as consisting of a primary physical eigenvalue and a

series of harmonics above this base state. The primary physical eigenvalue is so labelled since it is the main solution of the system and corresponds to Rossby waves in the sense of a well defined wave structure and wavespeed.

As the truncation level is increased it is observed that this central banded region becomes more heavily populated, with higher order solutions converging to an upper limit as indicated in Figure 2.3. While this behaviour is interesting in its own right, it is of little concern to us since the wavespeeds associated with such solutions are again rather too large to be considered as valid physical possibilities with reference to the Earth's atmosphere, where such speeds are never observed. We therefore restrict the rest of the discussion to an analysis of the primary physical eigenvalue and its main defining properties.

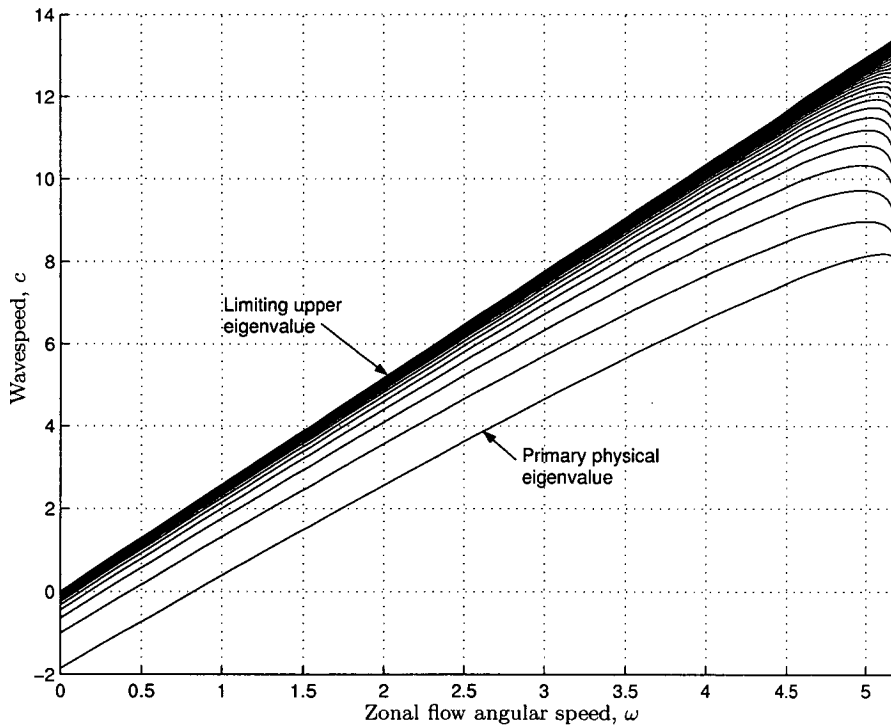


Figure 2.3: Zoomed eigen-spectrum for $\kappa = 4$ with $N = 50$.

There are three main points to be made concerning Figure 2.3. First and foremost we note that for values of ω away from the end points the wavespeed and ω relationship is close to linear. Secondly, there is a value of ω for which $c = 0$ so that the linearized Rossby wave structure remains stationary relative to the Earth's surface. For values of ω below this critical value we have wave motion towards the west

whereas for values higher we have eastward wave motion, allowing for a wide variety of atmospheric configurations. The final point concerns the behaviour at the upper end of the graph, in which no real confidence can be placed. The bending over of the solutions for large values of ω is a consequence of the fact that the height at the poles, h_o , is changing to conserve the total volume as previously discussed. At the other end of the graph, when $\omega = 0$, we observe that the linearized solution predicts that waves with non-zero wavespeed are possible when there is no zonal flow structure. One way to interpret this behaviour is through the idea that the perturbations themselves are valid solutions of the system and that no zonal flow is required for them to exist; this idea is expanded by Pedlosky [65, pages 108–110]. Nonetheless, the solutions associated with values of ω away from the end points are physically reasonable, relevant and consistent with the Rossby-Haurwitz solutions, to be discussed in the next section.

2.6.3 Comparison with Rossby-Haurwitz solution

To provide evidence supporting the accuracy of the linearized solutions computed, it is useful to make a comparison between these solutions and the equivalent corresponding Rossby-Haurwitz solutions. To do this we make use of the wavespeed formula as presented in Haurwitz's classic paper [32] and later adopted by Williamson et al. in their test set. The particular formula is given by

$$c = \frac{\kappa(3 + \kappa)\omega - 2\Omega}{(1 + \kappa)(2 + \kappa)} \quad (2.102)$$

which has been rewritten to reflect the naming conventions and variable names used in this work. Note that this equation clearly shows a linear relationship between c and ω . Also, Haurwitz's work does not allow one to fix the volume for the calculation, since it does not use a free-surface formulation, so we should expect some divergence from our solutions, which do take this into account.

To compare the two solution types we consider the primary physical eigenvalues for $\kappa = 3, 4$ and 5 with the equivalent Rossby-Haurwitz solutions over our valid ω range. Figure 2.4 shows the results of this comparison with the solid lines representing the equivalent Rossby-Haurwitz solution for $\kappa = 3$ to 5 from bottom to top respectively. In general one can conclude that the two models have good agreement, especially so for values of ω in the range $0 < \omega < 2$ where the effect of the volume matching is minimal. In fact better agreement is observed if one does not take the volume

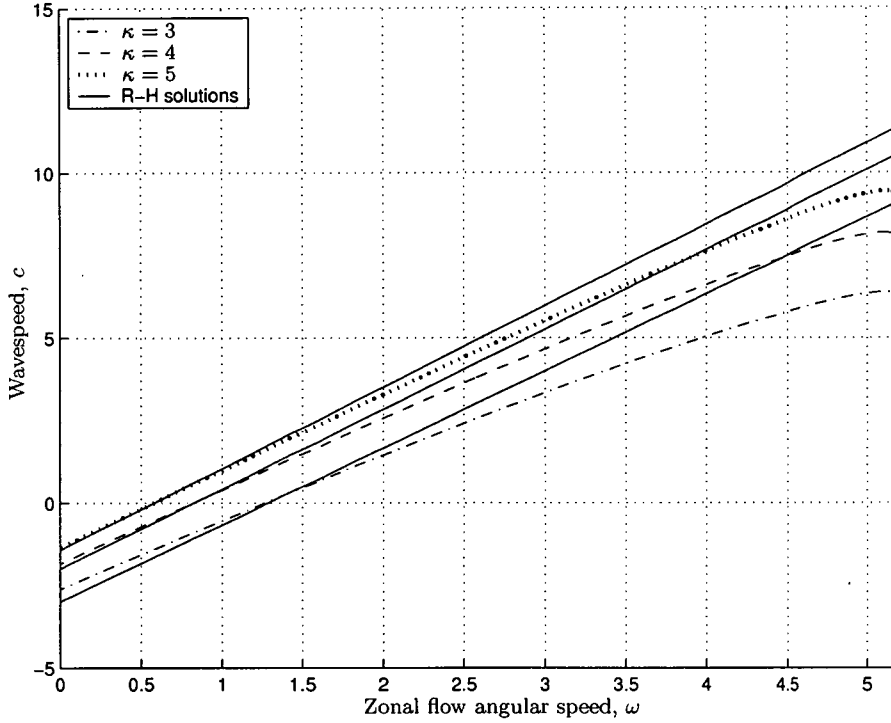


Figure 2.4: Comparison of incompressible linearized and Rossby-Haurwitz solutions for $\kappa = 3, 4$ and 5 with $N = 100$.

matching into consideration and fixes $h_o = 1$, however the validity of the comparison between various values of ω is questionable in this case.

It is also useful to examine the resulting free-surface contours produced by both models. In order to match the height contour levels it is necessary to specify some equivalent value of the wave amplitude ϵ . To make comparison possible we choose to match the two height fields at $(\eta, \phi) = (0, \pi/4)$ which represents a reasonable mid point level in each contour set. It is interesting to note that despite the fact that Haurwitz did not use a free-surface formulation, the resulting height field may be calculated via an analysis of the pressure field, as developed by Phillips[66].

Figures 2.5 and 2.6 provide a solution comparison both qualitatively, through a visual comparison, and quantitatively, through the specific contour levels of each height field. The latitudinal circle at $\phi = \pi/4$ is indicated to show where the match takes place. All plots were made using a polar stereographic projection of the Northern Hemisphere, described exhaustively in Snyder's monumental work[76]. Of particular interest is the slight pinching of crests and troughs for the Rossby-Haurwitz wave structure that is not evident in the linearized solution. This in

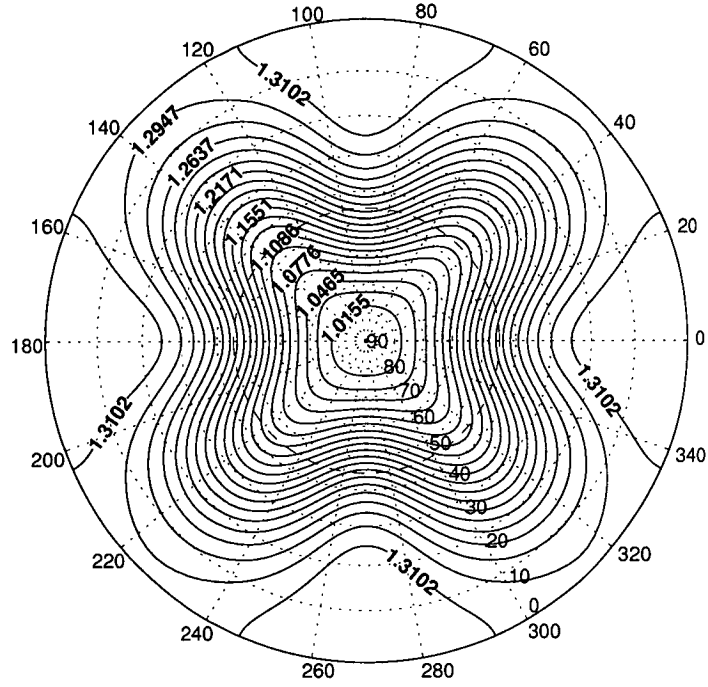


Figure 2.5: Incompressible shallow atmosphere free-surface contours for $\kappa = 4$ with $N = 100$.

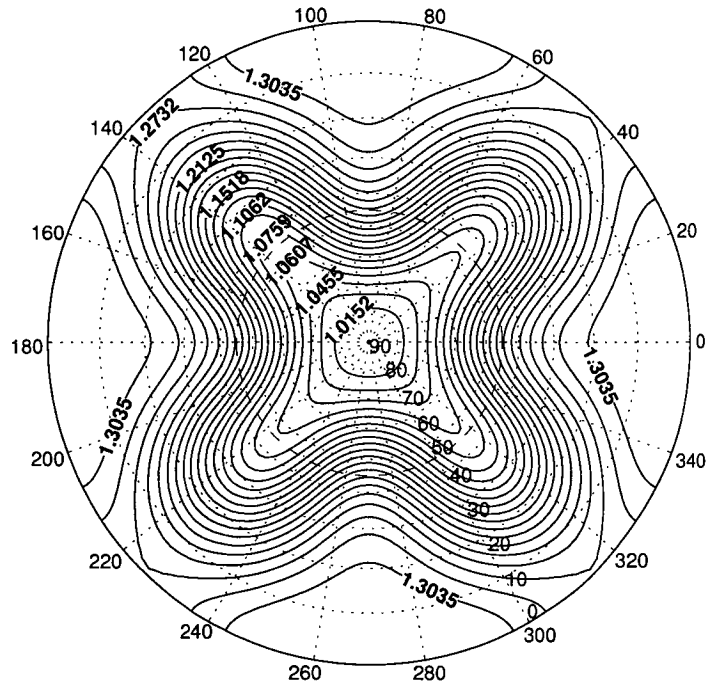


Figure 2.6: Rossby-Haurwitz free-surface contours for $\kappa = 4$.

turn forces the lower heights, and hence pressures, near the poles to extend further towards the equator in the Rossby–Haurwitz solution. However, overall there is very close agreement between both types of solutions, encouraging one to assume that these indeed are valid approximate solutions of the full non-linear governing equations.

As a final supporting statement we investigate the nature of the corresponding velocity vector field for the free-surface presented in Figure 2.5. From a geostrophic point of view we would expect the fluid streamlines to be nearly parallel to the pressure contours, something which is observed in Figure 2.7. Additionally we have increasingly diminishing flow as we approach either pole, which converges to the required stagnation point when $\phi = \pm\pi/2$. Since the particular viewpoint of the projection means that the sphere’s rotation is counter clockwise when viewed from above, we see that fluid flow is directed in the same direction as the underlying zonal flow with the Rossby wave pattern moving relative to this mean fluid progression.

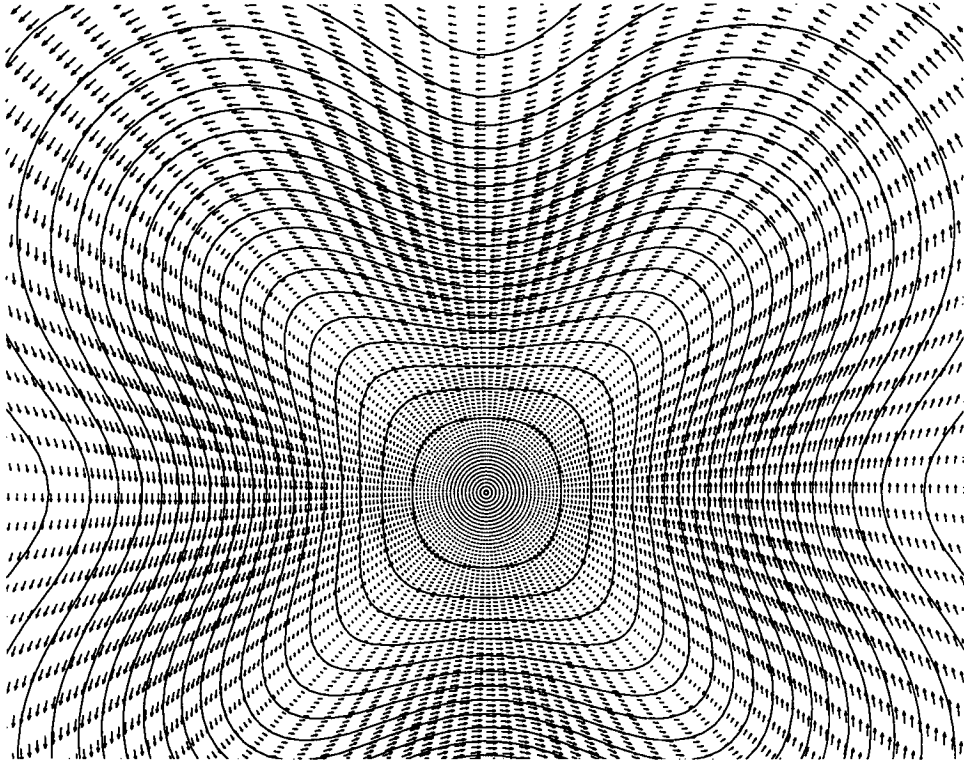


Figure 2.7: Incompressible shallow atmosphere free-surface contours with corresponding velocity vector field for $\kappa = 4$ with $N = 100$

In this chapter we have explored linearized solutions of the incompressible, non-

dimensional shallow atmosphere equations. The solutions that were obtained for particular values of longitudinal wave number κ were found to be in close agreement with the corresponding Rossby-Haurwitz solutions. Not only do the linearized solutions provide helpful insight into this complex dynamical system, they can also be used as a base starting point for a more thorough investigation of the complete nonlinear system. This problem is addressed in the next chapter.

CHAPTER 3

INCOMPRESSIBLE NONLINEAR SHALLOW ATMOSPHERE MODEL

The goal of this chapter is two fold: Firstly we wish to extend the linearized solutions computed in Chapter 2 to encompass the fully nonlinear equation set for the dynamical system. This will allow for the investigation of subtleties in the flow field, resulting from nonlinearity, which are not possible to expose using linear theory alone. Secondly, and perhaps more importantly, we aim to conduct an in-depth study of the relationship between the progressive wavespeed and corresponding amplitude. As will be shown, this type of analysis can reveal some interesting results concerning Rossby wave behaviour. It will be demonstrated that solutions of the system are highly dependent on the wavenumber κ and the zonal flow angular speed ω .

3.1 Problem Specification

3.1.1 Conservation Equations

The equations of motion to be used in the present chapter are those derived in the previous chapter for conservation of mass and momentum in the rotating shallow atmosphere system. For ease of reference and completeness we restate these equations ((2.43), (2.44) and (2.45)) here for later use. Readers may consult the first few sections of the previous chapter for their derivation. In dimensionless variables we have:

mass

$$(u_\lambda - \text{Sr } c \cos \phi) \frac{\partial h}{\partial \eta} + u_\phi \cos \phi \frac{\partial h}{\partial \phi} + h \left[\frac{\partial u_\lambda}{\partial \eta} + \cos \phi \frac{\partial u_\phi}{\partial \phi} - u_\phi \sin \phi \right] = 0, \quad (3.1)$$

λ momentum

$$(u_\lambda - \text{Sr } c \cos \phi) \frac{\partial u_\lambda}{\partial \eta} + u_\phi \cos \phi \frac{\partial u_\lambda}{\partial \phi} - \left(\frac{\cos \phi}{\text{Ro}} + u_\lambda \right) u_\phi \sin \phi + \frac{1}{\text{Fr}^2} \frac{\partial h}{\partial \eta} = 0, \quad (3.2)$$

ϕ momentum

$$(u_\lambda - \text{Sr } c \cos \phi) \frac{\partial u_\phi}{\partial \eta} + u_\phi \cos \phi \frac{\partial u_\phi}{\partial \phi} + \left(\frac{\cos \phi}{\text{Ro}} + u_\lambda \right) u_\lambda \sin \phi + \frac{\cos \phi}{\text{Fr}^2} \frac{\partial h}{\partial \phi} = 0. \quad (3.3)$$

The analytical solution of the above set of equations is extremely difficult, if not impossible, so we must turn to numerical approximation techniques to find solutions of the system. We will again employ the use of Fourier series but we must now use series with basis functions that span the entire solution range, rather than a restricted sub-domain as in the linearized solution approach.

3.1.2 Series Representation

In the previous chapter we were able to make use of the concept of a zonal flow and consider small perturbations about it. This approach allowed us to find small linearized corrections to the general flow field. In particular we showed that the two zonal flow parameters ω and h_o were enough to specify completely any zonal flow configuration. In the present chapter we still wish to use the concept of a zonal flow but we must now incorporate this into our series expansions as a fundamental component of the solution. Additionally, it is no longer possible to use the constant of integration h_o as a zonal flow parameter. This is because h_o effectively controls the free-surface height at the poles and in the nonlinear model we have no way of knowing what this height will be. Instead, the polar height becomes an output of the model and we must use some other technique for controlling the zonal flow state. We will address this issue shortly but first we define the particular forms for each series expansion.

Taking the symmetry and boundary conditions of Section 2.5.1 in Chapter 2 we now generalise the restricted series forms (2.69), (2.70) and (2.71) to encompass a wider range of solution. We can show that the series for the nonlinear problem that meet

our conditions are given by:

$$u_\lambda(\eta, \phi) = \omega \cos \phi + \sum_{m=1}^{\infty} \sum_{n=1}^{\infty} P_{m,n} \cos(\kappa m \eta) \cos((2n-1)\phi), \quad (3.4)$$

$$u_\phi(\eta, \phi) = \sum_{m=1}^{\infty} \sum_{n=1}^{\infty} Q_{m,n} \sin(\kappa m \eta) \sin(2n\phi), \quad (3.5)$$

$$\begin{aligned} h(\eta, \phi) = & \sum_{n=0}^{\infty} H_{0,n} \cos(2n\phi) \\ & + \sum_{m=1}^{\infty} \sum_{n=1}^{\infty} H_{m,n} \cos(\kappa m \eta) (-1)^n [\cos(2n\phi) + \cos(2(n-1)\phi)], \end{aligned} \quad (3.6)$$

where (3.6) uses basis recombination to satisfy boundary conditions at the poles and the series (3.4) for u_λ now contains the primary zonal flow velocity component. Instead of specifying the polar free-surface height we replace h_o with the η -independent series in (3.6) to allow for the polar height to be determined from the output of the model, as discussed previously.

It is interesting to point out the absence of any η -independent terms in the series (3.4) apart from the primary zonal flow term. One might well assume that to span the solution space with a complete basis set one should use a series for u_λ of the form

$$u_\lambda(\eta, \phi) = \omega \cos \phi + \sum_{n=1}^{\infty} P_{0,n} \cos((2n-1)\phi) + \sum_{m=1}^{\infty} \sum_{n=1}^{\infty} P_{m,n} \cos(\kappa m \eta) \cos((2n-1)\phi)$$

where we can think of the additional η -independent series term as modifying the base zonal flow in a way that only depends on latitude. The problem with this approach is that the zonal flow is no longer unique. Any numerical scheme that attempts to solve the equations using this series representation will fail since the zonal flow now becomes an output of the problem and the system has no way of knowing its own base state. In hindsight this conclusion seems rather obvious; however it was not discovered until analysis of the singular value decomposition of the Jacobian of the truncated system revealed exactly N machine precision sized singular values in the spectrum corresponding to the coefficients $P_{0,1}$ to $P_{0,N}$. Removal of these terms subsequently removed any associated ill-conditioning in the Jacobian, allowing the solution to be computed.

3.1.3 Volume Specification

To be able to make comparison between various solutions we need to fix the total mass of the system. The incompressibility of the problem implies that the density is constant throughout the fluid and hence we may regard conservation of mass as being equivalent to conservation of volume. To calculate the total volume of the fluid we integrate over the region contained between the surface of the sphere and the free-surface so that

$$\begin{aligned} V_{nl} &= \int_0^{2\pi} \int_{-\pi/2}^{\pi/2} \int_{\hat{a}}^{\hat{a}+h(\eta,\phi)} r^2 \cos \phi \, dr d\phi d\eta \\ &= \frac{4\kappa}{3} \int_0^{\pi/\kappa} \int_0^{\pi/2} [h^3 + 3\hat{a}^2 h + 3\hat{a} h^2] \cos \phi \, d\phi d\eta, \end{aligned} \quad (3.7)$$

where \hat{a} is the dimensionless form of the sphere's radius. Note also that we retain the wavenumber parameter κ from the previous chapter as a means of controlling the longitudinal wavelength and as a consequence we can restrict our integration to a smaller domain since the free-surface will have symmetry about the coordinate line $\eta = \pi/\kappa$.

To use the volume conservation condition effectively we need to decide upon a specific value for the volume, which we will denote V_z . Once this volume has been established we can construct an equation that reflects volume conservation by equating this volume with the volume obtained from (3.7). Thus we have the nonlinear equation for volume conservation given by

$$1 - \frac{V_{nl}}{V_z} = 0. \quad (3.8)$$

Equation (3.8) effectively replaces the specification of h_o to define an unique zonal flow structure. In the linearized problem an equivalent equation to (3.8) was not required since, for a fixed value of ω , the volume remained constant because the wavespeed did not vary with changes in the wave amplitude. In the nonlinear problem it is possible to have many different flow configurations for the same value of ω since the wavespeed now depends on the wave amplitude and thus the resulting volume will change as the Rossby wave amplitude changes. By using (3.8) we force the volume to remain constant for all computed solutions. If the amplitude is changing and the volume is constant it implies that the mean height of the fluid

must either increase or decrease. The mean height of the fluid is controlled via the polar free-surface height h_o . It is now apparent that we have in fact parametrised the polar height h_o in terms of the conservation condition expressed in (3.8), and this becomes the extra condition to close the problem.

3.2 Numerical Solution Method

3.2.1 Collocation

Equations (3.1), (3.2), (3.3) and (3.8) constitute a complete system for which the solution gives nonlinear Rossby waves. The solution process consists of finding the coefficients $H_{m,n}$, $P_{m,n}$, $Q_{m,n}$ and wavespeed c that make the series (3.4), (3.5) and (3.6) a solution of the system. Various different techniques for doing this are possible. The method chosen here is the pseudospectral technique of collocation in which we require the residuals, obtained by substituting the series into the governing equations, to be zero at every point on a mesh constructed from a finite number of points in the flow field. This technique is in contrast to the spectral Galerkin method of the previous chapter in which we required the residuals to be orthogonal to the basis expansion functions over the entire domain. While we can use the same basis functions for both the collocation and the Galerkin method, in the collocation method we no longer have the residual orthogonality property of spectral methods in general.

There are both advantages and disadvantages to using the collocation method over other techniques such as the Galerkin method or finite-difference schemes. Durran[20, pages 191–195] presents a detailed exposition of these key differences. In summary, the main advantage of collocation over a finite-difference scheme is that the collocation method will be more accurate provided the solution is smooth. This is a direct result of using infinitely differentiable basis functions which allow for the calculation of exact function derivatives at each point in the flow domain. The main advantage of collocation over the Galerkin method is that the collocation method is computationally less intensive because costly integrals need not be evaluated at each step. In addition, since the grid points are fixed for a particular mesh, we can cache the basis functions and their derivatives at all necessary points and use these stored values to speed up the solution process by eliminating costly function calls in the program. This technique will be explained later in the chapter.

The book by Boyd[10] provides an extensive analysis of spectral and pseudospectral methods, from which we summarise the basic process of the collocation method as follows. Suppose we have some functional operator given by

$$F[y(x)] = 0, \quad (3.9)$$

for independent variable x and dependent variable y . To solve this problem numerically we approximate $y(x)$ with a truncated series expansion of orthogonal basis functions, $\psi_n(x)$, so that

$$y(x) \approx y_N(x) = \sum_{n=0}^N a_n \psi_n(x). \quad (3.10)$$

Substituting (3.10) into (3.9) yields the equation

$$E[a_0, a_1, \dots, a_N, x] = F[y_N(x)] = 0. \quad (3.11)$$

We now choose $N + 1$ points, x_0, \dots, x_N , from the function domain and evaluate (3.11) at each of these discrete values to give

$$\mathbf{E}(\mathbf{a}) = \mathbf{0}, \quad (3.12)$$

where \mathbf{a} is the vector of unknown coefficients. In general (3.12) will not be satisfied for arbitrary \mathbf{a} and it now becomes the task to find the coefficients a_0, a_1, \dots, a_N that will simultaneously satisfy each individual component equation in (3.12).

The above algorithm outlines the essential elements of any collocation method. That is; find series coefficients that satisfy the residual equations exactly at a discrete number of points taken from the solution domain. A variety of methods can be employed to find the minimising set of coefficients; however it must be emphasized that this step is distinct from the general collocation method as a whole. In addition, the particular choice of grid points x_i is also an important stage in the solution process since certain choices of points are optimal in the sense of satisfying the equations at non-grid points. For our purposes the choice is easy since one can show that for Fourier basis functions the optimal choice is an evenly spaced mesh of grid points [10]. We now address the sub-task of finding the optimal set of coefficients a_n .

3.2.2 Newton–Raphson Technique

In general, the task of finding the vector of unknown coefficients \mathbf{a} that satisfies equation (3.12) is labelled a multi-dimensional root finding problem. Problems of

this type are notoriously difficult for a number of reasons, the main one being that zeros of one residual component generally have nothing in common with zeros of another distinct residual component, as described in Press et al.[68, pages 383–386]. However, it is possible to solve problems of this type with careful analysis and planning. One such method for accomplishing this task is an iterative technique called the Newton–Raphson algorithm.

We present here an overview of the Newton–Raphson algorithm as detailed in [68, pages 383–386]. Suppose we start with some initial guess for the vector of unknown coefficients, defined to be $\mathbf{a}^{(k)}$ where the superscript denotes the current iterative step. Each individual residual component in (3.12) can be expanded locally in a Taylor series about the multi-dimensional point $\mathbf{a}^{(k)}$, leading to the vector equation

$$\mathbf{E}(\mathbf{a}^{(k)} + \delta\mathbf{a}^{(k)}) = \mathbf{E}(\mathbf{a}^{(k)}) + \mathbf{J}^{(k)} \cdot \delta\mathbf{a}^{(k)} + O((\delta\mathbf{a}^{(k)})^2), \quad (3.13)$$

where $\mathbf{J}^{(k)}$ is the Jacobian matrix of partial derivatives and is defined by

$$J_{ij}^{(k)} = \left. \frac{\partial E_i}{\partial a_j} \right|_{\mathbf{a}^{(k)}}. \quad (3.14)$$

The goal of the root finding process is to make $\mathbf{E}(\mathbf{a}^{(k)} + \delta\mathbf{a}^{(k)}) = \mathbf{0}$; thus equation (3.13) provides a recipe for achieving this goal, since as a first approximation we can neglect the higher order terms and set $\mathbf{E}(\mathbf{a}^{(k)} + \delta\mathbf{a}^{(k)}) = \mathbf{0}$, enabling us to solve for the correction step $\delta\mathbf{a}^{(k)}$ that brings vector $\mathbf{a}^{(k)}$ closer to satisfying (3.12). The resulting linear system for the step direction is given by

$$\mathbf{J}^{(k)} \cdot \delta\mathbf{a}^{(k)} = -\mathbf{E}(\mathbf{a}^{(k)}), \quad (3.15)$$

which can be solved for the vector $\delta\mathbf{a}^{(k)}$ using standard linear algebra techniques. Once we have found the updating step, we update the solution to give the new vector

$$\mathbf{a}^{(k+1)} = \mathbf{a}^{(k)} + \delta\mathbf{a}^{(k)}, \quad (3.16)$$

which should be a better approximation to a root of (3.12). The above process is then repeated, starting from the new point $\mathbf{a}^{(k+1)}$, until convergence is achieved.

While this algorithm is useful it is by no means robust in the sense that it will always find a solution if one is known to exist. Specifically, the Newton–Raphson method is known to converge to a root only if the starting guess is sufficiently close to the root. Thus root finding using this technique requires both care and insight into the expected nature of the solution, as described by Acton [2].

One may improve the overall efficiency of the Newton–Raphson method by implementing a damping mechanism that tests if the calculated solution update at each stage of the algorithm actually does reduce each of the individual residual equations. Since the update vector $\delta \mathbf{a}^{(k)}$ will always be a descent direction, see [68], we can test the value of the residual at the new calculated point $\mathbf{a}^{(k+1)}$ and if $\|\mathbf{E}(\mathbf{a}^{(k+1)})\| > \|\mathbf{E}(\mathbf{a}^{(k)})\|$, for some appropriate norm, we reduce the magnitude of the step size by replacing $\delta \mathbf{a}^{(k)}$ with $\delta \mathbf{a}^{(k)}/2$ and retesting until we find a step magnitude that does reduce the residual. This technique is essentially the Newton–Raphson method with quasi line searches at the end of each iteration step.

The complete damped Newton–Raphson algorithm is represented in Table 3.1, where ϵ_1 and ϵ_2 are user-prescribed terminating error tolerances. In practice, one would normally use an L^1 or L^2 norm to represent the total residual error; in this study, the L^1 norm is employed. Additionally, step 3 of the algorithm must be monitored closely to check for spurious convergence since halving the step size multiple times will eventually satisfy the second terminating condition expressed in step 5. The simplest possible method to prevent this non-genuine convergence is to have an upper limit on the number of halvings allowed at each iterative level in the algorithm. If this limit is reached the algorithm is deemed to have failed for the specific initial guess in step 1, implying that either a root does not exist nearby or a new initial guess is required.

Damped Newton–Raphson Algorithmic Flow Chart

1. Define an initial guess, $\mathbf{a}^{(k)}$.
2. Solve the linear system, $\mathbf{J}^{(k)} \cdot \delta \mathbf{a}^{(k)} = -\mathbf{E}(\mathbf{a}^{(k)})$, for $\delta \mathbf{a}^{(k)}$.
3. While $\|\mathbf{E}(\mathbf{a}^{(k)} + \delta \mathbf{a}^{(k)})\| > \|\mathbf{E}(\mathbf{a}^{(k)})\|$, do $\delta \mathbf{a}^{(k)} = \delta \mathbf{a}^{(k)}/2$
4. Update the solution, $\mathbf{a}^{(k+1)} = \mathbf{a}^{(k)} + \delta \mathbf{a}^{(k)}$
5. If $\|\mathbf{E}(\mathbf{a}^{(k+1)})\| \leq \epsilon_1$ or $\|\delta \mathbf{a}^{(k)}\| \leq \epsilon_2$, EXIT
6. Increment k by 1 and repeat from step 2.

Table 3.1: Damped Newton–Raphson algorithm.

3.3 Code Highlights

In this section we present a brief overview of the key computer code components used to assemble and solve the nonlinear problem, as well as some specific details for particular techniques that were utilised.

3.3.1 Programming Language and Computational Environment

C++ was selected as the base programming language. In addition, various algorithms, with appropriate modifications, from “Numerical Recipes in C++” by Press et al.[68] were employed for common tasks, such as the solution of a linear system. The feature rich abilities of the C++ programming language were exploited where possible with much use being made of operator overloading to simplify and improve the readability of code. The Microsoft Visual C++ 6.0 and GNU C++ compilers were used for compilation on Microsoft Windows XP(tm) and Red Hat Linux 9.0(tm) respectively.

The majority of computations were performed on two separate computers, the first being an AMD Athlon(tm) XP 1800+ processor clocked at 1.54 GHz with 512 MB of physical memory clocked at 266 MHz, the second being an Athlon(tm) XP 2800+ processor clocked at 2.08 GHz with 1 GB of dual channel physical memory clocked at 333 MHz. Additionally, some computations were performed on an SGI Origin 3400 high performance computer (24 R14000 (500 MHz) CPUS, 24 GB main memory) using OpenMP, a programming interface for writing high performance parallel computations. Access to the super computer was generously provided by the Tasmanian Partnership for Advanced Computing (TPAC).

3.3.2 Truncation

To accomplish the task of numerically solving for the coefficients $H_{m,n}$, $P_{m,n}$, $Q_{m,n}$ and wavespeed c , we truncate the infinite series (3.4)–(3.6) with longitudinal trun-

cation M and latitudinal truncation N to give

$$u_\lambda(\eta, \phi) = \omega \cos \phi + \sum_{m=1}^M \sum_{n=1}^N P_{m,n} \cos(\kappa m \eta) \cos((2n-1)\phi), \quad (3.17)$$

$$u_\phi(\eta, \phi) = \sum_{m=1}^M \sum_{n=1}^N Q_{m,n} \sin(\kappa m \eta) \sin(2n\phi), \quad (3.18)$$

$$h(\eta, \phi) = \sum_{n=0}^N H_{0,n} \cos(2n\phi) + \sum_{m=1}^{M-1} \sum_{n=1}^N H_{m,n} \cos(\kappa m \eta) (-1)^n [\cos(2n\phi) + \cos(2(n-1)\phi)]. \quad (3.19)$$

Series (3.17)–(3.19), along with the unknown wavespeed c , contain a total of $3MN + 2$ unknown coefficients, so in order to close the system numerically we will need the same number of residual equations to use in the collocation method.

We have already noted that the problem is governed by three dynamical equations, (3.1)–(3.3), and a volume specification equation, (3.8). Since the volume specification equation contains an integral it is not possible to evaluate this at individual points in the domain. Rather, it represents the contribution from every point in the domain. Consequently we can just evaluate this equation once for a given coefficient set and append the result to our residual vector obtained from collocating at discrete points in the domain. This reduces the required number of collocation points to $3MN + 1$.

3.3.3 Forcing the Solution

It is necessary to be able to control the solution by stipulating either the wave amplitude, denoted \mathcal{A} , or the wavespeed, c , so that we may investigate the nonlinear dependence of the wavespeed on amplitude. In the linearized theory this dependence was not possible to expose because we only considered small amplitude waves. In the nonlinear theory the wavespeed will be a function of amplitude so that $c \equiv c(\mathcal{A})$. This behaviour has been demonstrated in a variety of situations, the most famous being Stokes' [78] classic paper on finite amplitude gravity waves which has spawned a plethora of additional papers (see the review article by Schwartz & Fenton [73]).

To force either the wavespeed or amplitude we must hold either of the two constant throughout each root finding process. It is most helpful to hold the amplitude constant and let the wavespeed be an output of the problem. To this end we need a

way of specifying the wave amplitude. This can be achieved by noting that we can parameterise \mathcal{A} in terms of one of our unknown coefficients. For example, we can hold $H_{1,1}$ fixed in the series for $h(\eta, \phi)$, thus removing one of the unknowns from the problem. With this method we have no way of knowing exactly what the relationship between \mathcal{A} and $H_{1,1}$ is, but it suffices to know that there *is* a relationship, through which we can force \mathcal{A} by specifying individual values for $H_{1,1}$.

By specifying either one of the coefficients or the wavespeed we again reduce by one the total number of unknowns in the problem so that we must now construct a total of $3MN$ residual equations. Since we have 3 separate dynamical equations that govern the system we need a total of MN collocation mesh points. We choose M points from the η domain and N points from the ϕ domain, to be discussed in the next section.

3.3.4 Collocation Points

For each orthogonal set of basis functions, there exists an optimal set of points chosen, from the function domain, which will yield an optimal collocation method. In general one can show that the optimal set of grid points consists of the abscissas of a Gaussian quadrature associated with the specific basis set [10, page 88]. For the trigonometric basis functions of a Fourier series, these points are evenly spaced throughout the entire periodic function domain and thus are easily calculated for any given truncation level.

For the collocation points in ϕ we restrict ourselves to the Northern hemisphere since our solution has specific symmetry relative to the equator. In addition we choose strictly internal points from the domain since we have imposed boundary conditions at both $\phi = 0$ and $\phi = \pm\pi/2$ through the specific choice of our basis functions. Defining

$$\Delta\phi = \frac{\pi}{2(N+1)} \quad (3.20)$$

to be the inter-grid point distance in the ϕ direction, the N equally-spaced ϕ -grid points are

$$\phi_i = i\Delta\phi, \quad \text{for } i = 1, 2, \dots, N. \quad (3.21)$$

The collocation points in η can be obtained in a similar manner; however, since we have stipulated a dependence on the wavenumber κ , we need to consider the effect this has on the linear independence of the individual residual equations. Specifically,

if parity exists in the basis functions, and this parity is reflected directly in the residual equations, then the collocation points must be modified to avoid redundancy in the residual vector [10, pages 159–171]. By incorporating the wavenumber κ into our series expansions we effectively force κ complete wavelengths around any given latitude circle. In addition each individual wavelength will have symmetry about its midpoint so that, for the first wavelengthⁱ, the symmetry line is $\eta = \pi/\kappa$. Consequently we must only choose collocation points from $\eta \in [0, \pi/\kappa)$ to avoid linearly dependent rows in the residual vector and resulting Jacobian matrix. Defining

$$\Delta\eta = \frac{\pi}{M\kappa} \quad (3.22)$$

to be the inter-grid point distance in the η direction, the M equally spaced η -grid points are

$$\eta_j = (j - 1)\Delta\eta, \quad \text{for } j = 1, 2, \dots, M. \quad (3.23)$$

The set of points taken from all possible (η_j, ϕ_i) pairs constitutes what is known as the collocation mesh. It is at precisely these points, and only these points, that we will zero the individual residual equations by finding the optimising wavespeed and associated set of coefficients.

3.3.5 Caching the Basis Functions

Unlike the spectral Galerkin method in which the residual values are considered at every point in the function domain, the pseudospectral collocation method only ever involves a finite number of points from the domain. We can use this to our advantage because generally the most computationally intensive part of any computer program is the evaluation of function calls. Since we know all the points at which we will need to evaluate our basis functions for given truncation levels, we can evaluate these just once and store the results in computer memory for later reference. The equations governing the dynamics contain not only the field variables but their derivatives with respect to η and ϕ as well, so we can also store this information in computer memory.

To illustrate this concept, consider the general basis function $\cos(\kappa m \eta)$ which appears in the u_λ and h series, (3.17) and (3.19), as well as in the η derivative of

ⁱIn the expression for η the $-ct$ term merely translates any initial wave configuration. We can therefore generalise by letting $t = 0$ so that effectively we have $\eta = \lambda$.

the u_ϕ series (3.18). For a given truncation level M the collocation points in η are defined uniquely by (3.23). We also know that the index m can take a value ranging from 1 to M . We can thus evaluate the general basis function for all possible m and η values and store this information in a matrix as

$$C_\eta = \begin{pmatrix} \cos(\kappa\eta_1) & \cdots & \cos(\kappa\eta_M) \\ \cos(2\kappa\eta_1) & \cdots & \cos(2\kappa\eta_M) \\ \vdots & & \vdots \\ \cos(M\kappa\eta_1) & \cdots & \cos(M\kappa\eta_M) \end{pmatrix}. \quad (3.24)$$

Similar matrices can be constructed and stored in computer memory for all the other general basis functions contained in the series expansions, allowing for rapid array access.

3.3.6 Calculation of the Jacobian Matrix

The root finding process outlined in Section 3.2.2 requires the computation of the Jacobian matrix of the residual vector at each iterative step. There are two main methods usually employed to calculate the Jacobian matrix. The first method involves the use of finite difference approximations to the derivatives of each residual component relative to each member of the vector composed of the unknown coefficients and wavespeed. The second method employs the analytical evaluation of the Jacobian terms prior to the computation stage, resulting in a simple evaluation for each element of the Jacobian. The second method is to be preferred to the first when the Jacobian elements are easily calculated because the resulting evaluations will be accurate to machine precision. In this study the analytical method is employed since the Jacobian elements are, in general, easily determined.

As an example we consider the evaluation of the derivative of the mass equation, (3.1), with respect to each of our unknown coefficient elements. For the sake of brevity we represent the mass equation at a particular collocation point as $f_1(\mathbf{a}) = 0$. Let a_i be a general element of the vector of unknowns \mathbf{a} and define the function ψ to be a generic placeholder for each of the dependent field variables u_λ , u_ϕ , h and the wavespeed c . We can represent the derivative of f_1 with respect to each element of \mathbf{a} as

$$\frac{\partial f_1}{\partial a_i} = \frac{\partial f_1}{\partial \psi} \frac{\partial \psi}{\partial a_i} + \frac{\partial f_1}{\partial \left(\frac{\partial \psi}{\partial \eta}\right)} \frac{\partial \left(\frac{\partial \psi}{\partial \eta}\right)}{\partial a_i} + \frac{\partial f_1}{\partial \left(\frac{\partial \psi}{\partial \phi}\right)} \frac{\partial \left(\frac{\partial \psi}{\partial \phi}\right)}{\partial a_i}. \quad (3.25)$$

Using this procedure we can show that the individual Jacobian components for the mass equation are

$$\frac{\partial f_1}{\partial P_{i,j}} = \frac{\partial h}{\partial \eta} \frac{\partial u_\lambda}{\partial P_{i,j}} + h \frac{\partial \left(\frac{\partial u_\lambda}{\partial \eta} \right)}{\partial P_{i,j}}, \quad (3.26)$$

$$\frac{\partial f_1}{\partial Q_{i,j}} = \left(\cos \phi \frac{\partial h}{\partial \phi} - h \sin \phi \right) \frac{\partial u_\phi}{\partial Q_{i,j}} + h \cos \phi \frac{\partial \left(\frac{\partial u_\phi}{\partial \phi} \right)}{\partial Q_{i,j}}, \quad (3.27)$$

$$\begin{aligned} \frac{\partial f_1}{\partial H_{i,j}} = & \left(\frac{\partial u_\lambda}{\partial \eta} + \cos \phi \frac{\partial u_\phi}{\partial \phi} - u_\phi \sin \phi \right) \frac{\partial h}{\partial H_{i,j}} \\ & + (u_\lambda - \text{Src} \cos \phi) \frac{\partial \left(\frac{\partial h}{\partial \eta} \right)}{\partial H_{i,j}} + u_\phi \cos \phi \frac{\partial \left(\frac{\partial h}{\partial \phi} \right)}{\partial H_{i,j}} \end{aligned} \quad (3.28)$$

$$\frac{\partial f_1}{\partial c} = -\text{Sr} \cos \phi \frac{\partial h}{\partial \eta}. \quad (3.29)$$

Similar expressions can be obtained for the λ and ϕ momentum equations. The derivatives of the field variables with respect to each coefficient are readily calculated from the individual series expansions. For example,

$$\frac{\partial u_\lambda}{\partial P_{i,j}} = \cos(\kappa i \eta) \cos((2j - 1)\phi). \quad (3.30)$$

Using this method we populate $3MN$ rows of the Jacobian matrix corresponding to all $3MN$ collocation grid points.

In addition we must also calculate the Jacobian elements corresponding to the volume specification equation (3.8). Since this equation is independent of u_λ , u_ϕ and c , the only contribution to the Jacobian will come from derivatives with respect to the free-surface coefficients. Letting the volume specification equation be represented by $f_4(\mathbf{a}) = 0$, we have

$$\frac{\partial f_4}{\partial H_{i,j}} = -\frac{4\kappa}{V_z} \int_0^{\pi/\kappa} \int_0^{\pi/2} [h^2 + \hat{a}^2 + 2\hat{a}h] \frac{\partial h}{\partial H_{i,j}} \cos \phi d\phi d\eta \quad (3.31)$$

where

$$\frac{\partial h}{\partial H_{i,j}} = \begin{cases} \cos(2j\phi) & \text{if } \begin{cases} i = 0, \\ j = 0, \dots, N, \end{cases} \\ \cos(\kappa i \eta) (-1)^j [\cos(2j\phi) + \cos(2(j-1)\phi)] & \text{if } \begin{cases} i = 1, \dots, M-1, \\ j = 1, \dots, N. \end{cases} \end{cases} \quad (3.32)$$

Equation (3.31) can be simplified further by analytically evaluating components of the integral that allow manipulation. Appendix A contains the specific details.

3.3.7 Adaptive Integration Method

The integrals appearing in (3.7) and (3.31) are evaluated using numerical quadrature. For the current study the technique of adaptive recursive quadrature is employed to evaluate the integrals, accurate to within a user defined relative tolerance which can be as small as the machine precision of the computer on which the computations are performed. The particular algorithm used is that of adaptive Lobatto quadrature, with Kronrod extension of the Gauss-Lobatto formula, as detailed in Gander & Gautschi[27].

It is required to compute the volume integral (3.7) to high accuracy so that the total volume of fluid is effectively conserved across separate runs of the program. Using adaptive Lobatto quadrature we compute this integral to machine precision with a relative tolerance of 1.0×10^{-14} . In as far as the Jacobian is only used as a means of finding an updating step direction, the machine accuracy employed in calculating (3.7) is not required in the quadrature evaluation of (3.31). In fact, computing (3.31) to high accuracy merely leads to significantly longer computation times with little improvement in the overall direction of the updating step. For this reason the accuracy of the Jacobian elements that are evaluated via quadrature is sacrificed in favour of shorter computation times, with negligible difference in algorithm efficiency in terms of producing a better estimate for the step direction.

3.3.8 Bootstrapping

In the present context we refer to bootstrapping as the process of taking a previous solution and using this as the basis for an initial guess from which a new solution is computed. The solution of the nonlinear problem requires three unique types of bootstrapping.

The first type refers to the process of taking the coefficients and wavespeed computed from the linearized model and computing an associated nonlinear solution. This type of process can be used to compute nonlinear solutions when the corresponding linearized solution is already known. This is only applicable when the amplitude is small so that the nonlinear solution is approximated well by the linearized solution.

The second type of bootstrapping refers to the process of starting with a solution to the nonlinear equations for a given truncation level and forcing one of the coefficients

in such a way as to produce another slightly different solution with the same truncation level. This procedure forms the basis of mapping the wavespeed amplitude relationship as it allows one to slowly increase either the wavespeed or amplitude and incrementally trace out the underlying curve. It is this type of bootstrapping that is employed most intensively in this study.

The third form of bootstrapping refers to taking a solution of the nonlinear system, for a given truncation level, and increasing the truncation and computing the resulting solution. This method can be used to verify numerically computed solutions through a convergence argument. If the solution is shown to change little from one truncation level to another we can be reasonably sure of the solution accuracy, especially if a sizeable magnitude decrease is observed between the first and last coefficient values in each series.

3.4 Solution and Results

3.4.1 Measuring the Amplitude

In order to investigate the relationship between the Rossby wavespeed and the amplitude, we require a means of measuring the amplitude, \mathcal{A} , of a particular Rossby wave. To elucidate this process, we first need to define what amplitude is. For a simple periodic wave pattern, the amplitude can be defined as the maximum deviation of the wave as measured from the mean position to an extreme point. Fundamental to this concept is the establishment of a universally agreed upon mean function value. This mean value is usually chosen to be where the underlying medium would reside if no wave pattern were present. For the case of one isolated periodic wave structure, this position is intuitively obvious.

Now consider the problem of measuring Rossby wave amplitude horizontally on a sphere, as depicted in the polar stereographic projection in Figure 3.1. To be consistent we require just one mean state but due to the multitude of wave shapes that are possible we see that there are an infinite number of mean states about which we can measure wave deviation. We must therefore decide on exactly where to measure amplitude from for any given wave. Because Rossby wave activity is predominantly associated with the mid-latitude regions and also because $\phi = \pm\pi/4$ represents the mid point between the equator and either pole, we choose the mean

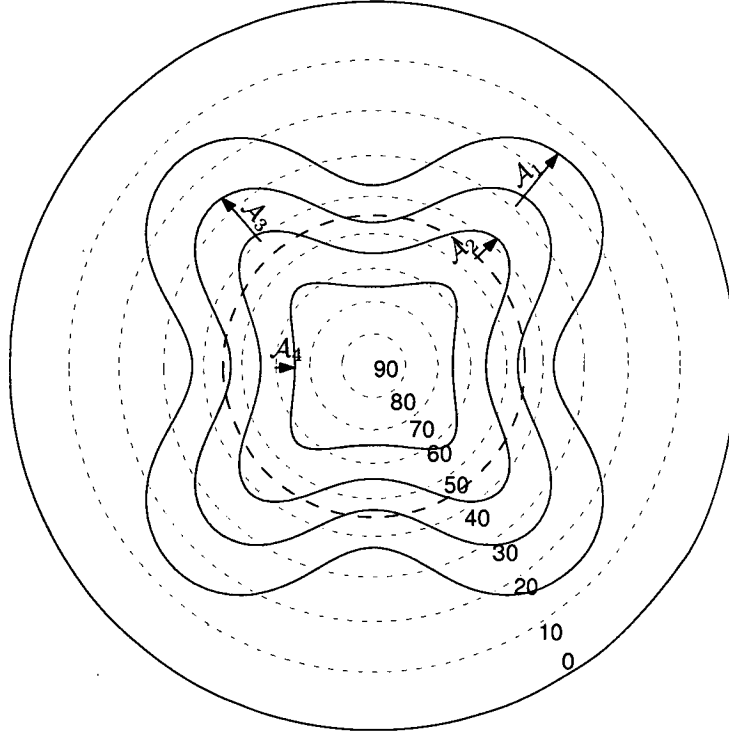


Figure 3.1: Various amplitude measurement methods

reference level as the latitude circle located 45 degrees from the equator in either hemisphere.

We now note that when we refer to progressive Rossby waves we actually mean a progressive-wave pattern as a perturbation from a base zonal flow state. As we have already shown in Section 2.4.1, associated with the base zonal flow state is a zonal free-surface state which has level surfaces lying along latitude circles of constant ϕ . For a given total system volume we can calculate the height of the zonal flow free-surface contours at $\phi = \pm\pi/4$ and then use these base levels to measure how the zonal flow state is deformed when a progressive Rossby wave structure is present. That is, we first record the base zonal height, denoted h_{bz} , of the free-surface at $\phi = \pm\pi/4$ when there is no Rossby wave structure, and then when a Rossby wave structure is present we find the height contour at the level h_{bz} and measure exactly how this level surface has been modified from its base zonal state.

We also note that the amplitudes indicated in Figure 3.1 will in general not be the same in both the equator-ward and pole-ward directions, with the divergence between the two growing as the overall wave amplitude grows. Because of the

topology of the sphere it is possible for a Rossby wave to extend further towards the equator than towards the pole where the lines of longitude converge. Thus to record \mathcal{A} effectively we will need to measure both the equator-ward and pole-ward deflections, which we denote \mathcal{A}_e and \mathcal{A}_p respectively. Associated with these separate but related amplitudes we define a simple averaged amplitude, the mean of the two values, to be

$$\mathcal{A}_{\text{ave}} = \frac{\mathcal{A}_e + \mathcal{A}_p}{2}. \quad (3.33)$$

In forthcoming sections when we present specific results we will plot the wavespeed c versus each of the above defined amplitudes, namely \mathcal{A}_e , \mathcal{A}_p and \mathcal{A}_{ave} .

3.4.2 Parameters and Constants

Although this analysis is not specific to a given sphere size or mass it again seems reasonable, as in the linearized model, to use parameters that closely approximate those of the Earth so that direct comparison can be made between existing meteorological models and observations. With this in mind we adopt the following values for the sphere specific parameters:

$$a = 6.37122 \times 10^6 \text{m}, \quad (3.34)$$

$$\Omega = \frac{2\pi}{24 \times 3600} \approx 7.272 \times 10^{-5} \text{s}^{-1}, \quad (3.35)$$

$$g = 9.80616 \text{m s}^{-2}. \quad (3.36)$$

Additionally we define each characteristic reference scale as

$$v_{\text{ref}} = 40 \text{m s}^{-1}, \quad (3.37)$$

$$h_{\text{ref}} = 8.0 \times 10^3 \text{m}, \quad (3.38)$$

$$c_{\text{ref}} = \frac{\Omega}{30} \approx 2.4241 \times 10^{-6} \text{s}^{-1}. \quad (3.39)$$

For the dimensionless zonal flow parameter ω we will use two specific values. In the linearized model we were afforded the luxury of being able to specify a broad range of ω values with little overhead incurred in terms of time taken to numerically analyze the problem. Unfortunately, in the nonlinear model, we are no longer able to investigate the solution dependency on ω without incurring a significant increase in the computation time. This is because at each value of ω chosen we must compute a complete solution curve for the c versus \mathcal{A} relationship which involves many possible

values of the wavespeed, rather than the single value computed in the linearized model. On average, to compute a complete solution curve for a fixed value of ω , many weeks of computational time is required for programs executing on the previously documented hardware specifications in Section 3.3.1.

For this reason it was decided to restrict the investigation to two specific values of the parameter ω . The first value is consistent with the angular speed ω used in the test set proposed by Williamson et al. [87]. The second value, chosen to be 80% of the first value, provides a slower and perhaps physically more realistic value for the super rotation rate. In dimensionless form the two values are given by

$$\omega_1 \approx 1.25,$$

$$\omega_2 \approx 1.0.$$

The particular values above are obtained by noting that Williamson et al. use a dimensional value for ω of $7.848 \times 10^{-6} \text{ s}^{-1}$, a value first introduced by Phillips[66]. In order to convert this to a dimensionless number it is necessary to multiply by the radius of the Earth and divide by the reference velocity scale so that

$$\omega_1 = \frac{7.848 \times 10^{-6} a}{v_{\text{ref}}} \approx 1.25,$$

$$\omega_2 = 80\% \omega_1 \approx 1.0.$$

It is also necessary to specify a base volume V_z for the system, to be used in the volume specification equation given by (3.8). For this study the value was chosen to be the total volume contained between the surface of the sphere and the free-surface shape defined by the zonal flow with parameters $h_o = 1$ and $\omega = 1.25$. Thus the base volume is simply the total volume of the atmosphere corresponding to purely zonal flow with parameters equivalent to those used in Williamson et al.[87].

3.4.3 Results for $\kappa = 4$, $\omega = 1.25$

We now examine results obtained by solving the equations using the numerical methods previously outlined. Because the process of root finding is quite sensitive to the initial approximation to the root we use the first type of bootstrapping defined in Section 3.3.8 to find an initial small-amplitude solution based on the linearized result for equivalent parameter values in the model. Once we have obtained this small amplitude nonlinear solution we then slowly force the wave amplitude by

holding coefficient $H_{1,1}$ fixed throughout the calculation and increasing its value between successive runs of the program. Using this technique we build up a picture of the overall relationship between the wavespeed and the amplitude.

Figure 3.2 shows the three solution curves when $\kappa = 4$ and $\omega = 1.25$ for each of the three measures of amplitude \mathcal{A}_e , \mathcal{A}_p and \mathcal{A}_{ave} defined previously in Section 3.4.1. The truncation levels are $M = 20$ and $N = 20$ so that each series has a total of 400 coefficients, with a total of 1200 unknowns for the problem. Results were initially computed at a lower truncation level of $M = N = 10$ to ascertain the general nature of the relationship. Once the nature of the solution was established the truncation was increased.

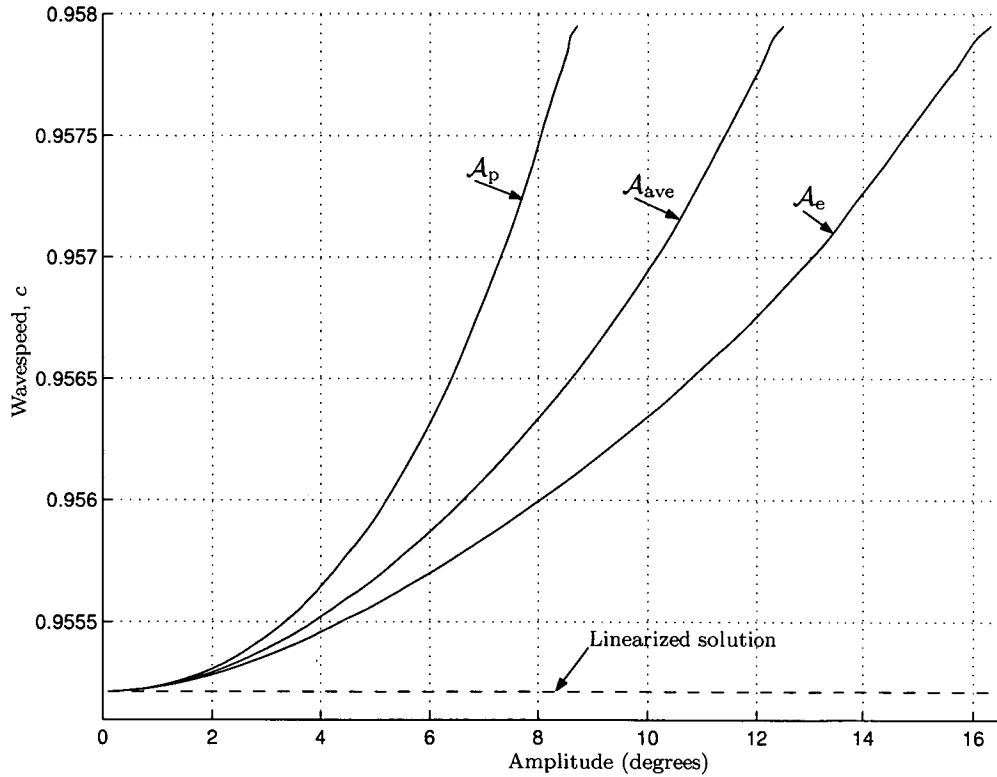


Figure 3.2: Incompressible wavespeed versus amplitude for $\kappa = 4$ and $\omega = 1.25$

The error tolerance on the L^1 norm of the residual vector was set at 10^{-12} , leading to average individual residual errors of the order of 10^{-15} or less. The agreement between the two levels of representation was found to be excellent with results at the higher truncation level only differing marginally from those at the lower level, providing evidence for the numerical convergence of the solutions calculated. In particular, the third type of bootstrapping outlined in Section 3.3.8 was used to

increase the truncation level beyond $M = N = 20$ for a random sample of points on the solution curve, and in all cases these higher resolution solutions were found to differ negligibly from those for $M = N = 20$, and, at least for small amplitude, from those of $M = N = 10$ as well.

The linearized solution is included and indicated in Figure 3.2, showing that for small amplitude waves the linear and nonlinear solutions are essentially equivalent. As the amplitude increases the wavespeed also increases, with the curve initially being tangential to the linearized result for small \mathcal{A} but diverging from the linearized result and increasing more rapidly as \mathcal{A} becomes larger. This behaviour is as expected by analogy with other nonlinear wave calculations for gravitationally influenced incompressible fluids, notably those of Stokes [78], Schwartz [71] and Cokelet [18]. These results, along with contributions from other key researchers in the field, are summarised in the review article by Schwartz & Fenton [73].

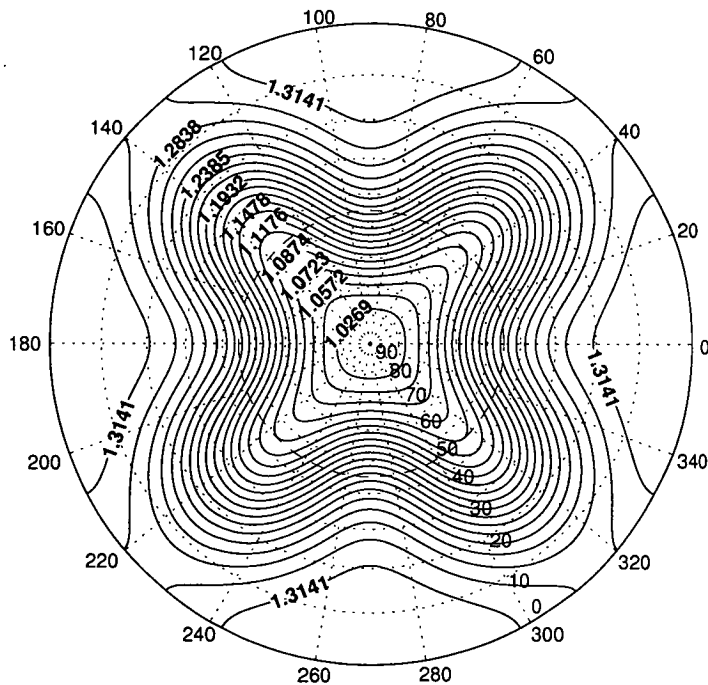


Figure 3.3: Incompressible shallow atmosphere free-surface contours for $\kappa = 4$, $\omega = 1.25$ at limit of computation. The average amplitude is $\mathcal{A}_{ave} = 12.5104(deg.)$ and the wavespeed is $c = 0.9580$.

As the amplitude continues to increase the rate of wavespeed increase grows rapidly until, ultimately, a limiting case is achieved numerically, where a slight curling over of the curve is observed. The physical explanation of this limiting solution is not

clear from this example computation. It is possible, for example, that a sharp crest might be formed somewhere in the flow field, as in the previously mentioned water-wave case studied by Stokes and later by Schwartz. Alternatively, it may be the case that the solution is topologically limited by enclosing bubbles, as found for the case of gravity waves with surface tension by Schwartz & Vanden-Broeck [72], and Chen & Saffman [15]. However, an analysis of the free-surface contours at this limiting wavespeed and amplitude combination, as shown in Figure 3.3, suggests that no such behaviour is present.

We suggest, however, that some type of nonlinear resonance behaviour occurs, which is not accessible to this numerical scheme because of the complexity of the solution space and the implied sensitivity of Newton's method to the initial guess used. Evidence supporting this statement is presented in the next section. Indeed, it is suspected that the limiting wavespeed-amplitude combination indicated in Figure 3.2 is only really limited by the numerical solution method and that, in reality, significantly faster and larger waves exist beyond the shown limit. Exhaustive attempts to find such larger waves were made using numerous methods. In particular the algorithm was changed so that the wavespeed became the forcing parameter in an attempt to look for faster progressive waves; however convergence of the residual vector was not obtained. In addition, the results obtained with the lower truncation level of $M = N = 10$ were found to converge for slightly larger amplitudes and wavespeeds, although it was then found that subsequent bootstrapping of these lower resolution solutions to ones at a higher resolution produced non-convergent residuals. We must therefore reject these results at this point until further analytical and numerical work can be done to investigate this behaviour.

3.4.4 Results for $\kappa = 4$, $\omega = 1.0$

The solution curves shown in Figure 3.4 represent results obtained with the values $\kappa = 4$ and $\omega = 1.0$. The truncation levels were set at $M = N = 15$ with initial curves mapped out using $M = N = 10$; little overall difference was observed between the two resolutions. The error tolerance on the L^1 norm of the residual vector was set at 10^{-12} , leading to average individual residual errors of the order of 10^{-15} or less. Like the previous example, the solution agrees well with the linearized result for small amplitude waves and as \mathcal{A} increases so does the wavespeed c . However, as opposed to the previous case for $\omega = 1.25$, distinct discontinuous jumps are now evident,

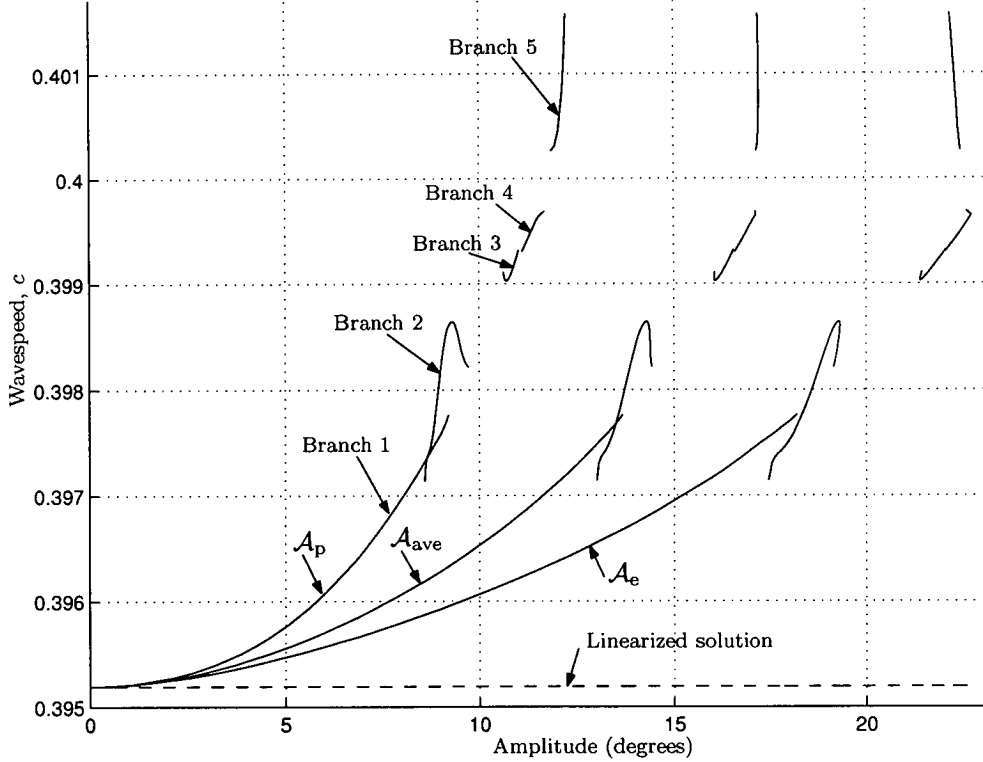


Figure 3.4: Incompressible wavespeed versus amplitude for $\kappa = 4$ and $\omega = 1.0$

dividing the solution curves into separate branches, between which no numerical solutions were able to be computed to adequate convergence. The individual branches have been labelled in the figure and will be referred to subsequently as branches 1 through 5 respectively.

Discrete branching of the solution, as evidenced in the present results, is characteristic of nonlinear resonance interaction in general, in which certain energy states of the system can be viewed as sympathetically exciting the underlying wave motion, undergoing energy exchange between waves of different wavelengths in the process. Nonlinear resonance has been known to exist in complex nonlinear wave propagation problems for some time now. In the context of gravity waves with surface tension Wilton [88] encountered key values of the capillary number at which resonance occurred. Schwartz & Vanden-Broeck [72], and Hogan [34, 35, 36], confirmed this behaviour in detail, by numerically solving the exact equations, and found that multiple simultaneous solution branches were possible. Forbes [24, 25] also found resonant behaviour for surface waves of large amplitude beneath an elastic sheet.

In the meteorological context, nonlinear resonance behaviour has been studied by

Longuet-Higgins & Gill [57] who showed that resonant interactions over time can exist between three waves, termed a resonant triad, obeying certain algebraic relationships relating the individual wavenumbers, associated with each physical dimension, and corresponding wavespeeds; their results are concerned with planetary waves both on the β -plane and more generally on a spherical surface. Both Hoskins [39] and Baines [6] extend this work by considering the stability of planetary waves and calculating amplitudes required for instability based on triad interactions for specific types of Rossby-Haurwitz waves.

To understand how the resonance is occurring in this particular example we can view the system as being forced by the parametrized amplitude through the Fourier coefficient $H_{1,1}$. As $H_{1,1}$ increases we see \mathcal{A} and c also increasing until suddenly some of the Fourier modes in our series expansions are naturally excited by the forcing and can absorb energy via nonlinear interactions. At this point resonance occurs and the system becomes unstable in the sense that unchanging progressive waves are no longer possible. We can thus think of resonance in this instance as a parameter region of, possibly highly oscillatory, transition between two stable progressive states for the full nonlinear time dependent problem. The fundamental nature of any resonance demands that the amplitude of the dominant harmonic wave grow in time. As we are only concerned with progressive waves this type of behaviour is excluded at the outset when we defined our travelling coordinate transform. However, as indicated by our results, the method used is still able to expose fundamental resonances of the system where full time dependence would be necessary to discern the complete behaviour of the dynamical system.

The separate branches of the solution curve shown in Figure 3.4 can be classified, at least partially, in terms of the general associated height field structure and corresponding velocity vector field along each solution curve segment. On branch 1 we conclude that at no point in the flow does the fluid move counter to the general direction of the overall wave propagation direction and additionally that the only stagnation points in the flow field are located at either of the two topological poles, as expected. The free-surface contours at the limiting upper value of branch 1 are shown in Figure 3.5. It is observed that the general character of these contours is quite similar to those obtained with both the linearized model and Rossby-Haurwitz theory of Section 2.6.3 of the previous chapter.

Not much difference was observed between the solutions along branch 1 and those

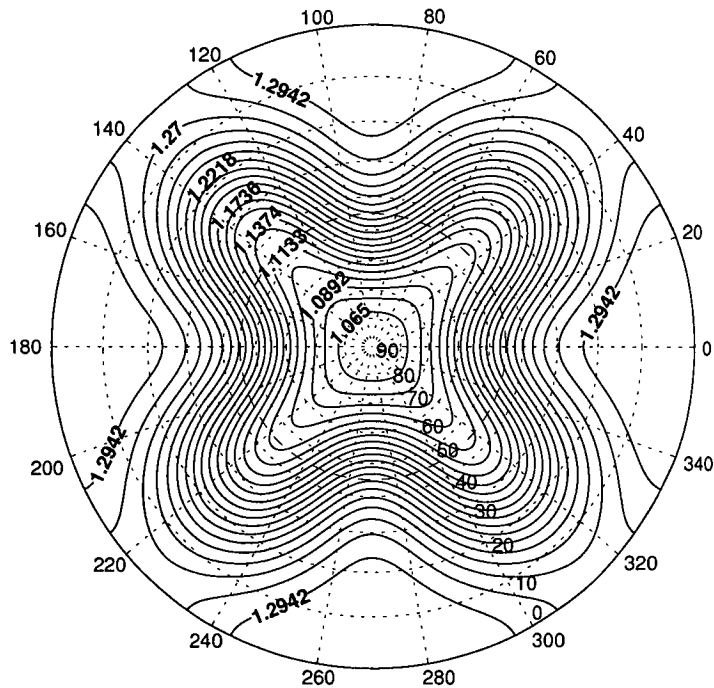


Figure 3.5: Incompressible shallow atmosphere free-surface contours at end of branch 1 for $\kappa = 4$, $\omega = 1.0$. The average amplitude is $\mathcal{A}_{ave} = 13.6732(deg.)$ and the wavespeed is $c = 0.3978$.

along branch 2, with the general flow properties of the previous paragraph applying equally well here. It is also important to emphasize that the apparent intersection of branches 1 and 2 in the diagram is not a bifurcation point. Examination of the Fourier coefficients in the neighbourhood of the overlap shows distinctly different solution structure for each branch which fail to converge to a common set, despite the fact that the values of \mathcal{A} and c for the two branches coincide at this point. It would be possible to prove this with a simple analysis of the determinant of the Jacobian near the point of apparent intersection, as in Chen & Saffman [15]; however the ease with which the Newton method iterates through this region seems to suggest that no further investigation is necessary with regard to the possible existence of a bifurcation. Additionally, the solution curve for the equatorial amplitude \mathcal{A}_e does not contain the intersection, which confirms the presence of a resonance branch, instead of a simple bifurcation.

Solutions on branches 3 and above reveal richer dynamics in terms of more stagnation points in the flow field, reverse flow leading to localised circulation, and highly nonlinear wave profiles. The main difference between the lower solution branches 1

and 2 and the upper solution branches 3, 4 and 5 can be expressed by examining the number of stagnation points in the flow field, disregarding the obvious polar stagnation points that all solutions must have by definition of the series expansions themselves. It is evident that for solutions on branches 3 and higher, all have stagnation points located symmetrically on the equator about the coordinate lines $\eta = \frac{2n\pi}{\kappa}$, for $n = 0, 1, \dots, \kappa - 1$. The exact position of these stagnation points was noted to change as the amplitude varied, although typically they were located quite close to the symmetry lines themselves. In between the two stagnation points the fluid was observed to flow counter to the general direction of the progressive-wave movement. The height field was examined for small-scale localised high pressure cells at these points of circulation, but none were found. However this does not contradict geostrophic theory, which is primarily valid at mid latitudes rather than at the equator.

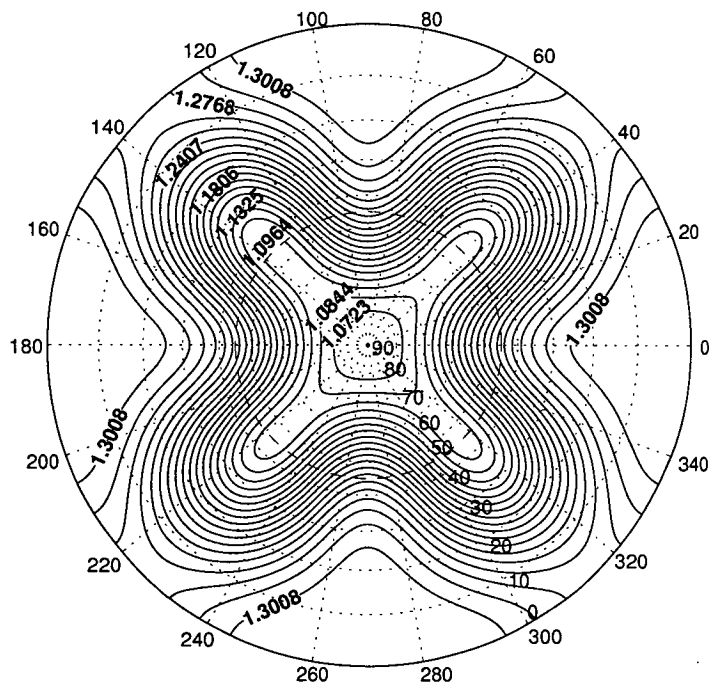


Figure 3.6: Incompressible shallow atmosphere free-surface contours at end of branch 4 for $\kappa = 4$, $\omega = 1.0$. The average amplitude is $\mathcal{A}_{ave} = 17.11662(deg.)$ and the wavespeed is $c = 0.3997$.

Figure 3.6 shows a typical free-surface contour plot for solutions along branches 3 and 4. The figure actually shows the contours at the limiting upper value of branch 4 and so represents the maximum allowable amplitude for waves on branch 4. It

seems, from an analysis of the velocity fields and height contours, that the qualitative difference between waves on branches 3 and 4 is negligible. Nonetheless, a distinct gap was encountered when trying to establish the continuity of the solution between branches 3 and 4. Further investigation is needed to establish the key qualitative differences between these two branches, although this is both beyond the scope and computational capability of the present work.

Of particular note is the way in which low-level polar heights, and hence pressures, are seen to move equator-ward for solutions along these branches. It is suspected that the limiting factor for wavespeeds and amplitudes towards the upper end of branch 4 is directly related to the topology of the low-level free-surface contours which are not able to bend inwards any further without creating an isolated cut-off low pressure system in the flow field. This statement is supported by the following analysis of branch 5 solutions.

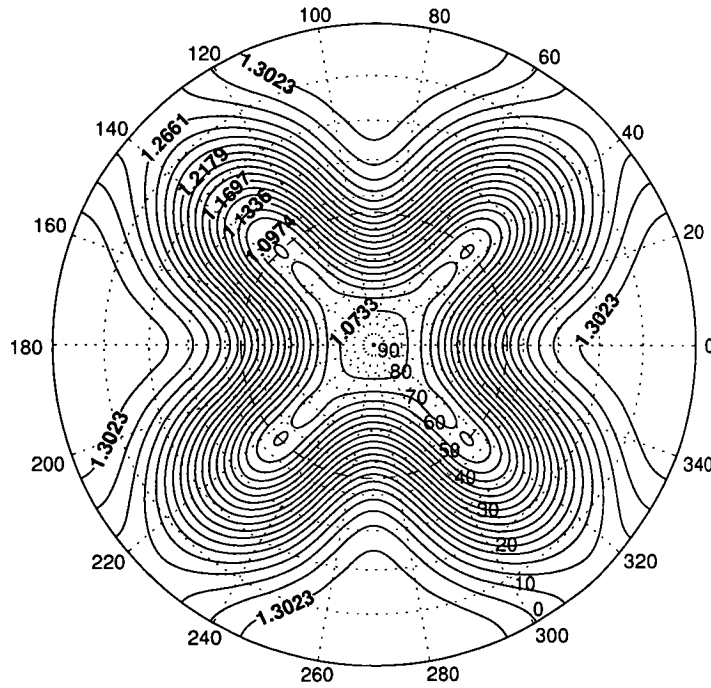


Figure 3.7: Incompressible shallow atmosphere free-surface contours at end of branch 5 for $\kappa = 4$, $\omega = 1.0$. The average amplitude is $\mathcal{A}_{ave} = 17.11662(deg.)$ and the wavespeed is $c = 0.4016$.

The highly nonlinear free-surface height contours for the upper end of branch 5 are shown in Figure 3.7. It is immediately evident that solutions along this branch have the distinguishing feature of cut-off low pressure cells which are isolated from the

general progressive-wave structure. In addition to the already mentioned stagnation points in the flow field for waves on branches 3 and higher, more stagnation points are introduced for waves on the fifth branch, this time occurring close to the poles of the coordinate system rather than near the equator. It was initially suspected that the centre of each cut-off low pressure cell must be a stagnation point; however careful analysis of the velocity vector field did not confirm this. Nonetheless the velocity in the vicinity of these cells is quite small compared to the rest of the flow field and can almost be described as circulatory about the centre of each cell.

It is of interest to note that the stagnation points introduced for branch 5 solutions occur immediately below each cut-off low pressure cell as indicated in figure 3.8. Also shown are all previously mentioned stagnation points as well as regions of circulation, labeled reverse flow. We can conclude that generally the flow is seen to be geostrophic in the sense that the streamlines are nearly parallel to the isobars. This is clearly true in the neighbourhood of the perturbed $\phi = \pm\pi/4$ zonal flow contour that forms the basis of the numerical analysis in this section.

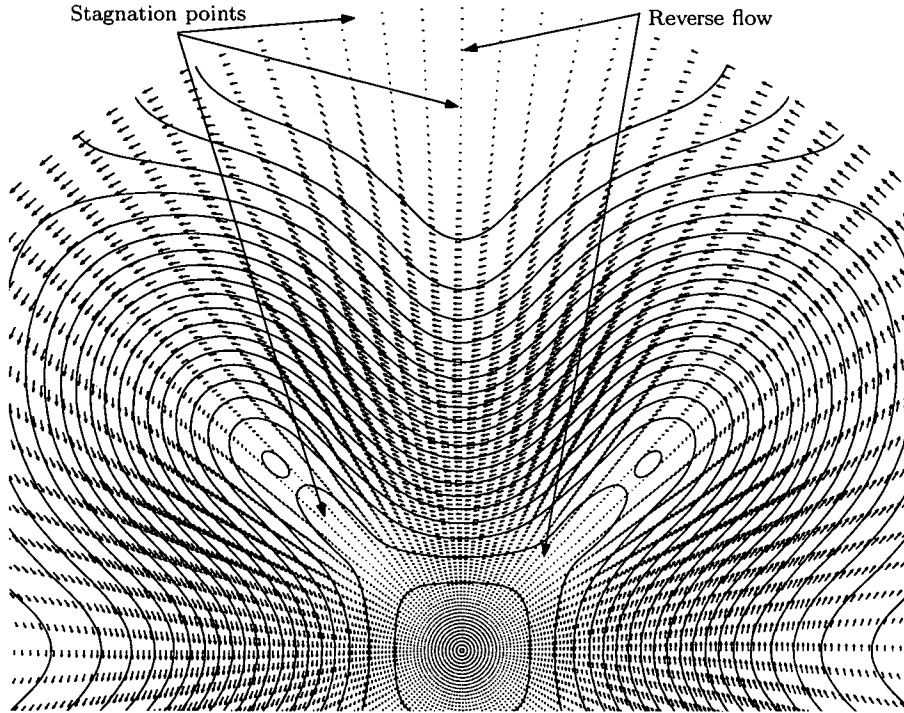


Figure 3.8: Incompressible shallow atmosphere free-surface contours with corresponding velocity vector field at end of branch 5 for $\kappa = 4$, $\omega = 1.0$. The average amplitude is $\mathcal{A}_{ave} = 17.11662(deg.)$ and the wavespeed is $c = 0.4016$.

The fate of the solution curves past the end of branch 5 is still uncertain. Attempts were made to compute more points beyond the limits shown but in all cases convergence was not achieved. It might be that our numerical method is not well suited to computing past points where the slope of the curve is nearly infinite, in which case improved techniques are required to investigate the behaviour past the limit shown. Alternatively this may be close to the maximum allowable amplitude of the system, imposed as a consequence of the finite size and topology of the sphere. An analysis of the constraints of potential vorticity conservation of Rossby waves on a β -plane by Lindzen & Schoeberl [52] revealed that there are finite limits to the size of Rossby wave amplitudes. This reasoning should apply even more so to the sphere where the finite size becomes an important attribute of the problem.

3.4.5 Results for $\kappa = 5$, $\omega = 1.25$

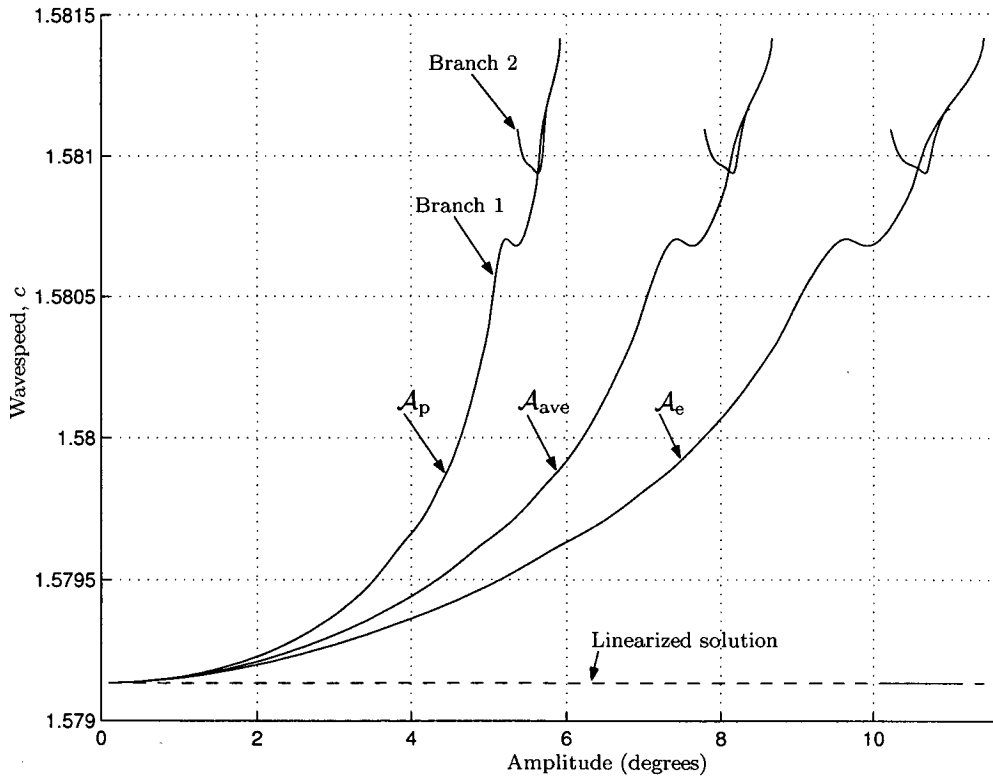


Figure 3.9: Incompressible wavespeed versus amplitude for $\kappa = 5$ and $\omega = 1.25$

It is of interest to study how the dynamical system behaves with an alternative value of the wave number κ . We now present results obtained with $\kappa = 5$, using the same pair of values ($\omega = 1.25$ and $\omega = 1.0$) for the dimensionless zonal flow super rotation;

in this section we examine the case $\omega = 1.25$. Figure 3.9 shows the computed wavespeed versus amplitude relationship using a truncation of $M = N = 20$. The error tolerance on the L^1 norm of the residual vector was set at 10^{-12} , leading to average individual residual errors of the order of 10^{-15} or less.

The same general trend as for $\kappa = 4$ is encountered here for $\kappa = 5$, with the linearized solution being a good approximation to the nonlinear solution for small \mathcal{A} and the wavespeed becoming increasingly greater as the amplitude is increased. It appears that the use of $\kappa = 5$ introduces a new phenomenon in the form of a localised cubic structure located near $c \approx 1.5807$. It was initially suspected that this was in fact two distinct branches separated by a resonance; however it was possible to compute continuously through this region, using a very small step size, without encountering any non convergent solutions.

Therefore it seems that there are at least two explanations for this behaviour. The first is that there is in fact a resonance occurring near the point of inflexion, but existing on such a small scale that we were unable to detect it on any occasion. This does not seem very likely given the nature of the previous nonlinear resonances observed for the case $\kappa = 4$, $\omega = 1.0$. The second explanation is that this is a feature of the dynamics and forcing, in which energy exchange between certain wavelengths is taking place in such a manner as to increase the overall amplitude while at the same time reducing the wavespeed. If so, this would represent a type of damped resonance, but careful analytical work, beyond the scope of this study, would be needed to identify the physical nature of the damping mechanism. Despite this localised reversal of the general trend of the graph, no obvious distinguishing features are visible when we examine the free-surface contours and velocity vector field in the vicinity of this solution region. This fact seems to support the conjecture that separate resonance branches do not exist in this case.

Two separate solution branches were found to exist towards the upper end of the curve when the limiting amplitude-wavespeed combination was approached. Because it is not entirely clear from the figure, it needs to be emphasized that the first branch terminates in the vicinity of $c \approx 1.5812$; thus the highest possible wavespeed indicated is at the right end of branch 2. It is again unlikely that the apparent intersection of the two branches is a sign of a simple bifurcation, for reasons outlined in the previous section.

For the left end of the second branch, numerical results have in fact been computed well beyond the termination point shown in the figure. However, it appears that they are of questionable validity due to increasing numerical error along that branch and have therefore not been shown. The ultimate fate of this upper branch is not clear and may perhaps require alternative numerical techniques to reveal. In any event it is possible that this branch is physically unstable, the system preferring the lower wavespeed over the higher one, and so would generally not be observed in practice. It is even possible that a physical instability in this branch might produce a numerical instability, since the numerical iteration process may be equivalent to stepping forward in time, as has been shown in various applications of the Peaceman-Rachford ADI method to the heat equation, documented in Ames [3, page 149].

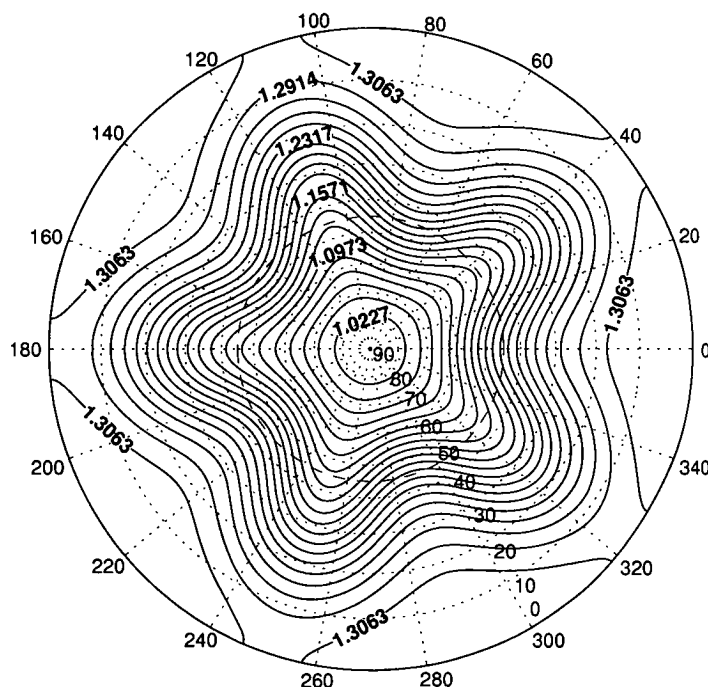


Figure 3.10: Incompressible shallow atmosphere free-surface contours at end of branch 1 for $\kappa = 5$, $\omega = 1.25$. The average amplitude is $\mathcal{A}_{ave} = 8.3678(deg.)$ and the wavespeed is $c = 1.5812$.

Typical free-surface contours of the system are presented in Figure 3.10, showing the nature of the solution at the end of branch 1. In contrast to the highly non-linear structures computed at the end of the curve for $\kappa = 4$ and $\omega = 1.0$, these contours exemplify the significantly smaller maximum amplitude for which a convergent wavespeed was able to be calculated. In addition, no defining qualitative

features of the velocity field were found that could be used to distinguish easily between the two solution branches. It is possible that more solution curves exist beyond those that are indicated; however attempts to find such solutions were not successful.

3.4.6 Results for $\kappa = 5$, $\omega = 1.0$

For completeness we present results in this final section for $\kappa = 5$ and $\omega = 1.0$. Figure 3.11 shows the computed solution curves obtained with the truncation level $M = N = 15$. The error tolerance on the L^1 norm of the residual vector was again set at 10^{-12} . The general features of this figure are less remarkable than those for the preceding set of results obtained with $\omega = 1.25$, although there is some evidence for a similar localised cubic structure, this time in the vicinity of $c = 0.99395$. The severity of this local cubic behaviour, however, is significantly less noticeable and does not substantially influence the general increase of c with \mathcal{A} . As in all previous solution curves presented, the results here agree well with the linearized value of the wavespeed for small values of the amplitude.

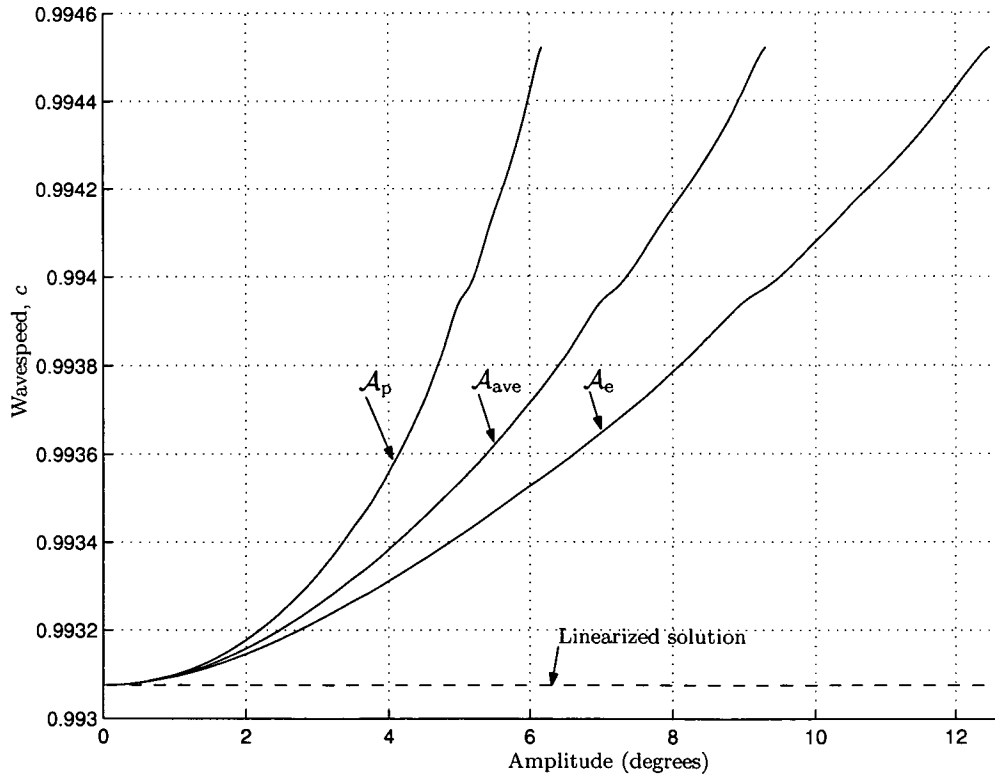


Figure 3.11: Incompressible wavespeed versus amplitude for $\kappa = 5$ and $\omega = 1.0$

Typical free-surface contours at the right end of the one and only computed branch are shown in Figure 3.12. The waves shown are in general highly nonlinear and it should be noted that the maximum possible amplitude obtained with this slower zonal super rotation speed is larger than that obtained with $\omega = 1.25$. No additional stagnation points in the flow field were observed, as in the previous case, and consequently all fluid flow was found to be in the same direction as the direction of propagation of the progressive-wave.

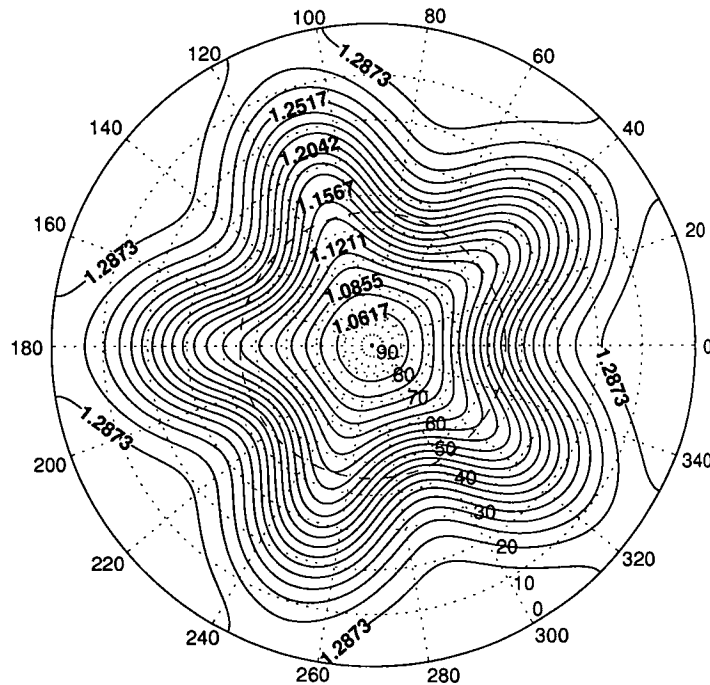


Figure 3.12: Incompressible shallow atmosphere free-surface contours at end of branch 1 for $\kappa = 5$, $\omega = 1.0$. The average amplitude is $\mathcal{A}_{ave} = 9.3175(deg.)$ and the wavespeed is $c = 0.9945$.

It is again suspected that there are in fact more solution branches in addition to the one shown in Figure 3.11. To support this statement we argue that the general nature of the flow field at the limiting computed value seems to be rather well behaved with no clearly identifiable limiting topological features. Unsuccessful attempts were made to bootstrap the limiting solutions to those on another higher branch; in all cases adequate convergence of the residual vector was not achieved.

It is also of interest to point out that the general computed values of the wavespeed for this set of results are similar in magnitude to those computed for $\kappa = 4$ and $\omega = 1.25$. In so far as the qualitative nature of both solution curves is the same,

it seems reasonable to speculate that all solutions in the vicinity of this wavespeed behave in a similar manner. That is to say that a general increase of c is seen with increasing \mathcal{A} for all values of κ and appropriate value of ω .

3.5 Closing Remarks

In this chapter we have successfully solved the complete nonlinear equations governing shallow atmosphere free-surface flow with embedded progressive Rossby wave structures. Solutions in the form of finite Fourier series were obtained using a collocation method with an associated Newton iterative scheme. By starting close to the linearized solutions computed in the previous chapter and forcing the amplitude to increasingly larger values we were able to successfully step along the wavespeed versus amplitude solution curves for specific values of the parameters κ and ω .

Results obtained show that a relationship exists between increasing wave amplitude and wavespeed; these are similar to the well known results for gravity influenced free-surface waves. For the specific case of $\kappa = 4$ and $\omega = 1.0$ we found substantial evidence for nonlinear resonance in the system, with adjacent solution branches being separated by areas in which no solutions could be computed to within reasonable convergence. At the limit of computability it was shown that highly nonlinear wave profiles are possible with areas of cut off low pressure being a key feature of the system at this critical limit. It is suspected that this behaviour exists in general, at least to some extent, for all solutions that were investigated; however attempts to confirm this have thus far been unsuccessful with questionable results. It is highly unlikely that numerical methods alone can answer this existence question. Analytical techniques may be required to address this issue, however these are beyond the scope of the present investigation.

CHAPTER 4

COMPRESSIBLE LINEARIZED SHALLOW ATMOSPHERE MODEL

4.1 Derivation

We consider here the derivation of the compressible shallow atmosphere equations in a rotating spherical coordinate system, again following the general approach developed in Pedlosky[65], with appropriate modifications for a compressible fluid. For ease of reference and completeness we treat the derivation in this section as distinct from that of the incompressible case derived in Section 2.1, although both derivations share some similarities.

Referring to Figure 4.1, define \bar{h} as the radial height above the level surface $r = a$ of a free-surface surrounding a rotating reference sphere of radius $r = a$. Additionally, define h and h_b as the depth of the fluid and the height of the underlying mountains respectively. The height of the free-surface, \bar{h} , can be given in terms of the two parameters h_b and h as

$$\bar{h} = h_b + h. \quad (4.1)$$

Although the generality of this setup affords the representation of a much wider class of problem we will restrict ourselves to the case when there is no underlying mountain specification so that $h_b = 0$, leading to

$$\bar{h} = h. \quad (4.2)$$

For this study we will be concerned with compressible, adiabatic fluid flow. Because

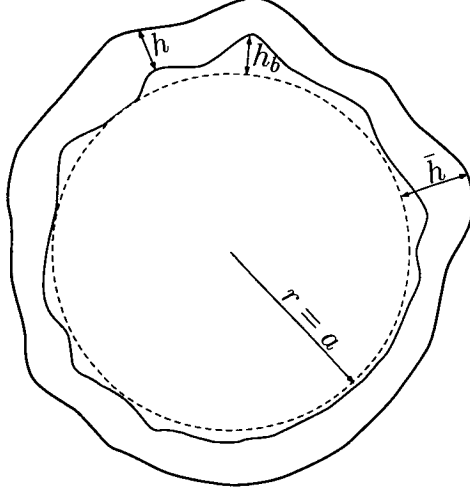


Figure 4.1: Free-surface height parameters

the fluid is adiabatic the rate of heat addition, q_h in (1.4), will be zero. Additionally, due to the nature of the spherical coordinate system the vertical coordinate r appears explicitly in the dynamical equations; however, we can adequately approximate this by $r = a$, see Holton [37]. Adopting the above approximations, we obtain the following modified form for the compressible dynamical equations, (1.6)–(1.11), presented in Chapter 1.

Mass

$$\frac{\partial \rho}{\partial t} + \frac{1}{a \cos \phi} \left[\frac{\partial}{\partial r} (a u_r \rho \cos \phi) + \frac{\partial}{\partial \lambda} (u_\lambda \rho) + \frac{\partial}{\partial \phi} (u_\phi \rho \cos \phi) \right] = 0, \quad (4.3)$$

r momentum

$$\frac{\partial u_r}{\partial t} + u_r \frac{\partial u_r}{\partial r} + \frac{u_\lambda}{a \cos \phi} \frac{\partial u_r}{\partial \lambda} + \frac{u_\phi}{a} \frac{\partial u_r}{\partial \phi} - \frac{u_\lambda^2 + u_\phi^2}{a} - 2\Omega u_\lambda \cos \phi + \frac{1}{\rho} \frac{\partial p}{\partial r} = -g, \quad (4.4)$$

λ momentum

$$\begin{aligned} \frac{\partial u_\lambda}{\partial t} + u_r \frac{\partial u_\lambda}{\partial r} + \frac{u_\lambda}{a \cos \phi} \frac{\partial u_\lambda}{\partial \lambda} + \frac{u_\phi}{a} \frac{\partial u_\lambda}{\partial \phi} + \frac{u_r u_\lambda - u_\lambda u_\phi \tan \phi}{a} \\ + 2\Omega(u_r \cos \phi - u_\phi \sin \phi) + \frac{1}{a \rho \cos \phi} \frac{\partial p}{\partial \lambda} = 0, \end{aligned} \quad (4.5)$$

ϕ momentum

$$\begin{aligned} \frac{\partial u_\phi}{\partial t} + u_r \frac{\partial u_\phi}{\partial r} + \frac{u_\lambda}{a \cos \phi} \frac{\partial u_\phi}{\partial \lambda} + \frac{u_\phi}{a} \frac{\partial u_\phi}{\partial \phi} + \frac{u_r u_\phi + u_\lambda^2 \tan \phi}{a} \\ + 2\Omega u_\lambda \sin \phi + \frac{1}{a \rho} \frac{\partial p}{\partial \phi} = 0, \end{aligned} \quad (4.6)$$

Energy

$$\rho c_v \frac{DT}{Dt} - \frac{p}{\rho} \frac{D\rho}{Dt} = 0, \quad (4.7)$$

Gas Law

$$p = \rho RT. \quad (4.8)$$

Using the gas law, (4.8), we can write the energy equation, (4.7), as

$$\frac{1}{(\gamma - 1)T} \frac{DT}{Dt} - \frac{1}{\rho} \frac{D\rho}{Dt} = 0, \quad (4.9)$$

where we have used the thermodynamic relationship $c_v/R = 1/(\gamma - 1)$. The absence of heat addition makes it possible to integrate the total derivatives in (4.9),

$$\int \frac{DT}{T} = \int (\gamma - 1) \frac{D\rho}{\rho} + \text{constant},$$

to give

$$T(\rho) = A\rho^{\gamma-1}, \quad (4.10)$$

where A is a constant of integration whose value is determined for each specific atmospheric composition. From (4.10) and (4.8) it is immediately obvious that the pressure can also be expressed as a function of density of the form

$$p(\rho) = \beta\rho^\gamma, \quad (4.11)$$

where we have defined the constant $\beta = AR$. Thermodynamically, equation (4.11) indicates that the atmosphere model is polytropic.

The underlying assumption of the shallow atmosphere approximation is that motion mainly occurs on level radial surfaces of the spherical coordinate system and less so in the r direction, effectively confining the velocity to motion that is predominantly tangent to the surface of the sphere. Mathematically we can write this statement as

$$u_r \approx O(\epsilon), \quad (4.12)$$

$$u_\lambda \approx O(1), \quad (4.13)$$

$$u_\phi \approx O(1), \quad (4.14)$$

where ϵ is a small parameter that reflects the shallowness of the atmosphere relative to the radius of the sphere. Consider now the implications of this approximation for the r momentum equation (4.4). We argue that the total derivative terms $\frac{\partial u_r}{\partial t}$,

$u_r \frac{\partial u_r}{\partial r}$, $\frac{u_\lambda}{a \cos \phi} \frac{\partial u_r}{\partial \lambda}$ and $\frac{u_\phi}{a} \frac{\partial u_r}{\partial \phi}$ are all $O(\epsilon)$ so that the r momentum equation reduces to

$$-\frac{u_\lambda^2 + u_\phi^2}{a} - 2\Omega u_\lambda \cos \phi + \frac{1}{\rho} \frac{\partial p}{\partial r} = -g. \quad (4.15)$$

Additionally, we assume that (4.15) is dominated by hydrostatics¹ so that effectively we have

$$\frac{\partial p}{\partial r} = -\rho g, \quad (4.16)$$

which in conjunction with (4.11), we arrive at

$$\rho^{\gamma-2} \frac{\partial \rho}{\partial r} = \frac{-g}{\beta \gamma}.$$

Integration with respect to r yields

$$\rho^{\gamma-1}(r, \lambda, \phi, t) = f_1(\lambda, \phi, t) - \frac{g(\gamma-1)r}{\beta \gamma}.$$

The value of $f_1(\lambda, \phi, t)$ is ascertained by assuming that on the free-surface, $r = a + \bar{h}(\lambda, \phi, t)$, the density has the constant value ρ_0 , so that

$$\rho^{\gamma-1}(r, \lambda, \phi, t) = \rho_0^{\gamma-1} + \frac{g(\gamma-1)}{\beta \gamma} (a + \bar{h}(\lambda, \phi, t) - r). \quad (4.17)$$

Using (4.17) we can solve for ρ . With the addition of (4.10) and (4.11) we obtain formulae for the thermodynamic variables in the problem. The results are

$$\rho(r, \lambda, \phi, t) = \left[\rho_0^{\gamma-1} + \frac{g(\gamma-1)}{\beta \gamma} (a + \bar{h}(\lambda, \phi, t) - r) \right]^{\frac{1}{\gamma-1}}, \quad (4.18)$$

$$p(r, \lambda, \phi, t) = \beta \left[\rho_0^{\gamma-1} + \frac{g(\gamma-1)}{\beta \gamma} (a + \bar{h}(\lambda, \phi, t) - r) \right]^{\frac{\gamma}{\gamma-1}}, \quad (4.19)$$

$$T(r, \lambda, \phi, t) = A \left[\rho_0^{\gamma-1} + \frac{g(\gamma-1)}{\beta \gamma} (a + \bar{h}(\lambda, \phi, t) - r) \right]. \quad (4.20)$$

From (4.18) and (4.19) we can show that

$$\frac{\partial p}{\partial \lambda} = g\rho \frac{\partial \bar{h}}{\partial \lambda}, \quad (4.21)$$

$$\frac{\partial p}{\partial \phi} = g\rho \frac{\partial \bar{h}}{\partial \phi}, \quad (4.22)$$

¹We can be more rigorous than this and use a scale analysis approach to argue this point. See Pedlosky[65, page 60] for the finer details of this process

so that the pressure gradient terms in the λ and ϕ momentum equations, (4.5) and (4.6), are given by

$$\frac{1}{\rho} \frac{\partial p}{\partial \lambda} = g \frac{\partial \bar{h}}{\partial \lambda}, \quad (4.23)$$

$$\frac{1}{\rho} \frac{\partial p}{\partial \phi} = g \frac{\partial \bar{h}}{\partial \phi}. \quad (4.24)$$

Equations (4.23) and (4.24) imply that the horizontal pressure gradient terms are r -independent, which in turn implies that all accelerations in (4.5) and (4.6) must also be r -independent. Thus the individual velocity components are r -independent if they are initially so, see [65], leading to

$$u_\lambda \equiv u_\lambda(\lambda, \phi, t), \quad (4.25)$$

$$u_\phi \equiv u_\phi(\lambda, \phi, t). \quad (4.26)$$

Using the shallow atmosphere approximation contained in (4.12)–(4.14), the two remaining momentum equations, (4.5) and (4.6), become

λ momentum

$$\frac{\partial u_\lambda}{\partial t} + \frac{u_\lambda}{a \cos \phi} \frac{\partial u_\lambda}{\partial \lambda} + \frac{u_\phi}{a} \frac{\partial u_\lambda}{\partial \phi} - \frac{u_\lambda u_\phi \tan \phi}{a} - 2\Omega u_\phi \sin \phi + \frac{g}{a \cos \phi} \frac{\partial \bar{h}}{\partial \lambda} = 0, \quad (4.27)$$

ϕ momentum

$$\frac{\partial u_\phi}{\partial t} + \frac{u_\lambda}{a \cos \phi} \frac{\partial u_\phi}{\partial \lambda} + \frac{u_\phi}{a} \frac{\partial u_\phi}{\partial \phi} + \frac{u_\lambda^2 \tan \phi}{a} + 2\Omega u_\lambda \sin \phi + \frac{g}{a} \frac{\partial \bar{h}}{\partial \phi} = 0. \quad (4.28)$$

We now consider the task of integrating the mass equation, (4.3), with respect to the radial coordinate r . We introduce the function

$$\rho_I = \int \rho(r, \lambda, \phi, t) dr \quad (4.29)$$

so that

$$\rho = \frac{\partial \rho_I}{\partial r}. \quad (4.30)$$

The definition of ρ_I , in combination with (4.25) and (4.26), enables the mass equation to be written as

$$\frac{\partial}{\partial r} \left[\frac{\partial \rho_I}{\partial t} + \frac{1}{a \cos \phi} \left(a u_r \cos \phi \frac{\partial \rho_I}{\partial r} + \frac{\partial}{\partial \lambda} (u_\lambda \rho_I) + \frac{\partial}{\partial \phi} (u_\phi \rho_I \cos \phi) \right) \right] = 0, \quad (4.31)$$

which can be integrated with respect to r and manipulated to give

$$u_r \rho + \frac{\partial \rho_I}{\partial t} + \frac{1}{a \cos \phi} \frac{\partial}{\partial \lambda} (u_\lambda \rho_I) + \frac{1}{a \cos \phi} \frac{\partial}{\partial \phi} (u_\phi \rho_I \cos \phi) = f_2(\lambda, \phi, t). \quad (4.32)$$

To determine $f_2(\lambda, \phi, t)$ we note that on the lower boundary we must have no normal flow, otherwise the fluid would penetrate the surface and breach the conservation of mass requirement. Thus on $r = a + h_b(\lambda, \phi)$ we must enforce the condition $\mathbf{q} \cdot \mathbf{n} = 0$ where \mathbf{n} is a normal to the surface. We can easily show that the normal to the lower boundary is given by

$$\mathbf{n} = \mathbf{e}_r - \frac{1}{a \cos \phi} \frac{\partial h_b}{\partial \lambda} \mathbf{e}_\lambda - \frac{1}{a} \frac{\partial h_b}{\partial \phi} \mathbf{e}_\phi, \quad (4.33)$$

so that

$$\mathbf{q} \cdot \mathbf{n} = u_r(a + h_b, \lambda, \phi, t) - \frac{u_\lambda}{a \cos \phi} \frac{\partial h_b}{\partial \lambda} - \frac{u_\phi}{a} \frac{\partial h_b}{\partial \phi} = 0. \quad (4.34)$$

Solving for u_r we obtain

$$u_r(a + h_b, \lambda, \phi, t) = \frac{u_\lambda}{a \cos \phi} \frac{\partial h_b}{\partial \lambda} + \frac{u_\phi}{a} \frac{\partial h_b}{\partial \phi}. \quad (4.35)$$

Substituting (4.35) into (4.32) and evaluating at $r = a + h_b$ allows us to solve for $f_2(\lambda, \phi, t)$, which we in turn substitute back into (4.32). After simplification we obtain

$$\begin{aligned} u_r \rho + \frac{\partial \rho_I}{\partial t} + \frac{1}{a \cos \phi} \frac{\partial}{\partial \lambda} (u_\lambda \rho_I) + \frac{1}{a \cos \phi} \frac{\partial}{\partial \phi} (u_\phi \rho_I \cos \phi) - \frac{\partial \rho_I}{\partial t} \Big|_{a+h_b} \\ - \rho|_{a+h_b} \left[\frac{u_\lambda}{a \cos \phi} \frac{\partial h_b}{\partial \lambda} + \frac{u_\phi}{a} \frac{\partial h_b}{\partial \phi} \right] - \frac{1}{a \cos \phi} \frac{\partial}{\partial \lambda} (u_\lambda \rho_I) \Big|_{a+h_b} \\ - \frac{1}{a \cos \phi} \frac{\partial}{\partial \phi} (u_\phi \rho_I \cos \phi) \Big|_{a+h_b} = 0 \end{aligned} \quad (4.36)$$

where $\rho|_{a+h_b}$ is taken to mean ρ evaluated at $r = a + h_b$, similarly for ρ_I and its derivatives.

On the upper boundary we enforce the kinematic condition

$$\frac{D}{Dt} [r - a - \bar{h}(\lambda, \phi, t)] = 0,$$

which states that the fluid can not penetrate the free-surface. Expanding the total derivative and solving for u_r gives

$$u_r(a + \bar{h}, \lambda, \phi, t) = \frac{\partial \bar{h}}{\partial t} + \frac{u_\lambda}{a \cos \phi} \frac{\partial \bar{h}}{\partial \lambda} + \frac{u_\phi}{a} \frac{\partial \bar{h}}{\partial \phi}. \quad (4.37)$$

Finally, substitution of (4.37) into (4.36) and subsequent simplification yields the

incompressible shallow atmosphere mass equation given by

$$\begin{aligned}
 & \left[\rho|_{a+\bar{h}} \frac{\partial \bar{h}}{\partial t} + \frac{\partial \rho_I}{\partial t} \Big|_{a+\bar{h}} - \frac{\partial \rho_I}{\partial t} \Big|_{a+h_b} \right] + \left[\frac{u_\lambda \rho|_{a+\bar{h}}}{a \cos \phi} \frac{\partial \bar{h}}{\partial \lambda} + \frac{1}{a \cos \phi} \frac{\partial}{\partial \lambda} (u_\lambda \rho_I) \Big|_{a+\bar{h}} \right. \\
 & \quad \left. - \frac{u_\lambda \rho|_{a+h_b}}{a \cos \phi} \frac{\partial h_b}{\partial \lambda} - \frac{1}{a \cos \phi} \frac{\partial}{\partial \lambda} (u_\lambda \rho_I) \Big|_{a+h_b} \right] + \left[\frac{u_\phi \rho|_{a+\bar{h}}}{a} \frac{\partial \bar{h}}{\partial \phi} \right. \\
 & \quad \left. + \frac{1}{a \cos \phi} \frac{\partial}{\partial \phi} (u_\phi \rho_I \cos \phi) \Big|_{a+\bar{h}} - \frac{u_\phi \rho|_{a+h_b}}{a} \frac{\partial h_b}{\partial \phi} \right. \\
 & \quad \left. - \frac{1}{a \cos \phi} \frac{\partial}{\partial \phi} (u_\phi \rho_I \cos \phi) \Big|_{a+h_b} \right] = 0. \tag{4.38}
 \end{aligned}$$

Equation (4.38) can be simplified considerably by noting that the derivatives of ρ_I can be expressed in terms of the density, ρ , and the free-surface, \bar{h} . Substitution of (4.18) into (4.29) and subsequent evaluation of the integral yields

$$\rho_I(r, \lambda, \phi, t) = -\frac{\beta}{g} \left[\rho_0^{\gamma-1} + \frac{g(\gamma-1)}{\beta\gamma} (a + \bar{h}(\lambda, \phi, t) - r) \right]^{\frac{\gamma}{\gamma-1}} + c_0 \tag{4.39}$$

$$= -\frac{1}{g} p(r, \lambda, \phi, t) + c_0, \tag{4.40}$$

for constant of integration c_0 . We now use (4.39) to calculate derivatives of ρ_I with respect to λ , ϕ and t . It is straightforward to show that

$$\frac{\partial \rho_I}{\partial t} = -\rho \frac{\partial \bar{h}}{\partial t}, \quad \frac{\partial \rho_I}{\partial \lambda} = -\rho \frac{\partial \bar{h}}{\partial \lambda}, \quad \frac{\partial \rho_I}{\partial \phi} = -\rho \frac{\partial \bar{h}}{\partial \phi},$$

and these expressions may now be used to simplify the mass equation so that algebraic manipulation of (4.38) leads to

$$\begin{aligned}
 & \rho|_{a+h_b} \frac{\partial \bar{h}}{\partial t} + \frac{1}{a \cos \phi} (\rho_I|_{a+\bar{h}} - \rho_I|_{a+h_b}) \left[\frac{\partial u_\lambda}{\partial \lambda} + \frac{\partial}{\partial \phi} (u_\phi \cos \phi) \right] \\
 & \quad + \frac{\rho|_{a+h_b}}{a \cos \phi} \left[u_\lambda \left(\frac{\partial \bar{h}}{\partial \lambda} - \frac{\partial h_b}{\partial \lambda} \right) + u_\phi \cos \phi \left(\frac{\partial \bar{h}}{\partial \phi} - \frac{\partial h_b}{\partial \phi} \right) \right] = 0 \tag{4.41}
 \end{aligned}$$

In this study we are only concerned with the special case of bottom topography in which $h_b = 0$. Thus, from equation (4.2), we have equality of the depth of the atmosphere, h , and the free-surface height, \bar{h} , allowing us to drop the overbar ($\bar{}$) notation and simplify further to give

$$\begin{aligned}
 & \rho|_a \frac{\partial h}{\partial t} + \frac{1}{a \cos \phi} (\rho_I|_{a+h} - \rho_I|_a) \left[\frac{\partial u_\lambda}{\partial \lambda} + \frac{\partial}{\partial \phi} (u_\phi \cos \phi) \right] \\
 & \quad + \frac{\rho|_a}{a \cos \phi} \left[u_\lambda \frac{\partial h}{\partial \lambda} + u_\phi \cos \phi \frac{\partial h}{\partial \phi} \right] = 0. \tag{4.42}
 \end{aligned}$$

Note that from (4.40) we can replace all occurrences of ρ_I with equivalent pressure terms so that we can also write (4.42) as

$$\rho|_a \frac{\partial h}{\partial t} + \frac{1}{a \cos \phi} \left[\frac{\partial}{\partial \lambda} \left(\frac{u_\lambda}{g} (p|_a - p|_{a+h}) \right) + \frac{\partial}{\partial \phi} \left(\frac{u_\phi \cos \phi}{g} (p|_a - p|_{a+h}) \right) \right] = 0. \quad (4.43)$$

As a check of the validity of this equation we note that if the fluid is incompressible, that is ρ is constant, then $p = p_0 + \rho g(a + h - r)$ so that

$$p|_a - p|_{a+h} = \rho g h,$$

and thus (4.43) becomes

$$\frac{\partial h}{\partial t} + \frac{1}{a \cos \phi} \left[\frac{\partial}{\partial \lambda} (u_\lambda h) + \frac{\partial}{\partial \phi} (u_\phi h \cos \phi) \right] = 0,$$

which is identical to (2.27) from the incompressible derivation.

To the extent that the aim of this study is to investigate progressive Rossby wave structures, we again introduce a coordinate frame involving the progressive angular wavespeed c and longitudinal and time coordinates, λ and t , as in Section 2.2 of Chapter 2. We define

$$\eta = \lambda - ct$$

as the new travelling coordinate system, with the effect of the $-ct$ term being to translate any initial wave structure either towards the west ($c < 0$) or towards the east ($c > 0$) with constant angular speed c .

Applying the coordinate transformation to the governing equations and writing $f = 2\Omega \sin \phi$, we can express the complete dimensional dynamical equations of motion for a thin layer of compressible fluid with a free-surface in a rotating spherical coordinate system as

mass

$$-cga \cos \phi \rho|_a \frac{\partial h}{\partial \eta} + \left[\frac{\partial}{\partial \eta} (u_\lambda (p|_a - p|_{a+h})) + \frac{\partial}{\partial \phi} (u_\phi \cos \phi (p|_a - p|_{a+h})) \right] = 0, \quad (4.44)$$

λ momentum

$$\left(\frac{u_\lambda}{a} - c \cos \phi \right) \frac{\partial u_\lambda}{\partial \eta} + \frac{u_\phi \cos \phi}{a} \frac{\partial u_\lambda}{\partial \phi} - \left(f \cos \phi + \frac{u_\lambda}{a} \sin \phi \right) u_\phi + \frac{g}{a} \frac{\partial h}{\partial \eta} = 0, \quad (4.45)$$

ϕ momentum

$$\left(\frac{u_\lambda}{a} - c \cos \phi \right) \frac{\partial u_\phi}{\partial \eta} + \frac{u_\phi \cos \phi}{a} \frac{\partial u_\phi}{\partial \phi} + \left(f \cos \phi + \frac{u_\lambda}{a} \sin \phi \right) u_\lambda + \frac{g \cos \phi}{a} \frac{\partial h}{\partial \eta} = 0, \quad (4.46)$$

where the density and pressure are defined by

$$\rho(r, \eta, \phi) = \left[\rho_0^{\gamma-1} + \frac{g(\gamma-1)}{\beta\gamma} (a + h(\eta, \phi) - r) \right]^{\frac{1}{\gamma-1}} \quad (4.47)$$

and

$$p(r, \eta, \phi) = \beta \left[\rho_0^{\gamma-1} + \frac{g(\gamma-1)}{\beta\gamma} (a + h(\eta, \phi) - r) \right]^{\frac{\gamma}{\gamma-1}} \quad (4.48)$$

respectively.

4.2 Non-dimensionalization and Problem Simplification

4.2.1 Non-dimensionalization

We now consider the non-dimensionalization of the compressible shallow atmosphere equations. First we define the following characteristic values, for each reference scale contained in the problem, as

$$\begin{aligned} v_{\text{ref}} &\equiv \text{characteristic speed,} \\ h_{\text{ref}} &\equiv \text{characteristic free-surface height,} \\ c_{\text{ref}} &\equiv \text{characteristic angular speed,} \\ \rho_{\text{ref}} &\equiv \text{characteristic density,} \\ p_{\text{ref}} &\equiv \text{characteristic pressure.} \end{aligned}$$

Using these dimensional characteristic values we now rescale all the field variables to dimensionless form giving

$$\hat{u}_\lambda = \frac{u_\lambda}{v_{\text{ref}}} \Rightarrow u_\lambda = v_{\text{ref}} \hat{u}_\lambda, \quad (4.49)$$

$$\hat{u}_\phi = \frac{u_\phi}{v_{\text{ref}}} \Rightarrow u_\phi = v_{\text{ref}} \hat{u}_\phi, \quad (4.50)$$

$$\hat{h} = \frac{h}{h_{\text{ref}}} \Rightarrow h = h_{\text{ref}} \hat{h}, \quad (4.51)$$

$$\hat{c} = \frac{c}{c_{\text{ref}}} \Rightarrow c = c_{\text{ref}} \hat{c}, \quad (4.52)$$

$$\hat{\rho} = \frac{\rho}{\rho_{\text{ref}}} \Rightarrow \rho = \rho_{\text{ref}} \hat{\rho}, \quad (4.53)$$

$$\hat{p} = \frac{p}{p_{\text{ref}}} \Rightarrow p = p_{\text{ref}} \hat{p}, \quad (4.54)$$

where the hat $\hat{\cdot}$ denotes a dimensionless variable. Substituting equations (4.49)–(4.54) into (4.44), (4.45), (4.46) and manipulating, we obtain

mass

$$-Sr\hat{c}\hat{p}|_a \cos \phi \frac{\partial \hat{h}}{\partial \eta} + \left(\frac{Fr}{M}\right)^2 \left[\frac{\partial}{\partial \eta} (\hat{u}_\lambda (\hat{p}|_a - \hat{p}|_{a+h})) + \frac{\partial}{\partial \phi} (\hat{u}_\phi \cos \phi (\hat{p}|_a - \hat{p}|_{a+h})) \right] = 0, \quad (4.55)$$

λ momentum

$$(\hat{u}_\lambda - Sr \hat{c} \cos \phi) \frac{\partial \hat{u}_\lambda}{\partial \eta} + \hat{u}_\phi \cos \phi \frac{\partial \hat{u}_\lambda}{\partial \phi} - \left(\frac{\cos \phi}{Ro} + \hat{u}_\lambda \right) \hat{u}_\phi \sin \phi + \frac{1}{Fr^2} \frac{\partial \hat{h}}{\partial \eta} = 0, \quad (4.56)$$

ϕ momentum

$$(\hat{u}_\lambda - Sr \hat{c} \cos \phi) \frac{\partial \hat{u}_\phi}{\partial \eta} + \hat{u}_\phi \cos \phi \frac{\partial \hat{u}_\phi}{\partial \phi} + \left(\frac{\cos \phi}{Ro} + \hat{u}_\lambda \right) \hat{u}_\lambda \sin \phi + \frac{\cos \phi}{Fr^2} \frac{\partial \hat{h}}{\partial \phi} = 0, \quad (4.57)$$

where the four dimensionless flow regime parameters are defined as

$$Sr = \frac{a c_{ref}}{v_{ref}} \quad \text{Strouhal number}, \quad (4.58)$$

$$Fr = \frac{v_{ref}}{\sqrt{g h_{ref}}} \quad \text{Froude number}, \quad (4.59)$$

$$Ro = \frac{v_{ref}}{2\Omega a} \quad \text{Rossby number}, \quad (4.60)$$

$$M = \frac{v_{ref}}{\sqrt{\frac{p_{ref}}{\rho_{ref}}}} \quad \text{Mach number}. \quad (4.61)$$

In addition to the above set of equations, we also need to find the dimensionless forms of (4.47) and (4.48). Recall that the thermodynamic relationship between density and pressure is given by equation (4.11), for some constant β . We stipulate that when p is at its reference value, so is ρ . Thus the value of β is given as $\beta = p_{ref}/\rho_{ref}^\gamma$, for appropriate characteristic values of the density and pressure. Using this definition we can write (4.47) as

$$\hat{\rho}(r, \eta, \phi) = \left[\left(\frac{\rho_0}{\rho_{ref}} \right)^{\gamma-1} + \frac{(\gamma-1)}{\gamma} \left(\frac{M}{Fr} \right)^2 \left(\frac{a}{h_{ref}} + \hat{h}(\eta, \phi) - \frac{r}{h_{ref}} \right) \right]^{\frac{1}{\gamma-1}}. \quad (4.62)$$

Similarly, from (4.48), we obtain

$$\hat{p}(r, \eta, \phi) = \left[\left(\frac{\rho_0}{\rho_{ref}} \right)^{\gamma-1} + \frac{(\gamma-1)}{\gamma} \left(\frac{M}{Fr} \right)^2 \left(\frac{a}{h_{ref}} + \hat{h}(\eta, \phi) - \frac{r}{h_{ref}} \right) \right]^{\frac{\gamma}{\gamma-1}}. \quad (4.63)$$

4.2.2 Problem Simplification

In the thermodynamic variable derivation process we assumed that the density on the free-surface was given by the constant value ρ_0 . It is entirely reasonable to

stipulate that this constant value is zero, so that the atmosphere ranges in density and pressure from high values on the surface of the sphere to increasingly lower values as we approach the free-surface, on which the values drop to zero. This idea is consistent with the concept of the atmosphere ending and is more plausible than arbitrarily ascribing a value to the free-surface density. For this reason we will adopt the value $\rho_0 = 0$ for all subsequent work in the remainder of this thesis. In doing so we significantly simplify the governing dynamical equations.

Putting $\rho_0 = 0$ into (4.62) and (4.63) gives

$$\hat{\rho}(r, \eta, \phi) = \left[\frac{(\gamma - 1)}{\gamma} \left(\frac{M}{Fr} \right)^2 \left(\frac{a}{h_{ref}} + \hat{h}(\eta, \phi) - \frac{r}{h_{ref}} \right) \right]^{\frac{1}{\gamma-1}} \quad (4.64)$$

and

$$\hat{p}(r, \eta, \phi) = \left[\frac{(\gamma - 1)}{\gamma} \left(\frac{M}{Fr} \right)^2 \left(\frac{a}{h_{ref}} + \hat{h}(\eta, \phi) - \frac{r}{h_{ref}} \right) \right]^{\frac{\gamma}{\gamma-1}}, \quad (4.65)$$

so that $\hat{p}|_{a+h} = 0$. Substituting (4.64) and (4.65) into (4.55), expanding the derivatives, and subsequent algebraic manipulation yields a modified continuity equation of the form

$$\begin{aligned} (\hat{u}_\lambda - Sr \hat{c} \cos \phi) \frac{\partial \hat{h}}{\partial \eta} + \hat{u}_\phi \cos \phi \frac{\partial \hat{h}}{\partial \phi} \\ + \frac{(\gamma - 1)}{\gamma} \hat{h} \left[\frac{\partial \hat{u}_\lambda}{\partial \eta} + \cos \phi \frac{\partial \hat{u}_\phi}{\partial \phi} - \hat{u}_\phi \sin \phi \right] = 0. \end{aligned} \quad (4.66)$$

Note that (4.66) is similar in form to its incompressible equivalent given by (2.43), the only difference coming from the $(\gamma - 1)/\gamma$ factor multiplying the divergence terms. This simplified form is a direct consequence of stipulating that the atmospheric density and pressure on the upper boundary of the atmosphere is zero. The equations to be used throughout the rest of this chapter are the set formed from conservation of mass (4.66), the two horizontal components of the conservation of momentum (4.56) and (4.57), and the thermodynamic descriptors (4.64) and (4.65). For the sake of brevity, we now dispense with the hat ($\hat{\cdot}$) notation and all variables will be assumed dimensionless unless otherwise stated.

4.3 Linearization of the Equations

We again construct a purely zonal base flow that only depends on latitude ϕ and has no u_ϕ component. In a similar manner to Section 2.4.1 we can show that a zonal

flow solution of (4.66), (4.56) and (4.57) is given by

$$u_{\lambda z} = \omega \cos \phi, \quad (4.67)$$

$$u_{\phi z} = 0, \quad (4.68)$$

$$h_z = h_o + \frac{\omega \text{Fr}^2}{2} \left(\frac{1}{\text{Ro}} + \omega \right) \cos^2 \phi. \quad (4.69)$$

where the parameter ω is the non-dimensional representation of the base angular speed of the flow and subscript z denotes field variables belonging to the zonal flow structure. The constant of integration h_o is used to specify the non-dimensional height of the free-surface at the poles.

Perturbations of size $O(\epsilon)$ about this flow state are constructed in the form

$$u_\lambda(\eta, \phi) = u_{\lambda z} + \epsilon \cos(\kappa\eta) \Lambda(\phi) + O(\epsilon^2), \quad (4.70)$$

$$u_\phi(\eta, \phi) = 0 + \epsilon \sin(\kappa\eta) \Phi(\phi) + O(\epsilon^2), \quad (4.71)$$

$$h(\eta, \phi) = h_z + \epsilon \cos(\kappa\eta) \mathcal{H}(\phi) + O(\epsilon^2), \quad (4.72)$$

where the parameter κ specifies the wavenumber of the solution. Equations (4.70)–(4.72) are substituted into (4.66), (4.56) and (4.57) and the set of equations are taken to $O(\epsilon)$. By defining the $O(\epsilon)$ terms according to (4.70)–(4.72) we remove the η dependence entirely from the linearized partial differential equations, transforming them into a set of ordinary differential and algebraic equations given by

mass

$$\begin{aligned} & -\kappa(\omega - \text{Sr } c) \cos \phi \mathcal{H}(\phi) + \Phi(\phi) \cos \phi \frac{d h_z}{d \phi} \\ & + \frac{(\gamma - 1)}{\gamma} h_z \left[-\kappa \Lambda(\phi) + \cos \phi \frac{d \Phi(\phi)}{d \phi} - \Phi(\phi) \sin \phi \right] = 0, \end{aligned} \quad (4.73)$$

λ momentum

$$-\kappa(\omega - \text{Sr } c) \cos \phi \Lambda(\phi) - \left(\frac{1}{\text{Ro}} + 2\omega \right) \Phi(\phi) \sin \phi \cos \phi - \frac{\kappa}{\text{Fr}^2} \mathcal{H}(\phi) = 0, \quad (4.74)$$

ϕ momentum

$$\kappa(\omega - \text{Sr } c) \Phi(\phi) + \left(\frac{1}{\text{Ro}} + 2\omega \right) \Lambda(\phi) \sin \phi + \frac{1}{\text{Fr}^2} \frac{d \mathcal{H}(\phi)}{d \phi} = 0. \quad (4.75)$$

The set of equations (4.73)–(4.75) are the linearized equations for compressible shallow atmosphere flow.

4.4 Numerical Solution of the Linearized Equations

Solutions of (4.73)–(4.75) are sought in the form of truncated Fourier series with specific symmetry conditions. We restrict the set of possible solutions to those that have u_λ and h symmetric and u_ϕ anti-symmetric with respect to the equator ($\phi = 0$). Additionally we require that u_λ and u_ϕ are zero at the poles, while h needs to be constant at the poles ($\phi = \pm\pi/2$). The functions that meet these prescribed conditions can be given by

$$\Lambda(\phi) = \sum_{n=1}^N P_{\kappa,n} \cos((2n-1)\phi), \quad (4.76)$$

$$\Phi(\phi) = \sum_{n=1}^N Q_{\kappa,n} \sin(2n\phi), \quad (4.77)$$

$$\mathcal{H}(\phi) = \sum_{n=1}^N H_{\kappa,n} (-1)^n [\cos(2n\phi) + \cos(2(n-1)\phi)], \quad (4.78)$$

where subscript κ on each coefficient denotes the longitudinal wavenumber and N is a positive integer truncation level. The particular form of (4.78) is due to the process of basis recombination, as discussed in Section 2.5.1 of Chapter 2.

To solve for the wavespeed c and associated coefficients $P_{\kappa,n}$, $Q_{\kappa,n}$ and $H_{\kappa,n}$ we exploit the orthogonality properties of the trigonometric functions by requiring that the residual equations, obtained after substituting (4.76)–(4.78) into (4.73)–(4.75), be orthogonal to each of our expansion functions. This technique amounts to the standard Galerkin method in which each residual equation is multiplied by each basis function in turn and integrated over the domain $-\pi/2 \leq \phi \leq \pi/2$. After considerable algebraⁱⁱ, in which the integrals are evaluated in closed form in a manner similar to Section 2.5.2, a generalized eigenvalue problem is constructed of the form

$$A\mathbf{x} = cB\mathbf{x}, \quad (4.79)$$

where A and B are matrices corresponding to the left and right-hand sides of each of the algebraic equations obtained from orthogonality. The eigenvalue c is the wavespeed for the progressive Rossby wave, and vector \mathbf{x} is the eigenvector of unknown linearized coefficients which is defined as

$$\mathbf{x} = [H_{\kappa,1}, \dots, H_{\kappa,N}, P_{\kappa,1}, \dots, P_{\kappa,N}, Q_{\kappa,1}, \dots, Q_{\kappa,N}]^T. \quad (4.80)$$

ⁱⁱSee Appendix B for the individual component equation derivations.

We note that the general structure of both A and B is that of banded diagonal matrices with A also containing banded sub and super-diagonal components. In particular we note that diagonal matrix B consists of non-zero elements along the main diagonal and thus will be invertible, implying that it will always be possible to find solutions of the generalized eigensystem, provided $B^{-1}A$ is non-singular.

4.5 Solution and Results

4.5.1 Model Parameters

We now specify the particular values for the dimensional parameters in the model, using values that closely approximate those of the Earth. We define the radius, angular speed and gravitational acceleration of the sphere to be

$$a = 6.37122 \times 10^6 \text{ m}, \quad (4.81)$$

$$\Omega = \frac{2\pi}{24 \times 3600} \approx 7.272 \times 10^{-5} \text{ s}^{-1}, \quad (4.82)$$

$$g = 9.80616 \text{ m s}^{-2}. \quad (4.83)$$

The characteristic scales for the horizontal wind speed and Rossby wavespeed are again given by

$$v_{\text{ref}} = 40 \text{ m s}^{-1}, \quad (4.84)$$

$$c_{\text{ref}} = \frac{\Omega}{30} \approx 2.4241 \times 10^{-6} \text{ s}^{-1}. \quad (4.85)$$

For the characteristic pressure and density we will use the average sea-level values for the Earth, which are given by

$$p_{\text{ref}} = 1.01 \times 10^5 \text{ kg m}^{-1} \text{ s}^{-2}, \quad (4.86)$$

$$\rho_{\text{ref}} = 1.29 \text{ kg m}^{-3}, \quad (4.87)$$

and the ratio of specific heats, γ , is given by the usual value of $\gamma = 7/5 = 1.4$. We have intentionally not specified a base reference scale h_{ref} for the free-surface height. Rather, we wish to determine an appropriate value for h_{ref} that will make the pressure and density attain characteristic values on the surface of the sphere.

To elucidate this process we consider a model atmosphere of uniform depth h_{ref} , where the density and pressure are respectively given by (4.64) and (4.65). Our aim is as follows; we wish to find a value for the reference height h_{ref} so that the

non-dimensional density and pressure at sea level are equal to unity. That is, the dimensional density and pressure at sea-level take their characteristic values. Since the free-surface has height everywhere given by the constant h_{ref} , the value of $\hat{h}(\eta, \phi)$ in (4.64) and (4.65) will be the constant $\hat{h} = 1$. Additionally, because we are evaluating on the surface of the sphere, we will have $r = a$ so that the density at sea-level is given by

$$\hat{\rho}(a) = \left[\frac{(\gamma - 1)}{\gamma} \left(\frac{M}{\text{Fr}} \right)^2 \right]^{\frac{1}{\gamma-1}}. \quad (4.88)$$

By substituting the dimensionless parameters M and Fr , given by (4.61) and (4.59), into (4.88) and setting $\hat{\rho}(a) = 1$ we can solve for h_{ref} to obtain

$$h_{\text{ref}} = \frac{\gamma p_{\text{ref}}}{(\gamma - 1)g\rho_{\text{ref}}}. \quad (4.89)$$

Using this value of h_{ref} ensures that the sea-level density and pressure are consistent with that observed on the Earth. For the particular reference and parameter values defined above we have

$$h_{\text{ref}} \approx 27.944 \times 10^3 \text{ m}.$$

Note that this is considerably larger than the value of $8.0 \times 10^3 \text{ m}$ used in the incompressible model in Chapters 2 and 3.

4.5.2 Zonal Flow Parameters and Mass Specification

So that we can compare solutions for different values of the zonal flow angular speed ω it is necessary to derive a mass specification condition, similar to the volume specification condition of Section 2.6.2. To perform this analysis we define a base system mass denoted by M_b . We choose M_b to be the mass of the atmosphere without any super rotation so that the free-surface has a uniform non-dimensional height of 1 everywhere and the total mass is just given by the contribution of mass elements in the region bounded inside the two concentric spheres of radii \hat{a} and $\hat{a} + 1$. The dimensionless form of the sphere's radius is the constant \hat{a} , which is just the dimensional value divided by the reference height of the free-surface. Using this notation we can rewrite the expression for the density, (4.64), in the form

$$\rho(r, \eta, \phi) = \left[\frac{(\gamma - 1)}{\gamma} \left(\frac{M}{\text{Fr}} \right)^2 \left(\hat{a} + \hat{h}(\eta, \phi) - \hat{r} \right) \right]^{\frac{1}{\gamma-1}} \quad (4.90)$$

Thus the base mass is given by

$$\begin{aligned}
 M_b &= \int_0^{2\pi} \int_{-\pi/2}^{\pi/2} \int_{\hat{a}}^{\hat{a}+1} \rho(\hat{r}) \hat{r}^2 \cos \phi \, d\hat{r} d\phi d\eta \\
 &= 4\pi \int_{\hat{a}}^{\hat{a}+1} \rho(\hat{r}) \hat{r}^2 \, d\hat{r}
 \end{aligned} \tag{4.91}$$

With a considerable amount of algebra the integral given by (4.91) can be evaluated in closed form. Defining

$$\beta = \frac{(\gamma - 1)}{\gamma} \left(\frac{M}{Fr} \right)^2, \tag{4.92}$$

$$f_1 = \beta(\hat{a} + 1), \tag{4.93}$$

we have

$$\begin{aligned}
 M_b &= 4\pi \int_{\hat{a}}^{\hat{a}+1} \rho(\hat{r}) \hat{r}^2 \, d\hat{r} \\
 &= \frac{4\pi(\gamma - 1)\beta^{\frac{3-2\gamma}{\gamma-1}}}{\gamma(2\gamma - 1)(3\gamma - 2)} [2f_1^2(\gamma - 1)^2 + 2\beta f_1(\gamma - 1)\gamma\hat{a} + \beta^2\gamma(2\gamma - 1)\hat{a}^2].
 \end{aligned} \tag{4.94}$$

The value given by (4.94) constitutes the base reference mass which will remain constant throughout all subsequent calculations.

In a similar manner to the previous mass calculation, we can calculate the mass for a given zonal flow structure specified by the parameters h_o and ω . The zonal mass, denoted M_z , is given by

$$\begin{aligned}
 M_z &= \int_0^{2\pi} \int_{-\pi/2}^{\pi/2} \int_{\hat{a}}^{\hat{a}+h_z(\phi)} \rho(\hat{r}, \phi) \hat{r}^2 \cos \phi \, d\hat{r} d\phi d\eta \\
 &= 4\pi \int_0^{\pi/2} \int_{\hat{a}}^{\hat{a}+h_z(\phi)} \rho(\hat{r}, \phi) \hat{r}^2 \, d\hat{r} d\phi.
 \end{aligned} \tag{4.95}$$

Defining $f_2(\phi) = \beta(\hat{a} + h_z(\phi))$ we have

$$\begin{aligned}
 M_z &= \frac{4\pi(\gamma - 1)\beta^{\frac{3-2\gamma}{\gamma-1}}}{\gamma(2\gamma - 1)(3\gamma - 2)} \times \\
 &\quad \int_0^{\pi/2} h_z^{\frac{\gamma}{\gamma-1}} [2f_2^2(\gamma - 1)^2 + 2\beta f_2(\gamma - 1)\gamma\hat{a} + \beta^2\gamma(2\gamma - 1)\hat{a}^2] \cos \phi \, d\phi.
 \end{aligned} \tag{4.96}$$

In general we will specify a value for ω and then find the value of h_o that makes the zonal mass M_z equivalent to the base mass M_b . That is, for a given value of ω , we need to solve for h_o that satisfies

$$1 - \frac{M_z(h_o)}{M_b} = 0. \quad (4.97)$$

This is accomplished, in the present work, by employing a Newton root finding method.

4.5.3 Results for $\kappa = 3, 4$ and 5

The solution of the generalized eigenvalue problem for the linearized system was achieved by implementing a MATLAB script that assembled the left and right hand side matrices and then solved the resulting system by using the inbuilt routine `eig(A,B)` to find the eigenvalues and corresponding eigenvectors. Although the linearized system will have a total of $3N$ eigenvalue-eigenvector pairs for integer truncation N , in this study, for reasons outlined previously in Section 2.6.2 of Chapter 2, we are only concerned with the primary physical eigenvalue of the system. The primary physical eigenvalue is so labelled since it is the main solution of the system and corresponds to Rossby waves in the sense of a well defined physically reasonable wave structure and wavespeed.

N	3	5	10	100	$O(\text{Coeff}_{100})$
$H_{3,1}$	-9.1054E-03	-8.6326E-03	-8.6749E-03	-8.6752E-03	1.0E-010
$H_{3,2}$	-4.7581E-03	-4.5063E-03	-4.5278E-03	-4.5279E-03	
$H_{3,3}$	1.8093E-03	2.1599E-03	2.1821E-03	2.1823E-03	
$P_{3,1}$	-1.2470E-01	-1.1821E-01	-1.1879E-01	-1.1879E-01	1.0E-06
$P_{3,2}$	-4.4615E-01	-4.2300E-01	-4.2509E-01	-4.2510E-01	
$P_{3,3}$	-1.4778E-01	-1.1667E-01	-1.1669E-01	-1.1669E-01	
$Q_{3,1}$	-6.9464E-01	-6.5860E-01	-6.6183E-01	-6.6185E-01	1.0E-07
$Q_{3,2}$	-1.8072E-01	-1.7181E-01	-1.7270E-01	-1.7270E-01	
$Q_{3,3}$	8.2411E-03	3.6124E-02	3.7022E-02	3.7033E-02	
c	-3.2732E-02	-3.0990E-02	-3.0990E-02	-3.0990E-02	-

Table 4.1: Convergence of compressible wavespeed and first three coefficients in each series for increasing N , $\kappa = 3$.

All computations were performed on an AMD Athlon(tm) XP 1800+ processor clocked at 1.54 GHz. Various truncation levels were chosen to check convergence of the algorithm and in all cases rapid convergence was observed for increasing N .

Tables 4.1, 4.2 and 4.3 illustrate this rapid convergence for $\kappa = 3, 4$ and 5 respectively. The final column in each table gives the order of the last coefficient in each series when $N = 100$ and provides evidence for the accuracy of the solution since in each case the coefficients are observed to drop off reasonably fast. Convergence of the eigenvalue was obtained with smaller truncation than that required for corresponding accuracy in the coefficients, providing confidence in the accuracy of the wavespeeds calculated.

N	3	5	10	100	$O(\text{Coeff}_{100})$
$H_{4,1}$	-8.9296E-03	-8.5877E-03	-8.5884E-03	-8.5884E-03	1.0E-17
$H_{4,2}$	-3.5334E-03	-3.4524E-03	-3.4527E-03	-3.4527E-03	
$H_{4,3}$	3.2098E-03	3.3605E-03	3.3608E-03	3.3608E-03	
$P_{4,1}$	-1.0787E-01	-1.0371E-01	-1.0372E-01	-1.0372E-01	1.0E-14
$P_{4,2}$	-5.0855E-01	-4.8726E-01	-4.8729E-01	-4.8729E-01	
$P_{4,3}$	-2.6010E-01	-2.2920E-01	-2.2922E-01	-2.2922E-01	
$Q_{4,1}$	-9.2662E-01	-8.9120E-01	-8.9126E-01	-8.9126E-01	1.0E-14
$Q_{4,2}$	-4.0757E-01	-3.8689E-01	-3.8692E-01	-3.8692E-01	
$Q_{4,3}$	8.1376E-03	3.6334E-02	3.6339E-02	3.6339E-02	
c	9.4027E-01	9.4351E-01	9.4351E-01	9.4351E-01	-

Table 4.2: Convergence of compressible wavespeed and first three coefficients in each series for increasing N , $\kappa = 4$.

N	3	5	10	100	$O(\text{Coeff}_{100})$
$H_{5,1}$	-8.7573E-03	-8.8926E-03	-8.8539E-03	-8.8539E-03	1.0E-13
$H_{5,2}$	-2.6638E-03	-2.6678E-03	-2.6562E-03	-2.6562E-03	
$H_{5,3}$	4.2517E-03	4.2289E-03	4.2113E-03	4.2112E-03	
$P_{5,1}$	-9.5624E-02	-9.7098E-02	-9.6676E-02	-9.6676E-02	1.0E-9
$P_{5,2}$	-5.4770E-01	-5.5740E-01	-5.5498E-01	-5.5498E-01	
$P_{5,3}$	-3.4186E-01	-3.5640E-01	-3.5482E-01	-3.5482E-01	
$Q_{5,1}$	-1.1484E+00	-1.1662E+00	-1.1611E+00	-1.1611E+00	1.0E-10
$Q_{5,2}$	-6.5400E-01	-6.6863E-01	-6.6572E-01	-6.6572E-01	
$Q_{5,3}$	1.2470E-03	-1.2695E-02	-1.2554E-02	-1.2554E-02	
c	1.5653E+00	1.5638E+00	1.5638E+00	1.5638E+00	-

Table 4.3: Convergence of compressible wavespeed and first three coefficients in each series for increasing N , $\kappa = 5$.

It is of interest to note that although we are now modelling a compressible atmosphere, the results obtained are generally quite similar to those from the incompressible model of Chapter 2. However, it is quite remarkable that the wavespeeds computed between the two models are consistently similar despite the fact that

the incompressible and compressible models have average free-surface heights that are quite different; the reference height in the compressible model is approximately three and a half times larger than that used in the incompressible model. Therefore it seems highly likely that when Phillips [66] first prescribed the value of $h_{\text{ref}} = 8.0 \times 10^3 \text{ m}$ for the incompressible dynamics, some consideration must have been given to the compressibility of the atmosphere.

To provide evidence supporting the accuracy of the linearized solutions computed, it is again useful to make a comparison between these solutions and the equivalent corresponding Rossby–Haurwitz solutions. To do this we make use of the wavespeed formula derived by Haurwitz [32]. The particular formula, restated here for reference, is given by

$$c = \frac{\kappa(3 + \kappa)\omega - 2\Omega}{(1 + \kappa)(2 + \kappa)} \quad (4.98)$$

which has been rewritten to reflect the naming conventions and variable names used in this work. To compare the two solution types we consider the primary physical

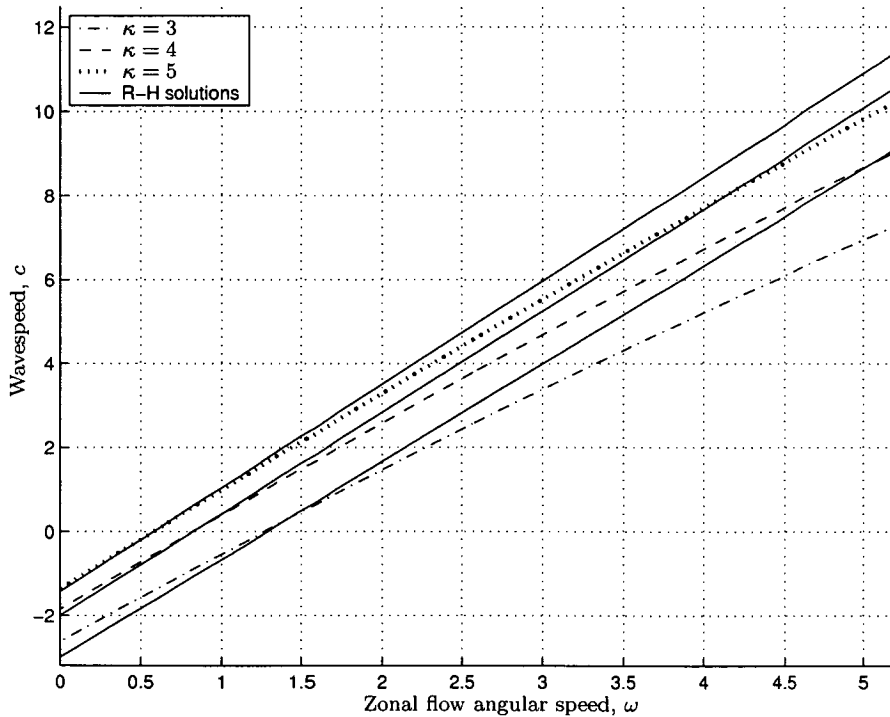


Figure 4.2: Comparison of compressible linearized and Rossby–Haurwitz solutions for $\kappa = 3, 4$ and 5 with $N = 100$.

eigenvalues for $\kappa = 3, 4$ and 5 with the equivalent Rossby–Haurwitz solutions over a reasonable range of allowable ω values. Figure 4.2 shows the results of this com-

parison, with the solid lines representing the equivalent Rossby–Haurwitz solution for $\kappa = 3$ to 5 from bottom to top respectively. In general one can conclude that the two models are in good broad agreement and we see that the behaviour of the compressible linearized solutions is not dissimilar to that of the incompressible linearized solutions, as shown in Figure 2.4 of Chapter 2. We also note that because the Haurwitz model has no provision for fixing the total mass M_b of the atmosphere, differences are to be expected between that model and the work presented here. The discrepancies are most noticeable for larger values of the parameter ω where the effect of the mass matching condition has greater influence on the solution.

Figures 4.3–4.5 present polar stereographic projections of the free-surface, density and pressure contours respectively. The scaling of the amplitude, via the linearization parameter ϵ , was chosen so that the free-surface height matched the non-dimensional height of the Rossby–Haurwitz wave at $(\eta, \phi) = (0, \pi/4)$. This is similar to the technique that was used to match the incompressible and Rossby–Haurwitz solutions in Section 2.6.3 of Chapter 2. The scaling is arbitrary and is only used here so that visual confirmation of the general wave structure can be made.

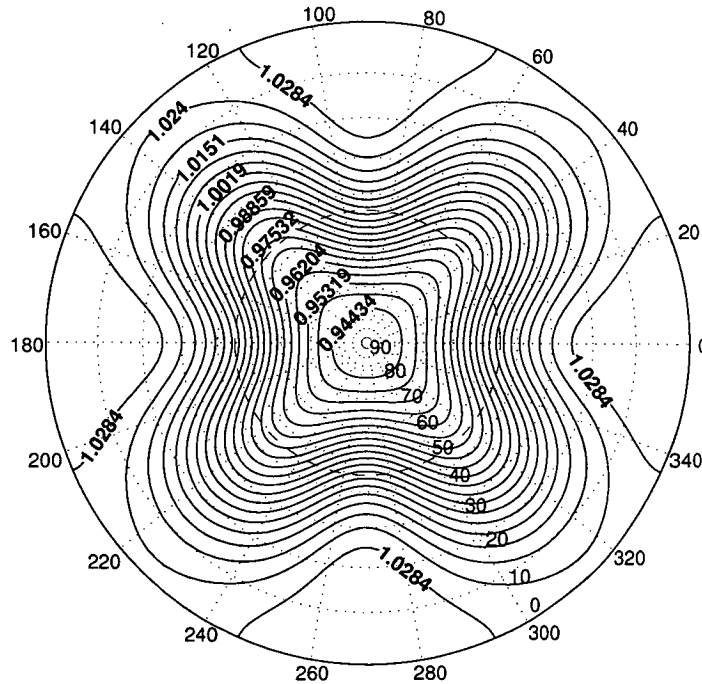


Figure 4.3: Compressible linearized free-surface contours for $\kappa = 4$ with $N = 100$.

It is evident that the compressible free-surface contours of Figure 4.3 are quite similar

in shape to those of the incompressible linearized theory (see Figure 2.5) and hence need no further comment. The density and pressure contours can be constructed once the free-surface shape is given, according to (4.64) and (4.65). Examination of the density contours in Figure 4.4 reveals that the fluctuation in density about the mean sea-level value of $\rho = 1$ is in reasonable agreement with that normally encountered in the Earth's atmosphere. Density values in Figure 4.4 range from approximately 85% to 110% of the mean sea-level value. Similar fluctuations are observed in the pressure field of Figure 4.5. Note also that the pressure and density contours are nearly parallel, so that the flow can be described as departing only slightly from that of barotropic flow.

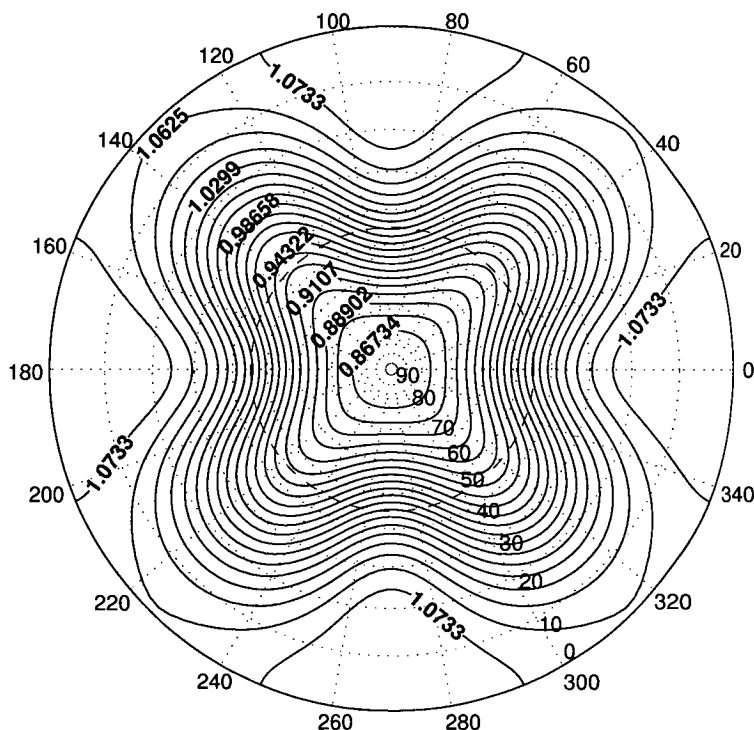


Figure 4.4: Compressible linearized density contours for $\kappa = 4$ with $N = 100$.

Figure 4.6 demonstrates the nature of the velocity vector field associated with the pressure field of Figure 4.5. The flow is observed to be predominantly geostrophic with the fluid streamlines essentially coinciding with the pressure contours. Additionally we have increasingly diminishing flow as we approach either pole, which converges to the required stagnation point when $\phi = \pm\pi/2$. The general nature of the fluid flow is directed in the same direction as the underlying zonal flow with the Rossby wave pattern moving relative to this mean fluid progression in an anti-

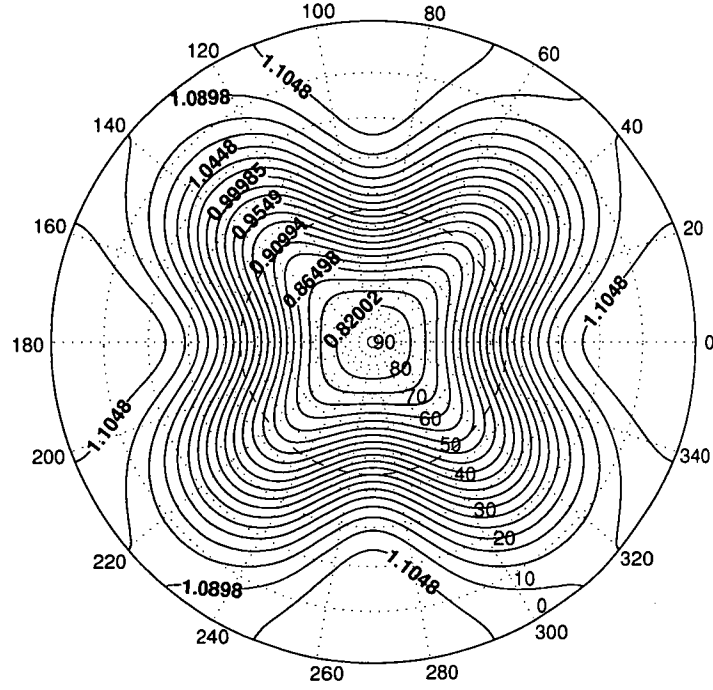


Figure 4.5: Compressible linearized pressure contours for $\kappa = 4$ with $N = 100$.

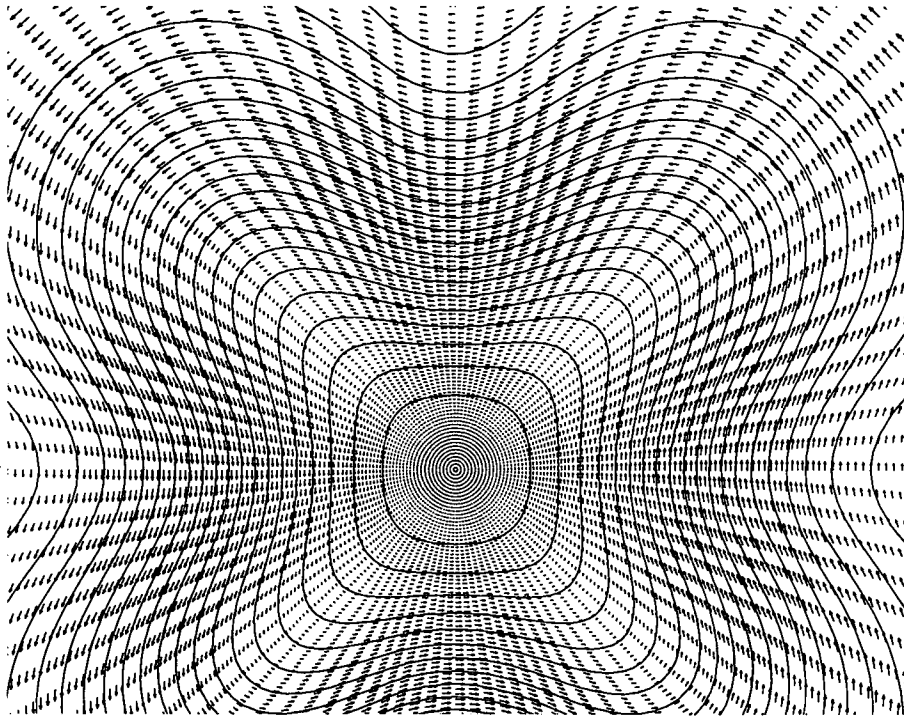


Figure 4.6: Compressible linearized pressure contours with corresponding velocity vector field for $\kappa = 4$ with $N = 100$

clockwise manner, as expected for this particular map projection of the Northern Hemisphere.

CHAPTER 5

COMPRESSIBLE NONLINEAR SHALLOW ATMOSPHERE MODEL

In this chapter we consider the solution of the full nonlinear dynamical problem for compressible flow on a rotating sphere with a free-surface. The linearized results of Chapter 4 are extended, providing detailed information on how the nonlinear progressive wavespeed and amplitude are related. The techniques used to solve the mathematical problem are similar to those used to solve the nonlinear incompressible dynamics problem in Chapter 3, and as such an abridged version is presented here with the main focus being on the results, which are shown to differ in some key ways.

5.1 Problem Specification

5.1.1 Conservation Equations

The equations of motion to be used are those derived in Chapter 4 for conservation of mass and momentum in the rotating compressible shallow atmosphere system. In dimensionless variables the three conservation equations are given as:

mass

$$(u_\lambda - \text{Sr } c \cos \phi) \frac{\partial h}{\partial \eta} + u_\phi \cos \phi \frac{\partial h}{\partial \phi} + \frac{(\gamma - 1)}{\gamma} h \left[\frac{\partial u_\lambda}{\partial \eta} + \cos \phi \frac{\partial u_\phi}{\partial \phi} - u_\phi \sin \phi \right] = 0. \quad (5.1)$$

λ momentum

$$(u_\lambda - \text{Sr } c \cos \phi) \frac{\partial u_\lambda}{\partial \eta} + u_\phi \cos \phi \frac{\partial u_\lambda}{\partial \phi} - \left(\frac{\cos \phi}{\text{Ro}} + u_\lambda \right) u_\phi \sin \phi + \frac{1}{\text{Fr}^2} \frac{\partial h}{\partial \eta} = 0, \quad (5.2)$$

 ϕ momentum

$$(u_\lambda - \text{Sr } c \cos \phi) \frac{\partial u_\phi}{\partial \eta} + u_\phi \cos \phi \frac{\partial u_\phi}{\partial \phi} + \left(\frac{\cos \phi}{\text{Ro}} + u_\lambda \right) u_\lambda \sin \phi + \frac{\cos \phi}{\text{Fr}^2} \frac{\partial h}{\partial \phi} = 0. \quad (5.3)$$

The particular form of (5.1) is the result of specifying that the density and pressure on the free-surface are zero, as in Section 4.2.2 of the previous chapter. The specific forms for the thermodynamic variables of density and pressure are given by

$$\rho(\hat{r}, \eta, \phi) = \left[\frac{(\gamma - 1)}{\gamma} \left(\frac{\text{M}}{\text{Fr}} \right)^2 \left(\hat{a} + \hat{h}(\eta, \phi) - \hat{r} \right) \right]^{\frac{1}{\gamma-1}} \quad (5.4)$$

and

$$p(\hat{r}, \eta, \phi) = \left[\frac{(\gamma - 1)}{\gamma} \left(\frac{\text{M}}{\text{Fr}} \right)^2 \left(\hat{a} + \hat{h}(\eta, \phi) - \hat{r} \right) \right]^{\frac{\gamma}{\gamma-1}}, \quad (5.5)$$

where \hat{a} is the dimensionless form of the sphere's radius.

5.1.2 Mass Specification

To enable comparison between solutions of the dynamical system given by (5.1)–(5.3) we again use a mass specification condition, so that the total mass of the atmosphere is held constant for all solutions calculated. We define a base system mass denoted M_b , which is given by (4.94) of Section 4.5.2. For a general progressive Rossby wave of arbitrary free-surface height $h(\eta, \phi)$, the total mass of fluid contained between the surface of the sphere and the free-surface is given by

$$M_{nl} = \int_0^{2\pi} \int_{-\pi/2}^{\pi/2} \int_{\hat{a}}^{\hat{a}+h(\eta, \phi)} \rho(\hat{r}, \phi) \hat{r}^2 \cos \phi \, d\hat{r} d\phi d\eta. \quad (5.6)$$

Defining

$$\beta = \frac{(\gamma - 1)}{\gamma} \left(\frac{\text{M}}{\text{Fr}} \right)^2, \quad (5.7)$$

$$f_3(\eta, \phi) = \beta(\hat{a} + h(\eta, \phi)), \quad (5.8)$$

we can write the integral given by (5.6) in the form

$$M_{nl} = \frac{4\kappa(\gamma - 1)\beta^{\frac{3-2\gamma}{\gamma-1}}}{\gamma(2\gamma - 1)(3\gamma - 2)} \times \int_0^{\pi/\kappa} \int_0^{\pi/2} h^{\frac{\gamma}{\gamma-1}} [2f_3^2(\gamma - 1)^2 + 2\beta f_3(\gamma - 1)\gamma\hat{a} + \beta^2\gamma(2\gamma - 1)\hat{a}^2] \cos\phi \, d\phi d\eta. \quad (5.9)$$

The nonlinear equation for mass conservation is then given by

$$1 - \frac{M_{nl}}{M_b} = 0. \quad (5.10)$$

The complete specification of a nonlinear atmospheric progressive Rossby wave in this compressible model consists of solving (5.1)–(5.3) and (5.10) subject to some condition defining the amplitude of the wave.

5.2 Numerical Solution Method

5.2.1 Series Solution and Algorithm

Solutions of the full nonlinear dynamics given in the previous section are sought using Fourier series with similar symmetry conditions imposed on the field variables as in Section 4.4 of Chapter 4. Taking these symmetry and boundary conditions into account, the series for the nonlinear problem, using longitudinal truncation M and latitudinal truncation N , are given by:

$$u_\lambda(\eta, \phi) = \omega \cos\phi + \sum_{m=1}^M \sum_{n=1}^N P_{m,n} \cos(\kappa m \eta) \cos((2n - 1)\phi), \quad (5.11)$$

$$u_\phi(\eta, \phi) = \sum_{m=1}^M \sum_{n=1}^N Q_{m,n} \sin(\kappa m \eta) \sin(2n\phi), \quad (5.12)$$

$$h(\eta, \phi) = \sum_{n=0}^N H_{0,n} \cos(2n\phi) + \sum_{m=1}^{M-1} \sum_{n=1}^N H_{m,n} \cos(\kappa m \eta) (-1)^n [\cos(2n\phi) + \cos(2(n - 1)\phi)]. \quad (5.13)$$

Here, (5.13) again uses basis recombination to satisfy boundary conditions at the poles. The nonlinear series (5.11) for u_λ now contains the primary zonal flow velocity component. Instead of specifying the polar free-surface height we replace h_o with

the single summation term in (5.13) to allow the polar height to be determined from the output of the model.

The solution is forced by either parameterizing the amplitude, denoted \mathcal{A} , in terms of one of the unknown coefficients, or specifying the wavespeed c . To this end $H_{1,1}$, in the series for $h(\eta, \phi)$, or the wavespeed c is fixed prior to computation, thus removing one of the unknowns from the problem. The majority of computations were performed by specifying $H_{1,1}$, and the second technique of specifying c was reserved for cases where two or more solutions were possible with the same amplitude.

The general solution process consists of finding the set of coefficients $H_{m,n}$, $P_{m,n}$, $Q_{m,n}$ and wavespeed c that make the series (5.11)–(5.13) a solution of the dynamical system described by (5.1)–(5.3) and (5.10). The technique chosen to accomplish this task for the current work was the pseudospectral technique of collocation in which we require the residuals, obtained by substituting the series into the governing equations, to be zero at every point on a mesh constructed from a finite number of collocation points in the flow field. This is exactly the same technique that was used to solve the incompressible nonlinear dynamics problem of Chapter 3 and will not be further expanded upon here.

For the collocation points in ϕ we restrict computation to the Northern hemisphere since the solution has specific symmetry relative to the equator. In addition, strictly internal points from the domain are chosen, since the specific choice of the basis functions for each series imposes boundary conditions at both $\phi = 0$ and $\phi = \pm\pi/2$. Defining

$$\Delta\phi = \frac{\pi}{2(N+1)} \quad (5.14)$$

to be the inter-grid point distance in the ϕ direction, the N equally-spaced ϕ -grid points are given by

$$\phi_i = i\Delta\phi, \quad \text{for } i = 1, 2, \dots, N. \quad (5.15)$$

The collocation points in η can be obtained in a similar manner; however, since we have stipulated a dependence on the wavenumber κ we are only free to choose collocation points from $\eta \in [0, \pi/\kappa)$ to avoid linearly dependent rows in the resulting Jacobian matrix. This also accounts for the fact that the Rossby wave is symmetric about its mid-line $\eta = \pi/\kappa$. Defining

$$\Delta\eta = \frac{\pi}{M\kappa} \quad (5.16)$$

to be the inter-grid point distance in the η direction, the M equally spaced η -grid points are given by

$$\eta_j = (j - 1)\Delta\eta, \quad \text{for } j = 1, 2, \dots, M. \quad (5.17)$$

The set of points taken from all possible (η_j, ϕ_i) pairs constitutes the collocation mesh to be used in the numerical solution.

Evaluating each of the three governing dynamical equations (5.1)–(5.3) at each of the collocation mesh points and computing the mass specification condition (5.10) yields a vector of residuals, denoted $\mathbf{E}(\mathbf{a})$, of length $3MN + 1$, where \mathbf{a} is a vector comprised of the wavespeed (if it is not the forcing term) and set of unknown coefficients. A damped Newton–Raphson method, as in Section 3.2.2 of Chapter 3, is then used to solve the resulting algebraic system, which has the general form

$$\mathbf{E}(\mathbf{a}) = \mathbf{0}. \quad (5.18)$$

The Jacobian matrix, which is required to compute the updating vector in the Newton–Raphson method, is calculated analytically since the Jacobian elements are, in general, easily determined. Additionally, the total residual error, which is used in assessing the convergence of a solution, is computed using the L^1 norm.

The starting guess at the set of unknowns \mathbf{a} in the Newton–Raphson method is initially determined from the equivalent small amplitude linearized solution given in Section 4.4 of the previous chapter. Once a small amplitude nonlinear solution has been determined it is then used as the basis for the next solution to be computed but with a slightly modified value of either c or $H_{1,1}$, depending on the type of forcing. This bootstrapping procedure forms the basis of mapping the wavespeed versus amplitude relationship incrementally.

Computational efficiency is achieved by caching each of the basis functions and their derivatives with respect to η and ϕ at each of the collocation mesh points; this approach reduces the computational overhead incurred by repeated function calls to the trigonometric functions. The integral appearing in (5.9) is evaluated using numerical quadrature. The particular algorithm used is that of adaptive Lobatto quadrature, with Kronrod extension of the Gauss–Lobatto formula, as detailed in Gander & Gautschi [27]. The majority of computations were performed on two separate computers, the first being an AMD Athlon(tm) XP 1800+ processor clocked at 1.54 GHz with 512 MB of physical memory clocked at 266 MHz, the second being

an Athlon(tm) XP 2800+ processor clocked at 2.08 GHz with 1 GB of dual channel physical memory clocked at 333 MHz.

5.2.2 Amplitude Measurement

In order to investigate the relationship between the progressive Rossby wavespeed and amplitude, we require a means of defining the amplitude \mathcal{A} of a particular Rossby wave. For a simple periodic wave, the amplitude can be defined as the maximum deviation from the mean position to an extreme point. The problem of measuring Rossby wave amplitude horizontally on a sphere is somewhat more complicated and arbitrary, however. Due to the multitude of wave shapes that are possible there are an infinite number of mean states about which we can measure wave deviation. We must therefore decide which one is appropriate to use. Because Rossby wave activity is predominantly associated with the mid-latitude regions and also because $\phi = \pm\pi/4$ represents the mid-point between the equator and either pole, we choose the mean reference level as the latitude circle located 45° from the equator in either hemisphere.

In this context, progressive Rossby waves are perturbations from a base zonal Westerly flow, for which the height contours are simply circles of constant ϕ . The unperturbed free-surface height contours at $\phi = \pm\pi/4$ are taken here as the base level, against which Rossby wave amplitudes are measured. This is identical with the definition of amplitude given in Section 3.4.1 of Chapter 3.

We again observe that the amplitude will not be the same in both the equator-ward and pole-ward directions, and the difference between the two will increase as the overall wave amplitude grows. Thus to record \mathcal{A} effectively we measure both the equator-ward and pole-ward deflections, again denoted \mathcal{A}_e and \mathcal{A}_p respectively. Associated with these separate amplitudes we define a simple averaged amplitude, the mean of the two values, to be

$$\mathcal{A}_{ave} = \frac{\mathcal{A}_e + \mathcal{A}_p}{2}. \quad (5.19)$$

It is important to emphasize that these definitions of amplitude are somewhat arbitrary, although they are a useful way of quantifying transverse amplitudes on a spherical surface.

5.3 Solution and Results

5.3.1 Model parameters

The parameters and constants for the model are again chosen to approximate those of the Earth, as in Section 4.5.1 of the previous chapter. Specifically, the parameters a , Ω and g , as well as the four reference scales v_{ref} , c_{ref} , p_{ref} and ρ_{ref} are given by (4.81)–(4.87) respectively. Additionally, the reference height level is defined by (4.89) and the ratio of specific heats is given as $\gamma = 1.4$.

For the dimensionless zonal flow parameter ω we use two specific values; these are the same values used in the incompressible nonlinear model of Section 3.4.2. The first value is consistent with the angular speed ω used in the test set proposed by Williamson et al. [87]. The second value, chosen to be 80% of the first value, provides a slower value for the super rotation rate. In dimensionless form they are given by

$$\omega_1 = 1.25, \tag{5.20}$$

$$\omega_2 = 1.0. \tag{5.21}$$

5.3.2 Results for $\kappa = 4$, $\omega = 1.25$

Figure 5.1 shows the wavespeed c computed for $\kappa = 4$ and $\omega = 1.25$, for each of the three measures of amplitude \mathcal{A}_e , \mathcal{A}_p and \mathcal{A}_{ave} . The truncation levels are $M = 15$ and $N = 15$ and the error tolerance on the L^1 norm of the residual vector was set at 10^{-12} . The solution curves are comprised of a total of 147 converged results; however, the majority of computations were performed for larger values of the amplitude so as to ascertain the detailed behaviour towards the right end of the graph.

The general characteristics of the solution are quite similar to those of the equivalent incompressible model with similar parameters (see Section 3.4.3). For small amplitude the value of the wavespeed c is appropriately approximated by the linearized solution, which is indicated in the figure. Additionally, as the amplitude increases so does the wavespeed, which is to be expected.

The main new feature of these results, as opposed to the incompressible results referred to previously, is the addition of a new branch, labeled branch 2 in Figure 5.1. The small hook-shaped branch 2 was found by first calculating the solution curve

at a lower truncation level of $M = N = 10$ and then bootstrapping these results to solutions with more coefficients at a higher truncation level. Only a narrow region of convergence was found; however, the solutions contained along this small branch were all found to converge within the required error tolerance norm of 10^{-12} .

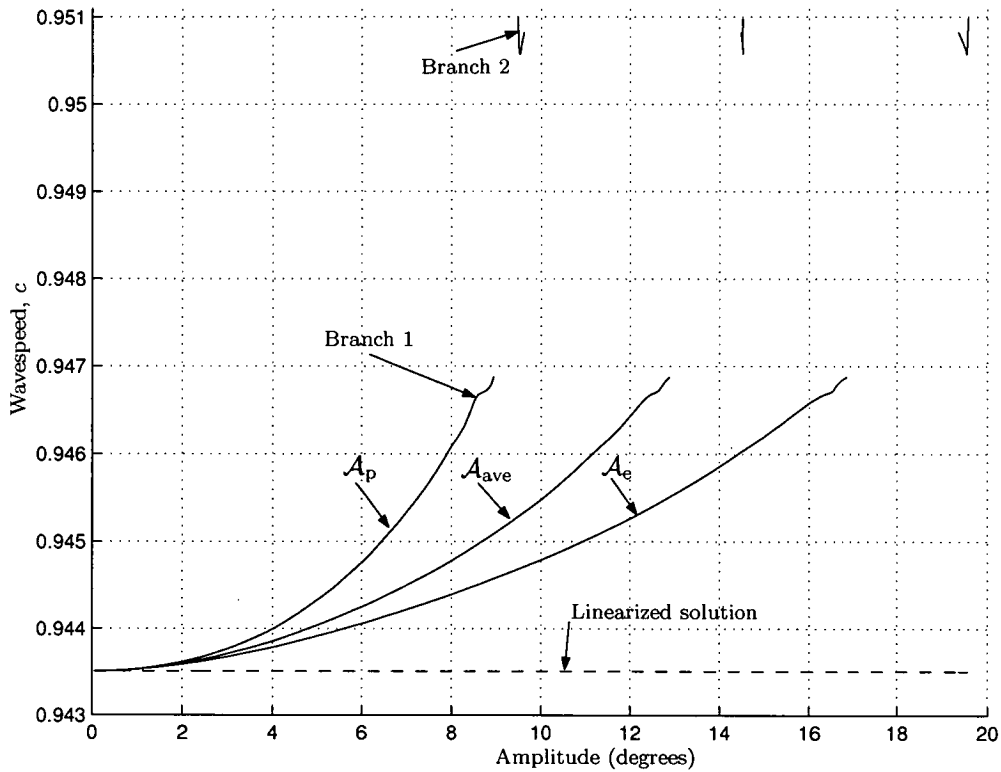


Figure 5.1: Compressible wavespeed versus Amplitude for $\kappa = 4$ and $\omega = 1.25$

The separation of the solution curve into two branches again indicates the presence of a resonant interaction. Attempts were made to find solutions for values of the wavespeed inside the gap between branches 1 and 2 but results indicated that no such solutions exist, or at least are not possible to find using our numerical method. A slight bending-over of the curve at the right end of branch 1 is observed. Identical behaviour was encountered in the incompressible model. Thus it seems likely that the incompressible model might also harbour an additional branch, beyond branch 1, with higher wavespeeds and larger amplitudes, as was conjectured previously in Section 3.4.3.

The free-surface contours at the limiting upper end of branch 2 are shown in Figure 5.2. To the extent that the difference in the amplitude of solutions lying on the right end of branch 1 and those lying on all of branch 2 is only slight, min-

imal qualitative difference is seen in the free-surface contours on both branches. Apart from the fact that solutions on branch 2 have greater wavespeeds, which is the main difference between them, a further distinguishing characteristic between the two branches is the formation of a flat-crested wave profile in the vicinity of $\phi = \pm\pi/4$ for solutions on the second branch. This shape is visible in Figure 5.2 as a flat-crested wave for the fifth contour level from the pole.

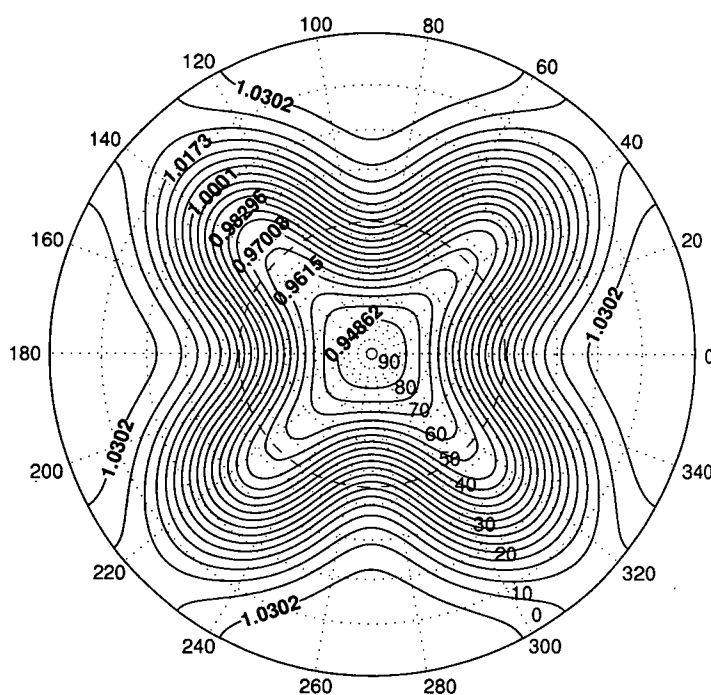


Figure 5.2: Compressible free-surface contours at end of branch 2 for $\kappa = 4$, $\omega = 1.25$.

Figure 5.3 shows this flat-crested region in detail, along with the computed velocity vector field. It is seen that this local region of flatness is also reflected in the wind vector. The cause of this feature is unknown but it appears that it would impose a limiting topological constraint for solutions on this branch. It is possible that a third branch exists beyond the second on which solutions would have the property of small localised circulation or ripples in the vicinity of the wave crest. This behaviour would be similar to that first encountered by Wilton [88]. Attempts were made to find more solution branches using bootstrapping techniques mentioned previously; in all cases no converged solutions were computed with the current numerical method.

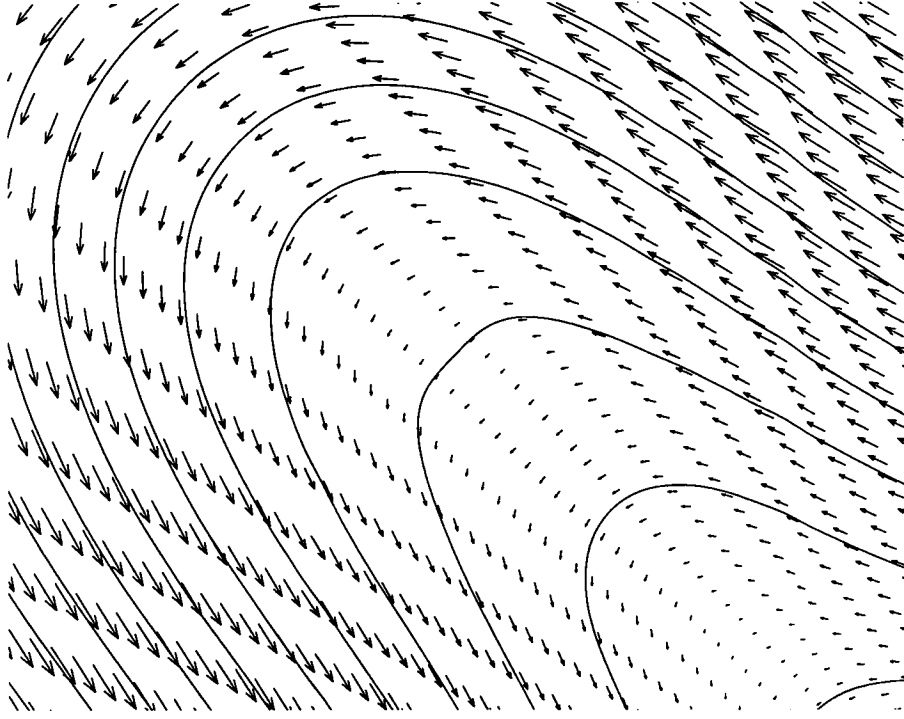


Figure 5.3: Compressible free-surface contours with velocity field at end of branch 2 for $\kappa = 4$, $\omega = 1.25$.

5.3.3 Results for $\kappa = 4$, $\omega = 1.0$

Figure 5.4 gives the computed wavespeeds from 197 individual computations using $\kappa = 4$ and $\omega = 1.0$. Results were obtained by requiring the L^1 norm of the residual vector to be less than 10^{-12} . The truncation levels were again set at $M = N = 15$ with little difference observed between solutions obtained with a truncation level of $M = N = 10$. Agreement between the nonlinear solution for small amplitude and the linearized result is again observed to be excellent, with the linearization only failing to provide a good estimate of the wavespeed as the amplitude is increased.

A distinct discontinuous jump is observed in the solution curve, indicating nonlinear resonance. Of particular note is the peaked, pinched region in the middle of branch 2, which is not present in the equivalent incompressible solution curve (see Figure 3.4). It is interesting to observe, however, that the incompressible model has a resonance located between branches 2 and 3 and that the qualitative difference between these two branches was minimal. Thus the peaked region in the middle of branch 2 for the compressible model could be seen as a similar phenomenon, except that for the

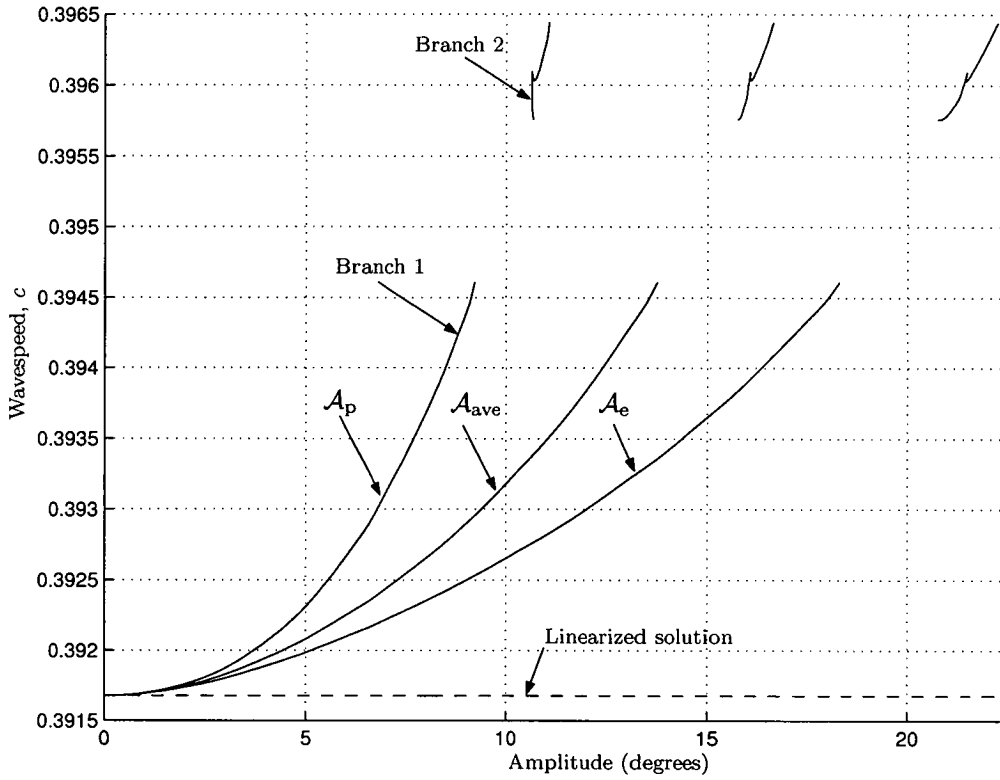


Figure 5.4: Compressible wavespeed versus amplitude for $\kappa = 4$ and $\omega = 1.0$

compressible dynamics the behaviour is damped, so that the effect of the resonance on the solution curve is limited locally.

It is also possible that the segment of the solution curve that has been labelled here as branch 2 is in fact two separate branches. To test whether this claim could be true, the solutions on branch 2 were calculated using a very small amplitude increase each time; in total, over 70 points comprise the computed branch 2 solution. Although the local peaked region was encountered, no break in the continuity of the numerical solution occurred, in contrast to the similar case for the incompressible dynamics in which a distinct gap was detected. It therefore seems reasonable to conclude that Branch 2 really is a continuous branch containing a damped resonance, on the basis of the careful numerical solution.

The main distinguishing difference between solutions on branches 1 and 2 can again be exposed by examining the associated velocity vector fields. As in the equivalent incompressible case of Section 3.4.4, it is observed that at no point on branch 1 does the solution contain any stagnation points other than at the poles. For solutions on

branch 2, however, there is again the presence of stagnation points on the equator so that the fluid flow is counter to the direction of Rossby wave propagation at certain points in the flow. Because this behaviour is essentially the same as that depicted in Figure 3.8 of Chapter 3, no further illustration is given here. It seems reasonable to conjecture that a smooth transition from solutions on branch 1 to solutions on branch 2 is not possible for pure travelling waves and that full nonlinear time dependence is required to study how a wave would make the transition from branch 1 to branch 2, as amplitude is increased. This, in part, explains the existence of the nonlinear resonance between the two distinct branches of the solution curve.

5.3.4 Results for $\kappa = 5$, $\omega = 1.25$

We now examine results obtained for $\kappa = 5$ and $\omega = 1.25$. A total of 262 converged

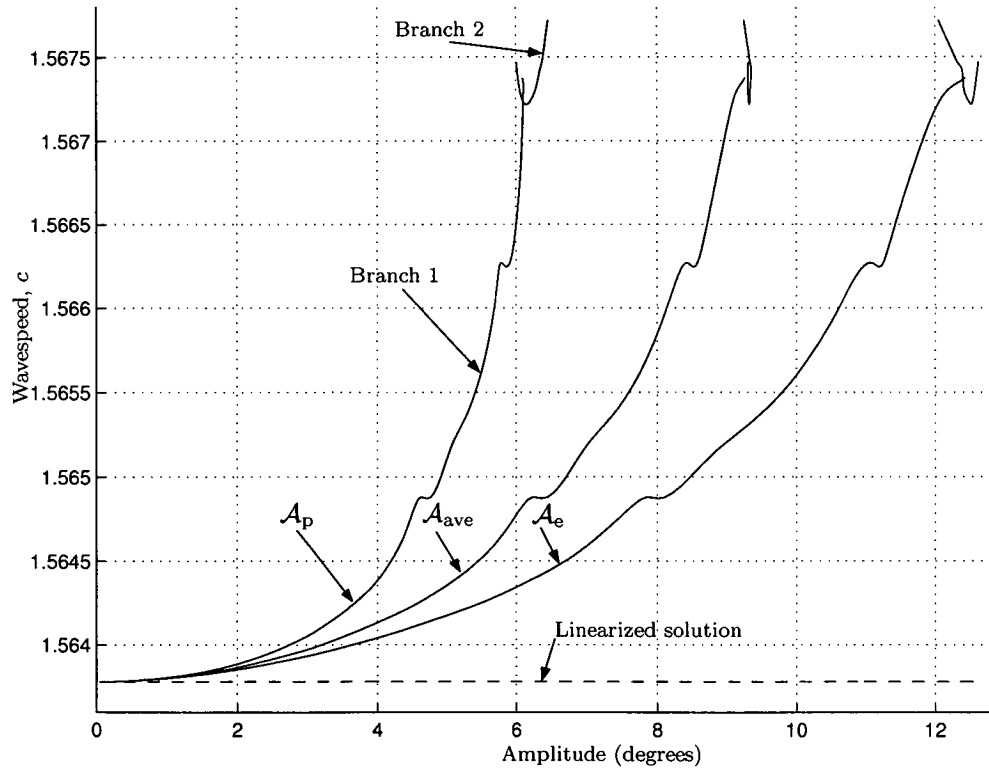


Figure 5.5: Compressible wavespeed versus Amplitude for $\kappa = 5$ and $\omega = 1.25$

solutions were computed and used to plot the c versus \mathcal{A} relationship in Figure 5.5. Note that more points were required here than for previous results because of the detailed structure of the solution curve. Results were obtained with truncation levels of $M = N = 15$ and the error tolerance on the L^1 norm of the residual vector was

set at 10^{-12} .

The general nature of the graph is seen to be quite similar to that of the incompressible equivalent given in Figure 3.9, with the linearized solution being a good approximation for small amplitude. However, note the existence of two localised cubic structures on branch 1, as opposed to the single isolated structure for the incompressible case. It was proposed in Section 3.4.5 that this behaviour was representative of a type of damped resonance in which energy exchange between certain wavelengths is taking place in such a manner as to increase the overall amplitude while at the same time reducing the wavespeed. To understand the exact mechanism behind this damping would require, at the very least, careful analytical work beyond the scope of this numerical study.

Despite this localised reversal of the general trend of the graph, no obvious distinguishing features are visible when the free-surface contours and velocity vector field are examined in the vicinity of these solution regions. Two separate solution branches were again found to exist towards the upper end of the curve when the limiting amplitude-wavespeed combination was approached. However, the qualitative difference between the two branches is minimal and it may be that this second branch is physically unstable, as discussed in Section 3.4.5 of Chapter 2, or that a greater truncation level is required to resolve the nature of this branch owing to slow convergence of the Fourier series.

5.3.5 Results for $\kappa = 5$, $\omega = 1.0$

In this final section we present results for the computed wavespeeds with parameter values given by $\kappa = 5$ and $\omega = 1.0$, as represented in Figure 5.6. The truncation levels were again set at $M = N = 15$ and the error tolerance on the L^1 norm of the residual vector was set at 10^{-12} , leading to average individual residual errors of the order of 10^{-15} or less. A total of 155 points comprise the makeup of the solution curves. For small amplitudes, the wavespeed is aptly given by the linearized result, as indicated in the figure.

One of the localised cubic structures, seen in the previous set of results, is evident here also, albeit on a much smaller scale, in the vicinity of $c = 0.9852$. This behaviour is similar in general to the incompressible results of Section 3.4.6. The main new feature is the introduction of another solution branch as a result of the

compressible dynamics. Despite the pinched nature of branch 2, the continuity of the solution along this branch was numerically established by approximately 60 individually converged solutions that failed to exhibit any discontinuous behaviour along the branch. We must therefore conclude, on the basis of numerical evidence, that branch 2 is indeed a continuous solution curve and not two distinct adjacent branches.

The behaviour of the solution on the second branch again seems to be influenced by some type of damping mechanism. It is not possible to expose the physical nature of this damping mechanism with numerical methods alone. The qualitative difference in the flow fields and free-surface contours for solutions on branch 1 and 2 is quite small, and at no point in the velocity fields of either branch does the fluid flow counter to the direction of progressive Rossby wave motion. Thus no additional stagnation points in the flow field are present. This agrees with the general properties of the equivalent incompressible dynamics of Section 3.4.6 of Chapter 3.

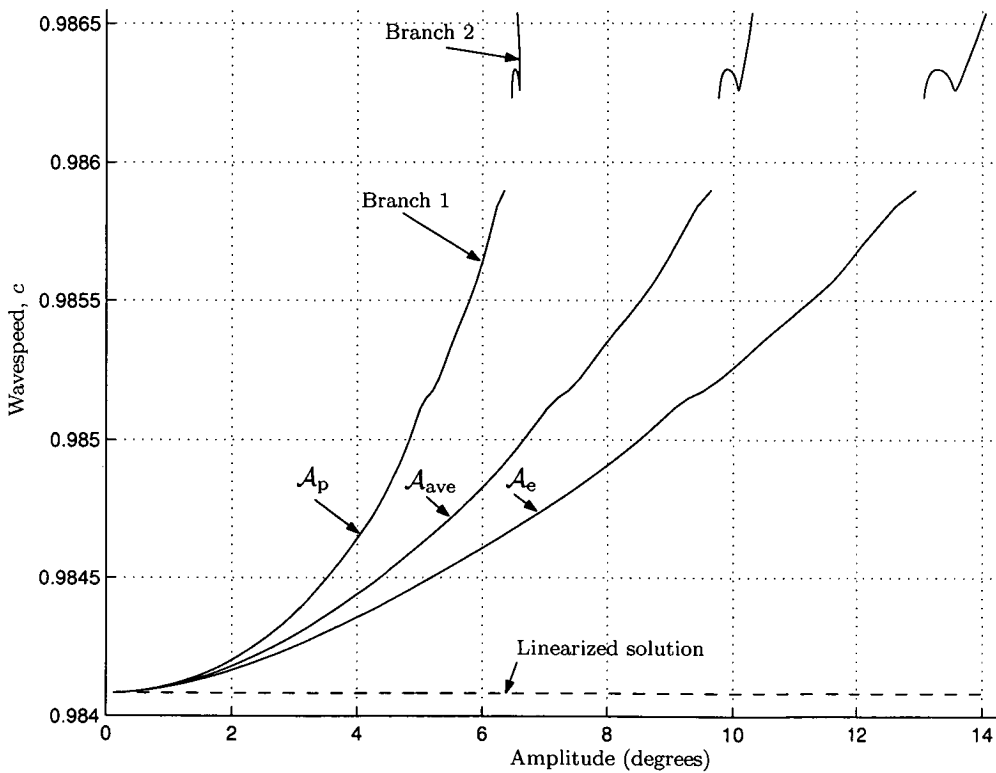


Figure 5.6: Compressible wavespeed versus Amplitude for $\kappa = 5$ and $\omega = 1.0$

5.4 Closing Remarks

In this chapter we solved the complete nonlinear equations governing compressible shallow atmosphere free-surface flow. The results obtained were similar to those from the incompressible model with similar parameters; however, small key differences were observed that are attributable to the compressibility of the dynamics. Specifically, it was shown that for all four cases examined, at least two distinct solution branches were found in each instance. The presence of compressibility was observed to damp some instances of resonant behaviour that were encountered in the incompressible model. The cut-off low pressure cells that were computed for $\kappa = 4$ and $\omega = 1.0$ in the incompressible case were not observed in the compressible model. However, it is suspected that they do still exist and that our numerical scheme was not capable of finding them due to the sensitivity of Newton's method. Attempts to confirm the existence of these cells have thus far been unsuccessful. It is again highly unlikely that numerical methods alone can answer this existence question, and that additional analytical methods may have to be employed. Such an analysis is beyond the scope of the present investigation.

CHAPTER 6

CONCLUSION AND CLOSING REMARKS

6.1 Discussion and Application to Meteorology

In this thesis we have presented a detailed picture of how the effects of nonlinearity influence the relationship existing between wavespeed and amplitude for progressive Rossby waves. The techniques utilised have uncovered feature-rich dynamical properties of solutions of the shallow atmosphere equations on a rotating sphere. In particular it was shown that nonlinear resonance plays an important and dominant role for waves with large amplitudes. The effect of resonance was observed to separate solutions of the system into disjoint regions, with similar solutions lying on the same solution branch in wavespeed–amplitude space.

Two specific models of the atmosphere were used: an incompressible and a compressible model. For the incompressible dynamics it was shown that, for slowly propagating progressive waves with longitudinal wavenumber $\kappa = 4$, if the amplitude forcing became large enough it was possible for the flow to develop localised low-pressure cells in the mid-latitude regions. These types of extreme amplitude solutions were accompanied by stagnation points in the flow field at locations other than the poles. In general it was observed that for these highly nonlinear waveforms the lower polar free-surface heights, and hence pressures, and also the higher equatorial free-surface elevations, tended to be grossly distorted so that it was common for contours originating near the equator or pole to be deformed towards regions well in excess of the mid-latitudes.

In the Earth's atmosphere, Rossby waves are frequently observed by filtering out localised small scale effects and concentrating on the 500 mb height field contours, so that the effects of the planetary boundary layer, and hence friction, are minimal. Using this technique it is possible to expose the large-scale structure of the atmosphere. Since the late 1970's there has been considerable effort expended by meteorologists in an attempt to explain the large-scale process of atmospheric blocking (see the critical review article by Lindzen [51]). In its simplest form, blocking is either the existence of a stationary high pressure cell that persists in the mid-latitudes where westerly flow would normally be observed, or a ridge of high pressure that extends polewards from the tropics and influences the mid-latitude flow characteristics. Usually the formation of a block tends to be associated with stationary planetary waves.

In the investigation conducted in this thesis, it was found that the most extreme case of large amplitude waves was for slowly moving progressive Rossby waves with the parameters $\kappa = 4$ and $\omega = 1.0$. The linearized wavespeed associated with this specific parameter configuration was $c \approx 0.395$. Thus for only a slightly smaller value of the zonal flow parameter ω , the linearized and associated nonlinear wavespeeds would be very close to zero, so that the Rossby wave would be approximately stationary with respect to the surface of the Earth. We conjecture that the particular nature of the wavespeed–amplitude relationship for stationary Rossby waves would not be dissimilar to that computed for the case $\kappa = 4$ and $\omega = 1.0$. If this is so it would imply the existence of highly distorted nearly stationary Rossby waves containing high pressure ridges extending polewards from the equator, with cut-off low pressure cells in the mid-latitudes. This type of atmospheric configuration could be seen as being crucial to the instigation of a blocking event, with subsequent development of cut-off high-pressure cells near the mid-latitudes when full time dependence is included in the model.

This argument is, in general, supported by the work of Austin [5] who found that the splitting of westerly winds by blocking is attributable to interference, or resonance, between planetary waves with very large amplitudes. In this conjecture, however, nothing is implied as to how the dynamical system moves from one solution branch to the next. Nor is it expected that all the solution branches would be physically stable. Charney & DeVore [13] and Charney, Shukla & Mo [14] have conducted studies in an attempt to ascertain the effect of topography and thermal forcing on blocking in

the atmosphere and have shown the existence of multiple equilibrium states, some of which exhibit blocking phenomena. It is thus possible that through various forcing mechanisms, such as the effects of topography and thermal heating/cooling, the atmosphere can pass from one equilibrium state to another. If this proves to be true then the highly nonlinear feature-rich solutions calculated in this work would support the idea that blocking is primarily a dynamical state which is accessible through appropriate forcing of the atmospheric system.

6.2 Future work and Closing Remarks

The aim of this thesis was to investigate numerically nonlinear progressive Rossby wave behaviour. The analysis techniques utilised have uncovered some of the defining features of shallow atmosphere free-surface flow with progressive Rossby waves; however, many questions still remain unanswered. Because of the complexity of the governing equations, and the associated sensitivity of Newton's method, it is highly possible that our numerical solution method did not find all possible solution branches for the particular parameter configurations used. It would thus be desirable to conduct analytical research in an attempt to support the numerical findings contained in this thesis. Additionally, an analytical study would provide insight into the proposed existence of additional solution branches that were conjectured at various stages throughout this thesis. However, because of the sheer complexity of the dynamical equations involved, it is more than likely that such an analytical approach would be severely limited in scope unless significant approximations and idealizations were made.

In this work nothing has been said of the stability of the solutions computed. It seems highly likely that solutions along the first branch of each wavespeed–amplitude curve would be stable, and for small amplitude waves an analysis of the linearized system would more than likely suffice to ascertain the Lyapunov stability of the system. The reasoning behind this statement stems from the fact that Rossby waves are frequently observed in the atmosphere and so must form an integral part of its stable composition. The stability of the highly nonlinear waves computed with very large amplitudes would require special attention again. It would be desirable to know whether or not the largest flow computed for $\kappa = 4$ and $\omega = 1$, the flow containing cut-off low-pressure cells, is stable, as this would have consequences

for the stability of blocking formations, as discussed previously. Additionally, the inclusion of topography and temperature forcing in this analysis would be of great benefit.

This work has shown the sensitive dependence of progressive Rossby-wave solutions upon the zonal flow speed ω . Ideally, a complete study of the entire parameter region $0 < \omega < \omega_u$ would reveal the complete dynamical behaviour of large amplitude progressive Rossby waves, where ω_u is the maximum permissible angular speed, limited by the requirement that the atmosphere have some positive depth. Of course, such a massive numerical study is not achievable. It may be the case that analytical techniques might reveal further dynamical behaviour, although that is beyond the scope of the present work.

APPENDIX A

EVALUATION OF VOLUME SPECIFICATION JACOBIAN ELEMENTS

The Jacobian elements for the incompressible volume specification equation described in equation (3.31) can be further simplified by noting that the integral

$$\frac{\partial f_4}{\partial H_{i,j}} = -\frac{4\kappa}{V_z} \int_0^{\pi/\kappa} \int_0^{\pi/2} [h^2 + \hat{a}^2 + 2\hat{a}h] \frac{\partial h}{\partial H_{i,j}} \cos \phi \, d\phi \, d\eta \quad (\text{A.1})$$

can be split into three separate integrals so that

$$\begin{aligned} \frac{\partial f_4}{\partial H_{i,j}} &= -\frac{4\kappa \hat{a}^2}{V_z} \int_0^{\pi/\kappa} \int_0^{\pi/2} \frac{\partial h}{\partial H_{i,j}} \cos \phi \, d\phi \, d\eta - \frac{8\kappa \hat{a}}{V_z} \int_0^{\pi/\kappa} \int_0^{\pi/2} h \frac{\partial h}{\partial H_{i,j}} \cos \phi \, d\phi \, d\eta \\ &\quad - \frac{4\kappa}{V_z} \int_0^{\pi/\kappa} \int_0^{\pi/2} h^2 \frac{\partial h}{\partial H_{i,j}} \cos \phi \, d\phi \, d\eta \\ &= -\frac{4\kappa \hat{a}^2}{V_z} I_1 - \frac{8\kappa \hat{a}}{V_z} I_2 - \frac{4\kappa}{V_z} I_3. \end{aligned} \quad (\text{A.2})$$

Integrals I_1 and I_2 can be worked out analytically with the aid of (3.32). When $i = 0$ we have

$$\begin{aligned} I_1 &= \int_0^{\pi/\kappa} \int_0^{\pi/2} \cos(2j\phi) \cos \phi \, d\phi \, d\eta \\ &= -\frac{\pi(-1)^j}{(4j^2 - 1)\kappa} \quad , j = 0, \dots, N, \end{aligned} \quad (\text{A.3})$$

and for $i \geq 1$ we obtain

$$\begin{aligned} I_1 &= \int_0^{\pi/\kappa} \int_0^{\pi/2} \cos(\kappa i \eta) (-1)^j [\cos(2j\phi) + \cos(2(j-1)\phi)] \cos \phi d\phi d\eta \\ &= 0, \forall j. \end{aligned} \quad (\text{A.4})$$

Similarly for I_2 , when $i = 0$ we have

$$\begin{aligned} I_2 &= \int_0^{\pi/\kappa} \int_0^{\pi/2} h \cos(2j\phi) \cos \phi d\phi d\eta \\ &= \frac{\pi}{\kappa} \sum_{n=0}^N H_{0,n} \left[\frac{(-1)^{j-n} (1 - 4j^2 - 4n^2)}{16j^4 + (1 - 4n^2)^2 - 8j^2(1 + 4n^2)} \right], \quad j = 0, \dots, N. \end{aligned} \quad (\text{A.5})$$

When $i \geq 1$,

$$\begin{aligned} I_2 &= \int_0^{\pi/\kappa} \int_0^{\pi/2} h \cos(\kappa i \eta) (-1)^j [\cos(2j\phi) + \cos(2(j-1)\phi)] \cos \phi d\phi d\eta \\ &= \frac{\pi}{2\kappa} \sum_{n=1}^N H_{i,n} g(j, n), \quad j = 1, \dots, N \end{aligned} \quad (\text{A.6})$$

where

$$\begin{aligned} g(j, n) &= \frac{96(-1+2j)(-1+2n)}{(-3+2j-2n)(-1+2j-2n)(1+2j-2n)(3+2j-2n)} \times \\ &\quad \times \frac{[4(-1+j)j + (-3+2n)(1+2n)]}{(-5+2j+2n)(-3+2j+2n)(-1+2j+2n)(1+2j+2n)}. \end{aligned}$$

These expressions can be used to directly evaluate their respective integral components in (A.2) so that only I_3 need be evaluated using numerical quadrature. By analytically evaluating the integral components in this manner the computation times were observed to decreaseⁱ because the individual integrand components differ significantly in scale, meaning any adaptive quadrature method has to work very hard to obtain reasonable accuracy when the integrals are not separated using the above analytical technique.

ⁱDecrease is relative to just evaluating the entire integral using numerical quadrature, rather than performing analytical evaluation.

APPENDIX B

COMPRESSIBLE LINEARIZED SYSTEM DERIVATION

The individual equations that comprise the rows of the linear system given by (4.79) are obtained by using orthogonality of the base expansion functions. The general process is identical to that used in section 2.5.2 of chapter 2 and will not be repeated here. Rather, we simply state the results of the integrations and algebraic manipulations. For integer truncation level N , the truncated system of equations corresponding to conservation of mass, given by equation (4.73), is as follows: for $l = 1$ we have

$$\begin{aligned} & \left[-\frac{\kappa(\gamma-1)h_o}{\gamma} - \frac{3\kappa\omega\text{Fr}^2(\gamma-1)}{8\gamma} \left(\frac{1}{\text{Ro}} + \omega \right) \right] P_{\kappa,1} - \frac{\kappa\omega\text{Fr}^2(\gamma-1)}{8\gamma} \left(\frac{1}{\text{Ro}} + \omega \right) P_{\kappa,2} \\ & + \left[\frac{h_o(\gamma-1)}{2\gamma} + \frac{\omega\text{Fr}^2(\gamma-3)}{8\gamma} \left(\frac{1}{\text{Ro}} + \omega \right) \right] Q_{\kappa,1} + \frac{\omega\text{Fr}^2(\gamma-3)}{16\gamma} \left(\frac{1}{\text{Ro}} + \omega \right) Q_{\kappa,2} \\ & + \frac{3\kappa\omega}{2} H_{\kappa,1} - \frac{\kappa\omega}{2} H_{\kappa,2} = c \left[\frac{3\kappa\text{Sr}}{2} H_{\kappa,1} - \frac{\kappa\text{Sr}}{2} H_{\kappa,2} \right], \end{aligned} \quad (\text{B.1})$$

for $l = 2$ we have

$$\begin{aligned} & -\frac{\kappa\omega\text{Fr}^2(\gamma-1)}{8\gamma} \left(\frac{1}{\text{Ro}} + \omega \right) P_{\kappa,1} + \left[-\frac{\kappa h_o(\gamma-1)}{\gamma} - \frac{\kappa\omega\text{Fr}^2(\gamma-1)}{4\gamma} \left(\frac{1}{\text{Ro}} + \omega \right) \right] P_{\kappa,2} \\ & - \frac{\kappa\omega\text{Fr}^2(\gamma-1)}{8\gamma} \left(\frac{1}{\text{Ro}} + \omega \right) P_{\kappa,3} + \left[\frac{3h_o(\gamma-1)}{2\gamma} + \frac{\omega\text{Fr}^2(9\gamma-7)}{16\gamma} \left(\frac{1}{\text{Ro}} + \omega \right) \right] Q_{\kappa,1} \\ & + \left[\frac{3h_o(\gamma-1)}{2\gamma} + \frac{\omega\text{Fr}^2(9\gamma-11)}{16\gamma} \left(\frac{1}{\text{Ro}} + \omega \right) \right] Q_{\kappa,2} + \frac{\omega\text{Fr}^2(3\gamma-5)}{16\gamma} \left(\frac{1}{\text{Ro}} + \omega \right) Q_{\kappa,3} \\ & + \frac{\kappa\omega}{2} H_{\kappa,1} - \kappa\omega H_{\kappa,2} + \frac{\kappa\omega}{2} H_{\kappa,3} = c \left[\frac{\kappa\text{Sr}}{2} H_{\kappa,1} - \kappa\text{Sr} H_{\kappa,2} + \frac{\kappa\text{Sr}}{2} H_{\kappa,3} \right], \end{aligned} \quad (\text{B.2})$$

for $3 \leq l \leq N-1$ we have

$$\begin{aligned}
& -\frac{\kappa\omega\text{Fr}^2(\gamma-1)}{8\gamma} \left(\frac{1}{\text{Ro}} + \omega\right) P_{\kappa,l-1} + \left[-\frac{\kappa h_o(\gamma-1)}{\gamma} \right. \\
& \quad \left. - \frac{\kappa\omega\text{Fr}^2(\gamma-1)}{4\gamma} \left(\frac{1}{\text{Ro}} + \omega\right) \right] P_{\kappa,l} - \frac{\kappa\omega\text{Fr}^2(\gamma-1)}{8\gamma} \left(\frac{1}{\text{Ro}} + \omega\right) P_{\kappa,l+1} \\
& \quad + \frac{\omega\text{Fr}^2[2(l-2)(\gamma-1) + 3\gamma - 1]}{16\gamma} \left(\frac{1}{\text{Ro}} + \omega\right) Q_{\kappa,l-2} \\
& \quad + \left[\frac{(2l-1)h_o(\gamma-1)}{2\gamma} + \frac{\omega\text{Fr}^2[6(l-1)(\gamma-1) + 3\gamma - 1]}{16\gamma} \left(\frac{1}{\text{Ro}} + \omega\right) \right] Q_{\kappa,l-1} \\
& \quad + \left[\frac{(2l-1)h_o(\gamma-1)}{2\gamma} + \frac{\omega\text{Fr}^2[6l(\gamma-1) - 3\gamma + 1]}{16\gamma} \left(\frac{1}{\text{Ro}} + \omega\right) \right] Q_{\kappa,l} \\
& \quad + \frac{\omega\text{Fr}^2[2(l+1)(\gamma-1) - 3\gamma + 1]}{16\gamma} \left(\frac{1}{\text{Ro}} + \omega\right) Q_{\kappa,l+1} \\
& \quad + \frac{\kappa\omega(-1)^l}{2} H_{\kappa,l-1} - \kappa\omega(-1)^l H_{\kappa,l} + \frac{\kappa\omega(-1)^l}{2} H_{\kappa,l+1} \\
& = c \left[\frac{\kappa\text{Sr}(-1)^l}{2} H_{\kappa,l-1} - \kappa\text{Sr}(-1)^l H_{\kappa,l} + \frac{\kappa\text{Sr}(-1)^l}{2} H_{\kappa,l+1} \right] \tag{B.3}
\end{aligned}$$

and for $l = N$ we have

$$\begin{aligned}
& -\frac{\kappa\omega\text{Fr}^2(\gamma-1)}{8\gamma} \left(\frac{1}{\text{Ro}} + \omega\right) P_{\kappa,N-1} + \left[-\frac{\kappa h_o(\gamma-1)}{\gamma} \right. \\
& \quad \left. - \frac{\kappa\omega\text{Fr}^2(\gamma-1)}{4\gamma} \left(\frac{1}{\text{Ro}} + \omega\right) \right] P_{\kappa,N} \\
& \quad + \frac{\omega\text{Fr}^2[2(N-2)(\gamma-1) + 3\gamma - 1]}{16\gamma} \left(\frac{1}{\text{Ro}} + \omega\right) Q_{\kappa,N-2} \\
& \quad + \left[\frac{(2N-1)h_o(\gamma-1)}{2\gamma} + \frac{\omega\text{Fr}^2[6(N-1)(\gamma-1) + 3\gamma - 1]}{16\gamma} \left(\frac{1}{\text{Ro}} + \omega\right) \right] Q_{\kappa,N-1} \\
& \quad + \left[\frac{(2N-1)h_o(\gamma-1)}{2\gamma} + \frac{\omega\text{Fr}^2[6N(\gamma-1) - 3\gamma + 1]}{16\gamma} \left(\frac{1}{\text{Ro}} + \omega\right) \right] Q_{\kappa,N} \\
& \quad + \frac{\kappa\omega(-1)^N}{2} H_{\kappa,N-1} - \kappa\omega(-1)^N H_{\kappa,N} = c \left[\frac{\kappa\text{Sr}(-1)^N}{2} H_{\kappa,N-1} - \kappa\text{Sr}(-1)^N H_{\kappa,N} \right] \tag{B.4}
\end{aligned}$$

For the λ -momentum equation given by (4.74), the individual component equations of the linear system are given by: for $l = 0$,

$$-\frac{\kappa\omega}{2} P_{\kappa,1} - \frac{1}{4} \left(\frac{1}{\text{Ro}} + \omega\right) Q_{\kappa,1} + \frac{\kappa}{\text{Fr}^2} H_{\kappa,1} = c \left[-\frac{\kappa\text{Sr}}{2} P_{\kappa,1} \right], \tag{B.5}$$

for $l = 1$,

$$\begin{aligned}
 -\frac{\kappa\omega}{2}P_{\kappa,1} - \frac{\kappa\omega}{2}P_{\kappa,2} - \frac{1}{4}\left(\frac{1}{\text{Ro}} + \omega\right)Q_{\kappa,2} + \frac{\kappa}{\text{Fr}^2}H_{\kappa,1} - \frac{\kappa}{\text{Fr}^2}H_{\kappa,2} \\
 = c\left[-\frac{\kappa\text{Sr}}{2}P_{\kappa,1} - \frac{\kappa\text{Sr}}{2}P_{\kappa,2}\right] \quad (\text{B.6})
 \end{aligned}$$

and for $l \geq 2$,

$$\begin{aligned}
 -\frac{\kappa\omega}{2}P_{\kappa,l} - \frac{\kappa\omega}{2}P_{\kappa,l+1} + \frac{1}{4}\left(\frac{1}{\text{Ro}} + \omega\right)Q_{\kappa,l-1} - \frac{1}{4}\left(\frac{1}{\text{Ro}} + \omega\right)Q_{\kappa,l+1} \\
 - \frac{\kappa(-1)^l}{\text{Fr}^2}H_{\kappa,l} + \frac{\kappa(-1)^l}{\text{Fr}^2}H_{\kappa,l+1} = c\left[-\frac{\kappa\text{Sr}}{2}P_{\kappa,l} - \frac{\kappa\text{Sr}}{2}P_{\kappa,l+1}\right]. \quad (\text{B.7})
 \end{aligned}$$

Similarly, from the ϕ momentum equation (4.75) we have: for $1 \leq l \leq N-1$,

$$\begin{aligned}
 \frac{1}{2}\left(\frac{1}{\text{Ro}} + \omega\right)P_{\kappa,l} - \frac{1}{2}\left(\frac{1}{\text{Ro}} + \omega\right)P_{\kappa,l+1} + \kappa\omega Q_{\kappa,l} + \frac{2l(-1)^{l+1}}{\text{Fr}^2}H_{\kappa,l} \\
 - \frac{2l(-1)^{l+1}}{\text{Fr}^2}H_{\kappa,l+1} = c[\kappa\text{Sr}Q_{\kappa,l}], \quad (\text{B.8})
 \end{aligned}$$

and for $l = N$ we have

$$\frac{1}{2}\left(\frac{1}{\text{Ro}} + \omega\right)P_{\kappa,N} + \kappa\omega Q_{\kappa,N} + \frac{2N(-1)^{N+1}}{\text{Fr}^2}H_{\kappa,N} = c[\kappa\text{Sr}Q_{\kappa,N}]. \quad (\text{B.9})$$

These relations are then used to construct the generalized eigenvalue problem expressed by (4.79).

APPENDIX C

3D OPENGL ROSSBY WAVE VIEWER

Wave speed = 3.962765e-001
Ap = 6.54 degrees
Aave = 8.97 degrees
Ae = 11.39 degrees
Period = 75.70 days
Current tex_id = 29

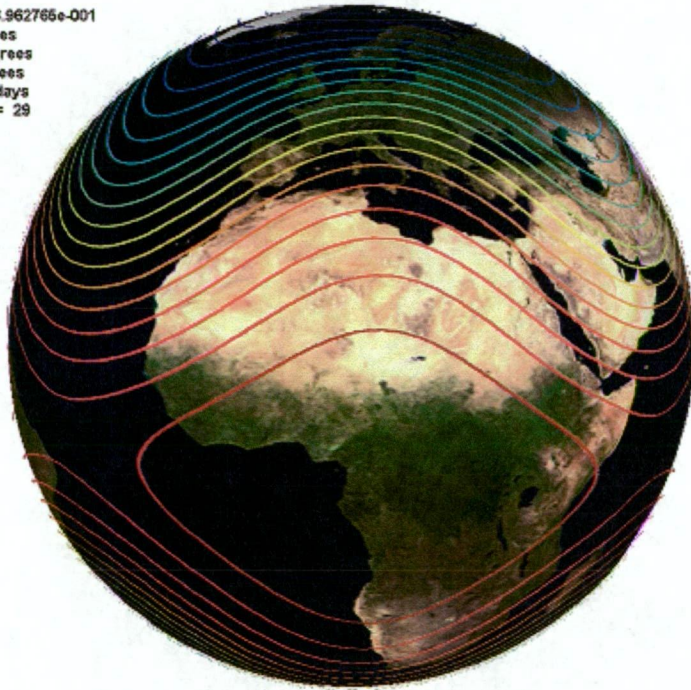


Figure C.1: Rossby-wave viewer output, Equatorial region

A three-dimensional (3D) visualisation tool was developed to aid in interpreting the results, using the OpenGL 3D programming interface. The basic idea and aim was to be able to view progressive-wave free-surface contours superimposed on a rotating sphere in full 3D and real time. Additionally, it was required to translate these contours with respect to the rotating sphere so as to illustrate visually the prop-

agation of the waves. OpenGL provides a convenient interface for accomplishing such a task, with built-in functions to handle the majority of the complex 3D calculations. We present here a brief overview of the processes utilised to implement this program (see, e.g., Hill [33] for an explanation of terms used in this discussion). The basic framework for the 3D program is loosely based around a tutorial on Jeff Molofee's OpenGL related website (see, <http://nehe.gamedev.net>); however substantial changes were required to implement the full program. Additionally, arc-ball camera movement in the program was implemented using Terence J. Grant's tutorial as a guide. This tutorial is also freely available on Jeff Molofee's website (see, <http://nehe.gamedev.net/data/lessons/lesson.asp?lesson=48>).

Wave speed = 3.964142e-001
 Ap = 6.86 degrees
 Aave = 9.56 degrees
 Ae = 12.23 degrees
 Period = 75.68 days
 Current tex_id = 32

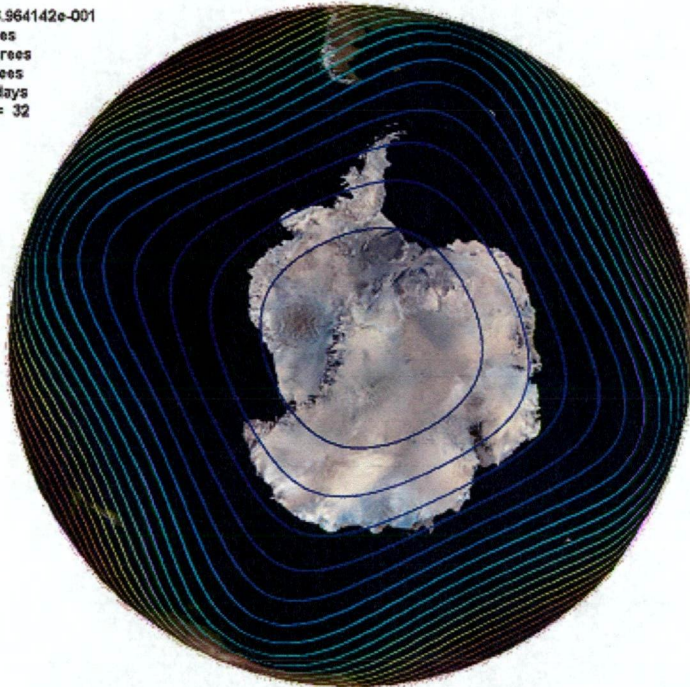


Figure C.2: Rossby-wave viewer output, Antarctic polar region

Full-colour free-surface contours were generated in MATLAB, for every point on each wavespeed-amplitude curve computed. These 2D images were then exported as encapsulated postscript files so they could be scaled without corruption. The images were then clipped and resized so as to be compatible with OpenGL texture loading. Because it was desirable to have a full-colour map of the Earth wrapped around the sphere, it was necessary to make only the contours in each image opaque, with the rest of the image being transparent so that the map of the Earth could

be seen beneath the contours. For this reason, an alpha channel (transparency channel) was added to each image in order to let OpenGL know which parts of each contour image were visible; the alpha channel algorithm was written in MATLAB. The pictures were then saved using the PNG format, which supports the addition of an alpha channel.

Texture mapping (the process of mapping a 2D image onto a 3D surface) was used to load images of the Earth and free-surface contours, and then wrap each image around the surface of a sphere. Various rotations, which are standard functions of the OpenGL language, were then employed to translate the free-surface contours relative to the underlying image of the Earth. This gives the desired effect of the progressive waves moving relative to the fixed land beneath them. Readouts of the current progressive wavespeed, amplitude and period were placed in the upper left-hand corner of the screen, providing easy visual reference.

Wave speed = 4.015673e-001
 A_p = 12.24 degrees
 A_{ave} = 17.19 degrees
 A_e = 22.14 degrees
 Period = 74.71 days
 Current tex_id = 139

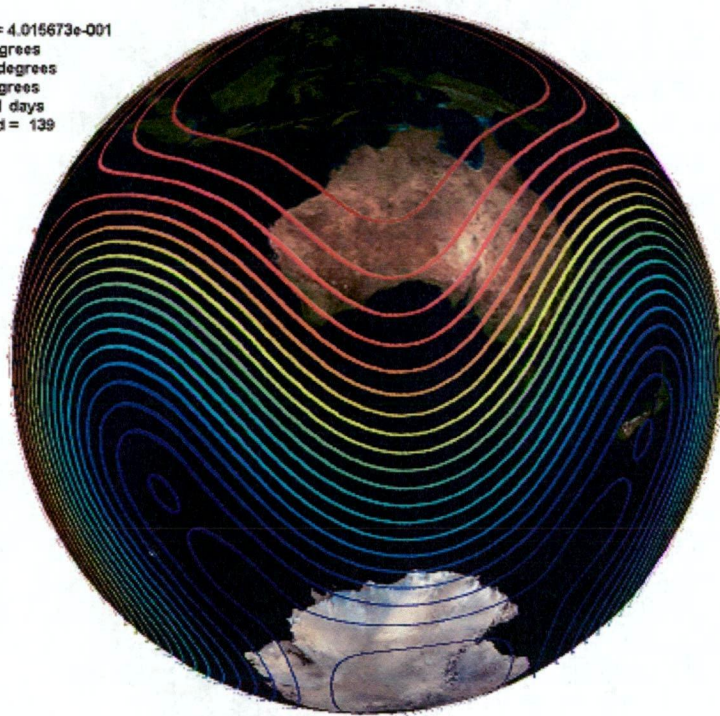


Figure C.3: Rossby-wave viewer output, Australian region

Additionally, a control mechanism was implemented to let a user step easily along the various computed solutions on each wavespeed–amplitude curve. In this manner, the transition and qualitative difference of solutions lying on different resonance branches is readily observed. Complete control over the viewing angle and zoom

level were also implemented, providing visual access to any point on the globe with a simple click and drag or wheel scroll of the mouse.

Figures C.1–C.3, which are screen shots of the running program, illustrate the general output of the viewer, although it must be emphasised that the real program runs in full 3D and is interactive. The viewer has been designed to run on Windows 98/NT/2000/Me/XP operating systems, although a port to Linux would be possible, and requires a system with an OpenGL compliant graphics card with at least 32Mb of memory. The program and source code are freely available upon request to the author.

BIBLIOGRAPHY AND SELECTED READING LIST

- [1] M. Abramowitz and I. A. Stegun. *Handbook of Mathematical Functions with Formulas, Graphs, and Mathematical Tables*. Dover, 1972.
- [2] F. S. Acton. *Numerical Methods that Work*. Harper and Row, 1970.
- [3] W. F. Ames. *Numerical Methods for partial differential equations*. Academic Press, second edition, 1977.
- [4] G. Arfken. *Mathematical Methods for Physicists*. Academic Press, 3rd edition, 1985.
- [5] J. F. Austin. The blocking of middle latitude westerly waves by planetary waves. *Q.J.R. Meteorol. Soc.*, 106:327–350, 1980.
- [6] P. G. Baines. The stability of planetary waves on a sphere. *J. Fluid Mech.*, 73(part 2):193–213, 1976.
- [7] J. J. Barton and L. R. Nackman. *Scientific and Engineering C++: An introduction with advanced techniques and examples*. Addison-Wesley Publishing Company, Inc., 1994.
- [8] G. K. Batchelor. *Introduction to Fluid Dynamics*. Cambridge University Press, 1967.
- [9] J. R. Bates, Y. Li, A. Brandt, S. F. McCormick, and J. Ruge. A global shallow-water numerical model based on the semi-lagrangian advection of potential vorticity. *Q.J.R. Meteorol. Soc.*, 121:1981–2005, 1995.
- [10] John P. Boyd. *Chebyshev and Fourier Spectral Methods*. Dover Publications, 2nd edition, 2000.
- [11] T. G. Callaghan and L. K. Forbes. Nonlinear progressive Rossby waves for incompressible flow on a rotating sphere, Submitted for publication. *J. Fluid Mech.*, 2004.
- [12] C. Canuto. *Spectral Methods in Fluid Dynamics*. Springer Series in Computational Physics. Springer-Verlag, 1988.
- [13] J. G. Charney and J. G. DeVore. Multiple flow equilibria in the atmosphere and blocking. *J. Atmos. Sci.*, 36:1205–1216, 1979.
- [14] J. G. Charney, J. Shukla, and K. C. Mo. Comparison of a barotropic blocking theory with observation. *J. Atmos. Sci.*, 38:762–779, 1981.
- [15] B. Chen and P.G. Saffman. Steady gravity-capillary waves on deep water II. Numerical results for finite amplitude. *Studies in Appl. Math.*, 62:95–111, 1980b.
- [16] H.-B. Cheong. Application of double fourier series to the shallow-water equations on a sphere. *J. Comput. Phys.*, 165:261–287, 2000.

- [17] H.-B. Cheong. Double fourier series on a sphere: Applications to elliptic and vorticity equations. *J. Comput. Phys.*, 157:327–349, 2000.
- [18] E. D. Cokelet. Steep gravity waves in water of arbitrary uniform depth. *Philos. Trans. R. Soc. London Ser. A*, 286:183–230, 1977.
- [19] H. M. Deitel and P. J. Deitel. *C++ How to Program*. Prentice Hall, 1994.
- [20] D. R. Durran. *Numerical Methods for Wave Equations in Geophysical Fluid Dynamics*, volume 32 of *Texts in applied mathematics*. Springer-Verlag, 1998.
- [21] J. A. Dutton. *The Ceaseless Wind: An introduction to the theory of atmospheric motion*. McGraw-Hill, 1976.
- [22] P. N. Edwards. A brief history of atmospheric general circulation modeling. In D. A. Randall, editor, *General Circulation Development, Past Present and Future: The Proceedings of a Symposium in Honor of Akio Arakawa*, pages 67–90. New York: Academic Press, 2000.
- [23] L. K. Forbes and S. R. Belward. Atmospheric interfacial waves in the presence of two moving fluid layers. *Phys. Fluids*, 6(10):3306–3316, October 1994.
- [24] L.K. Forbes. Surface waves of large amplitude beneath an elastic sheet. Part 1. High-order series solution. *J. Fluid Mech.*, 169:409–428, 1986.
- [25] L.K. Forbes. Surface waves of large amplitude beneath an elastic sheet. Part 2. Galerkin solution. *J. Fluid Mech.*, 188:491–508, 1988.
- [26] L. Fox and I. B. Parker. *Chebyshev Polynomials in Numerical Analysis*. Oxford University Press, 1968.
- [27] W. Gander and W. Gautschi. Adaptive quadrature - revisited. *BIT*, 40(1):84–101, March 2000.
- [28] G. H. Golub and C. F. Van Loan. *Matrix Computations*. John Hopkins Series in the Mathematical Sciences. John Hopkins University Press, 1989.
- [29] D. Gottlieb and S. A. Orszag. *Numerical Analysis of Spectral Methods: Theory and applications*. Regional Conference Series in Applied Mathematics. SIAM, 1977.
- [30] G. J. Haltiner. *Numerical Weather Prediction*. John Wiley and Sons, Inc., 1971.
- [31] G. J. Haltiner and R. T. Williams. *Numerical Prediction and Dynamic Meteorology*. Wiley, second edition, 1980.
- [32] B. Haurwitz. The motion of atmospheric disturbances on the spherical earth. *J. Mar. Res.*, 3:254–267, 1940.
- [33] F. S. Hill. *Computer Graphics Using OpenGL*. Prentice Hall, second edition, 2001.
- [34] S. J. Hogan. Some effects of surface tension on steep water waves. *J. Fluid Mech.*, 91:167–180, 1979.
- [35] S. J. Hogan. Some effects of surface tension on steep water waves. Part 2. *J. Fluid Mech.*, 96:417–445, 1980.
- [36] S. J. Hogan. Some effects of surface tension on steep water waves. Part 3. *J. Fluid Mech.*, 110:381–410, 1981.
- [37] James R. Holton. *An Introduction to Dynamic Meteorology*. Academic Press, 1972.
- [38] I. Horton. *Beginning Visual C++ 5*. Wrox Press Ltd., 1997.

- [39] B. J. Hoskins. Stability of the Rossby-Haurwitz wave. *Q.J.R. Meteorol. Soc.*, 99:723–745, 1973.
- [40] R. Jakob-Chien, J. J. Hack, and D. L. Williamson. Spectral transform solutions to the shallow water test set. *J. Comput. Phys.*, 119:164–187, 1995.
- [41] I. N. James. *Introduction to Circulating Atmospheres*. Cambridge Atmospheric and Space Science Series. Cambridge University Press, 1995.
- [42] R. Klein. Asymptotic analyses for atmospheric flows and the construction of asymptotically adaptive numerical methods. *ZAMM*, 80:765–777, 2000.
- [43] H.-O. Kreiss and J. Olinger. Comparison of accurate methods for the integration of hyperbolic equations. *Tellus*, 24:199–215, 1972.
- [44] E. Kreyszig. *Advanced Engineering Mathematics*. Wiley, sixth edition, 1988.
- [45] T. N. Krishnamurti and L. Bounoua. *An Introduction to Numerical Weather Prediction Techniques*. CRC Press, 1996.
- [46] Sir H. Lamb. *Hydrodynamics*. Dover Publications, 6th edition, 1945.
- [47] D. Lanser, J. G. Blom, and J. G. Verwer. Time integration of the shallow water equations in spherical geometry. *J. Comput. Phys.*, 171:373–393, 2001.
- [48] A. T. Layton. Cubic spline collocation method for the shallow water equations on the sphere. *J. Comput. Phys.*, 179:578–592, 2002.
- [49] A. T. Layton and W. F. Spitz. A semi-lagrangian double fourier method for the shallow water equations on the sphere. *J. Comput. Phys.*, 189:180–196, 2003.
- [50] D. K. Lilly. A note on barotropic instability and predictability. *J. Atmos. Sci.*, 30(1):145–146, January 1973.
- [51] R. S. Lindzen. Stationary planetary waves, blocking, and interannual variability. *Adv. Geophys.*, 29:251–273, 1986.
- [52] R. S. Lindzen and M. R. Schoeberl. A note on the limits of rossby wave amplitudes. *J. Atmos. Sci.*, 39(5):1171–1174, May 1982.
- [53] A. Z. Loesch. Finite-amplitude stability or Rossby wave flow. *J. Atmos. Sci.*, 35(6):929–939, June 1978.
- [54] M. S. Longuet-Higgins. Planetary waves on a rotating sphere. *Proc. Roy. Soc. London A*, 279:446–473, 1964.
- [55] M. S. Longuet-Higgins. Planetary waves on a rotating sphere. II. *Proc. Roy. Soc. London A*, 284:40–68, 1965.
- [56] M. S. Longuet-Higgins. New integral relations for gravity waves of finite amplitude. *J. Fluid Mech.*, 149:205–215, 1984.
- [57] M.S. Longuet-Higgins and A.E. Gill. Resonant interactions between planetary waves. *Proc. R. Soc. Lond. A*, 299:120–140, 1967.
- [58] E. Lorenz. Barotropic instability of Rossby wave motion. *J. Atmos. Sci.*, 29(2):258–265, February 1972.
- [59] E. N. Lorenz. *The Nature and Theory of the General Circulation of the Atmosphere*. WMO(Series). World Meteorological Organisation, 1967.
- [60] J. C. McWilliams, L. P. Graves, and M. T. Montgomery. A formal theory for vortex rossby waves and vortex evolution. *Geophys. Astro. Fluid Dyn.*, 97(5):275–309, Aug 2003.

- [61] P. Neittaanmaki, M. Rudnicki, and A. Savini. *Inverse Problems and Optimal Design in Electricity and Magnetism*, volume 35 of *Monographs in Electrical and Electronic Engineering*. Oxford Science Publications, 1996.
- [62] A. Neumaier. Solving ill-conditioned and singular linear systems: A tutorial on regularization. *SIAM Rev.*, 40:636–666, 1998.
- [63] T. Nihei and K. Ishii. A fast solver of the shallow water equations on a sphere using a combined compact difference scheme. *J. Comput. Phys.*, 187:639–659, 2003.
- [64] J. M. Ortega and W. C. Rheinboldt. *Iterative Solution of Nonlinear Equations in Several Variables*. Computer Science and Applied Mathematics. Academic Press, 1970.
- [65] J. Pedlosky. *Geophysical Fluid Dynamics*. Springer-Verlag, 1982.
- [66] N. A. Phillips. Numerical integration of the primitive equations on the hemisphere. *Mon. Wea. Rev.*, 87:333–345, 1959.
- [67] V. Pope and T. Davies. Testing and evaluating atmospheric climate models. *Comp. Sci. Eng.*, 4(5):64–69, Sep-Oct 2002.
- [68] W. H. Press, S. A. Teukolsky, W. T. Vetterling, and B. P. Flannery. *Numerical Recipes in C++: The art of scientific computing*. Cambridge University Press, 2nd edition, 2002.
- [69] C.-G. Rossby and collaborators. Relation between variations in the intensity of the zonal circulation of the atmosphere and the displacements of the semi-permanent centers of action. *J. Mar. Res.*, 2:38–55, 1939.
- [70] R. Salmon. *Lectures on Geophysical Fluid Dynamics*. Oxford University Press, 1998.
- [71] L. W. Schwartz. Computer extension and analytic continuation of stokes' expansion for gravity waves. *J. Fluid Mech.*, 62:553–578, 1974.
- [72] L. W. Schwartz and J.-M. Vanden-Broeck. Numerical solution of the exact equations for capillary-gravity waves. *J. Fluid Mech.*, 95:119–139, 1979.
- [73] L.W. Schwartz and J.D. Fenton. Strongly nonlinear waves. *Ann. Rev. Fluid Mech.*, 14:39–60, 1982.
- [74] J. Shen. Efficient spectral-Galerkin methods III: Polar and cylindrical geometries. *SIAM J. SCI. COMPUT.*, 18(6):1583–1604, November 1997.
- [75] I. Silberman. Planetary waves in the atmosphere. *J. Met.*, 11:27–34, 1954.
- [76] John P. Snyder. *Map projections—A Working Manual*. U.S. Geological Survey professional paper ; 1395, 1987.
- [77] M. A. Snyder. *Chebyshev Methods in Numerical Approximation*. Prentice Hall Series in Automatic Computation. Prentice Hall, 1966.
- [78] G. G. Stokes. On the theory of oscillatory waves. *Camb. Trans.*, viii:441–473, 1847.
- [79] P. N. Swarztrauber. Spectral transform methods for solving the shallow-water equations on the sphere. *Mon. Wea. Rev.*, 124:730–744, 1996.
- [80] M. Taylor, J. Tribbia, and M. Iskandarani. The spectral element method for the shallow water equations on the sphere. *J. Comput. Phys.*, 130:92–108, 1997.
- [81] J. Thuburn and Y. Li. Numerical simulations of rossby-haurwitz waves. *Tellus A*, 52:181–189, 2000.

- [82] M. A. Tolstykh. Vorticity-divergence semi-lagrangian shallow-water model of the sphere based on compact finite differences. *J. Comput. Phys.*, 179:180–200, 2002.
- [83] H. Tomita, M. Tsugawa, M. Satoh, and K. Goto. Shallow water model on a modified icosahedral geodesic grid by using spring dynamics. *J. Comput. Phys.*, 174:579–613, 2001.
- [84] K. Trulsen and C. C. Mei. Modulations of three resonating gravity-capillary waves by a long gravity wave. *J. Fluid Mech.*, 290:345–376, 1995.
- [85] K. Trulsen and C. C. Mei. Effects of weak wind damping on wilton’s ripples. *J. Fluid Mech.*, 335:141–163, 1997.
- [86] A. Wiin-Nielsen and H. Marshall. On the structure of transient atmospheric waves. Part III. *Atmosfera*, 3:73–109, 1990.
- [87] D. L. Williamson, J. B. Drake, J. J. Hack, R. Jakob, and P. N. Swarztrauber. A standard test set for numerical approximations to the shallow water equations in spherical geometry. *J. Comput. Phys.*, 102:211–224, 1992.
- [88] J.R. Wilton. On ripples. *Philos. Mag.*, 29(6):688–700, 1915.

INDEX

- M_b , base system mass, 89
- M_z , zonal flow mass, 90
- T , temperature, 6
- V_b , base volume, 31
- V_z , zonal flow volume, 32, 43, 58
- Ω , angular velocity, 6
- \bar{h} , free-surface height, 8, 74
- β -plane, 1
- κ , longitudinal wavenumber, 18, 43
- ω , zonal angular speed, 16, 85
- u_λ , 5
- u_ϕ , 5
- u_r , 5
- c , angular wavespeed, 13
- h , free-surface depth, 9, 74
- h_o , polar free-surface height, 16, 85
- adiabatic flow, 74
- Amplitude
 - \mathcal{A}_{ave} , 57
 - \mathcal{A}_e , 57
 - \mathcal{A}_p , 57
 - maximum allowable, 68
 - measurement method, 56, 102
 - measurement of, 55
- atmospheric blocking, 113
- barotropic flow, 94
- basis function, 19
 - caching, 44, 51, 101
 - caching example, 51
 - Fourier, 19
 - spherical harmonics, 19
- basis recombination, 21, 86, 99
- bifurcation, 69
- bifurcation point, 64
- bootstrapping, 54, 101
 - type 1, 54
 - type 2, 54
 - type 3, 55
- boundary conditions, 19, 21
- characteristic scales, 14
- collocation, 100
- collocation mesh, 50, 101
 - definition, 51
 - optimal choice, 45
- collocation method, 44
 - advantages, 44
 - algorithm, 45
- computer specifications, 48, 101
- conservation equations
 - dimensional compressible, 81
 - dimensional incompressible, 12
 - incompressible advective form, 13
 - spherical component form, 6
- continuity equation, 6
- convergence, 29
- convergence of longitude, 20
- Coriolis parameter, 15
- curvature terms, 9
- density, 5
 - free-surface value, 84
 - sea-level, 88
- diagonal matrix, 27, 87
- eigenspectrum
 - incompressible, 33
- eigenvalue, 27, 86
 - primary physical, 33, 90
- eigenvalues
 - central band, 33
- eigenvector, 27, 86
- energy conservation, 6, 9
- Euler equation, 6
- finite-difference scheme, 44
- flat-crested wave, 105, 106
- forcing, 49
 - amplitude, 49, 58, 112
 - compressible model, 100
 - thermal, 114
 - topographical, 114

- wavespeed, 49, 61
- Fourier coefficients, 21
- Fourier mode, 18
- Fourier series, 19, 41, 99
 - truncated, 86
 - truncation, 25, 48
- free-surface, 5
- Froude number, 15, 28, 83
- Galerkin method, 21, 44, 86
- generalised eigenvalue problem, 25, 86
 - solution of, 29, 90
 - truncated, 27
- geostrophic approximation, 38, 94
- gravitaitonal acceleration, 5
- height field matching, 36, 93
- horizontal
 - acceleration, 11, 78
 - pressure gradient, 11, 78
- hydrostatic approximation, 10, 77
- ideal fluid, 6
- ideal gas law, 6, 9
- index shifting, 23
- Jacobian matrix, 46, 101
 - calculation of, 52
 - linear dependence, 51
- kinematic condition, 12, 79
- large-scale flow, 28
- latitude, 5
- latitude circle, 51
- linear system
 - infinite, 25
- Linearization
 - compressible, 85
 - incompressible, 17
- localised circulation, 64
- longitude, 5
- Mach number, 83
- mass conservation, 6
- mass specification, 88, 98
- momentum conservation, 6
- Newton–Raphson method, 45, 101
 - algorithm, 46
 - algorithmic flow chart, 47
 - damped, 47
 - shortcomings, 46
- non-dimensionalization
 - incompressible equations, 14
- normal flow, 11
- North pole, 5
- numerical quadrature
 - adaptive recursive, 54
 - Lobatto, 54
- orthogonality, 21, 22
 - algebraic equations, 24
- parameter specification, 28, 57, 87, 103
- parity, 18, 51
- planetary wave, 1
- polar height parametrisation, 44
- polar stereographic projection, 36, 93
- pole problem, 20
- polytropic atmosphere, 76
- pressure, 5
 - cut-off low, 66
 - free-surface value, 84
 - incompressible, 10
 - sea-level, 88
- progressive-wave, 13
- pseudospectral method, 45
- radial coordinate, 5
- recurrence relation, 26
- residual equation, 21, 49
 - redundancy, 51
- residual vector, 101
- resonance
 - branch, 61
 - damped, 69, 107, 109
 - discrete branching, 62
 - nonlinear, 61, 104, 106, 112
 - parameter region, 63
 - planetary wave, 63
- reverse flow, 64
- root finding, 90
 - multi-dimensional, 45
- Rossby number, 15, 28, 83
- Rossby wave, 1, 15
 - observational method, 113
 - stationary, 34, 113
- Rossby–Haurwitz
 - comparison with compressible
 - linearized solution, 92
 - comparison with incompressible
 - linearized solution, 35
 - formula, 35, 92
 - free-surface contours, 37

- scale analysis, 10
- series representation, 41
- shallow atmosphere
 - compressible, 74
 - incompressible, 8
- shallow atmosphere approximation, 10, 76
- shallow atmosphere equations
 - non-dimensional compressible, 83, 97
 - non-dimensional compressible
 - linearized, 85
 - non-dimensional incompressible, 15, 40
 - non-dimensional incompressible
 - linearized, 17, 18
- singular value decomposition, 42
- South pole, 5
- spherical polar coordinate system, 5
- stability
 - planetary wave, 63
- stagnation point, 20, 63, 65, 107
 - symmetrical location, 65
- Strouhal number, 15, 28, 83
- super rotation, 16
- symmetry conditions, 19, 43, 86, 99

- unit vector, 5

- valid zonal flow value, 31, 32
- velocity vector, 5
- volume conservation, 31
- volume matching condition, 32
- volume specification, 43

- zonal flow, 15, 84